Doctorate Dissertation

博士論文

Magnetic and electronic states of spinel ferrites studied by x-ray magnetic circular dichroism

（X 線磁気円二色性によるスピネルフェライトの磁性と電子状態の研究）

A Dissertation Submitted for Degree of Doctor of Science
December 2018

平成 30 年 12 月博士（理学）申請

Department of Physics, Graduate School of Science,
The University of Tokyo

東京大学大学院理学系研究科物理学専攻

Yosuke Nonaka

野中　洋亮

Magnetic and electronic states of spinel ferrites studied by x-ray magnetic circular dichroism

Thesis

Yosuke Nonaka

Department of Physics,
Graduate School of Science,
The University of Tokyo

December, 2018

Abstract

Transition-metal oxides are one of the most representative class of materials of strongly correlated electron systems. They show novel phenomena originating from the interplay between charge, spin, lattice, and orbital degrees of freedom. Among them, spinel ferrites $M\mathrm{Fe_2O_4}$ have attracting strong attention from both the scientific and technological point of view. In this thesis, we presented new insights into the electronic and magnetic states in spinel ferrites.

From the viewpoint of technological applications, the spin-filter structure using spinel ferrites are intensively studied as a promising spin injector to Si. However, the degradation of ferrimagnetic order at the interface between the spinel ferrites and other materials have prevented practical applications. In order to clarify the microscopic origin of the degradation of ferrimagnetic order, we have investigated magnetic and electronic states of epitaxial $\mathrm{CoFe_2O_4}(111)$ and $\mathrm{NiFe_2O_4}(111)$ thin films using x-ray absorption spectroscopy (XAS) and x-ray magnetic circular dichroism (XMCD).

In Chapter 3, we investigated the magnetocrystalline anisotropy (MCA) of $\mathrm{CoFe_2O_4}$ thin films. From the magnetic-field-angle dependence of XMCD spectra, it was found that the MCA of $\mathrm{CoFe_2O_4}$ is significantly reduced near the interface. This behavior was qualitatively explained by the change of cation distribution near the interface. We also pointed out that the small epitaxial strain induce a uniaxial MCA.

In Chapter 4, the as-grown and annealed $\mathrm{CoFe_2O_4}(111)$ and $\mathrm{NiFe_2O_4}(111)$ thin films were studied by XAS and XMCD. By analyzing the spectral line shapes, the valences and site occupancies of Fe ions were obtained. We observed that the Fe ions are redistributed by annealing, and the degraded ferrimagnetic order near the interface is successfully recovered. It was found that the microscopic origin

of the degradation of ferrimagnetic order is vacant T_d sites which exist near the interface.

From a fundamental scientific viewpoint, the Verwey transition of Fe_3O_4 has also been studied. Accurate XMCD experiments have been performed using a newly developed 'vector-magnet' apparatus and a fast polarization-switching undulator beamline. We found that the orbital magnetic moment decreases upon cooling across the Verwey transition temperature T_V. We also found that there was almost no anisotropy of the orbital magnetic moment above and below T_V within experimental error below 0.01 μ_B/atom. The observed temperature dependence and the upper bound for the angle dependence of the orbital magnetic moments would put constraints on theoretical models for the studies of the Verwey transition.

Contents

Chapter 1

Introduction

1.1 Spinel-type oxides

Materials with strong electron-electron interaction, which are called strongly correlated electron systems, have been a hot topic for a long time. Transition-metal oxides are one of the representative materials of the strongly correlated electron systems. Unlike conventional metals, the charge degree of freedom is significantly restricted and, therefore, the rest of the degree of freedom (spin and orbital) can play important roles and many macroscopic novel phenomena appear, such as giant magnetoresistance [1], metal-insulator transition [2], multiferroics [3], high-T_C superconductivity [4], and so on. Therefore, many kinds of transition-metal oxides have been studied intensively for both the scientific and technological interests.

A typical example is a perovskite-type transition-metal oxide ABO_3. Figure 1.1 (a) shows the unit cell of a cubic perovskite structure, where a transition-metal ion B is located at the center of six oxygen ligands. The A site is usually occupied by the rare-earth ions and they supply electrons to $3d$-$2p$ hybridized bands. By substituting various ions for the A and B site, one can easily control the physical properties and the electronic states via filling control and bandwidth control [2]. Therefore, numerous studies have been performed on this system. For example in the perovskite-type manganites $LaMnO_3$, the importance of the orbital degree of freedom, namely, which orbitals are occupied among the nearly-degenerate $3d$ orbitals, has been pointed out [7]. Such a degree of freedom in partially filled e_g

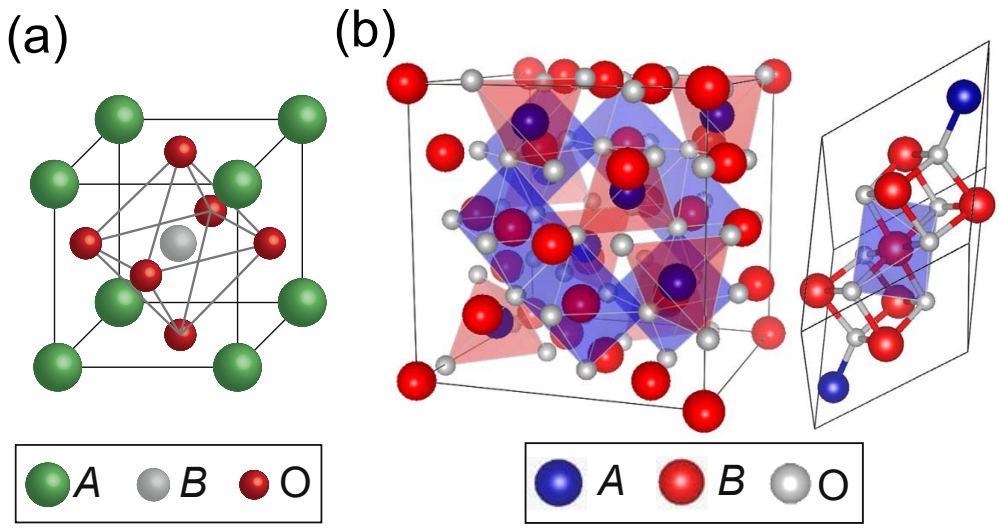

Figure 1.1: Crystal structures of perovskite-type and spinel-type oxides. (a) Unit cell of the cubic perovskite structure. Adapted from Ref. [5]. (b) Cubic unit cell (left) and primitive unit cell (right) of the spinel-type structure. Illustrated using the VESTA software [6].

orbitals (e_g^1) gives rise to the orbital-ordered state in which the occupied orbitals form a regular pattern over the crystal [8].

The spinel-type oxide AB_2O_4 have also attracted much attention because of the interesting and valuable properties. This class of compounds contains one or two kinds of transition-metal ions in the A and B sites in their crystal structures. Therefore, a wide variety of novel phenomena can be realized by selecting the appropriate pairs of the transition-metal ions for the two sites. Figure 1.1 (b) shows the crystal structure of the spinel-type oxides. There are two views of unit cells. The conventional cubic unit cell (left) and a primitive unit cell (right) are shown. Hereafter, we use the cubic unit cell for crystallographic notations. The A ion is surrounded by four oxygen atoms in the tetrahedral coordination and, therefore, has T_d symmetry. On the other hand, the B ion is surrounded by six oxygen atoms in the octahedral coordination and, therefore, has the O_h symmetry. Hereafter, we label the two sites as T_d and O_h sites. Unlike the fivefold degeneracy in a free atom, the d orbitals of ions in solids are split into several levels reflecting

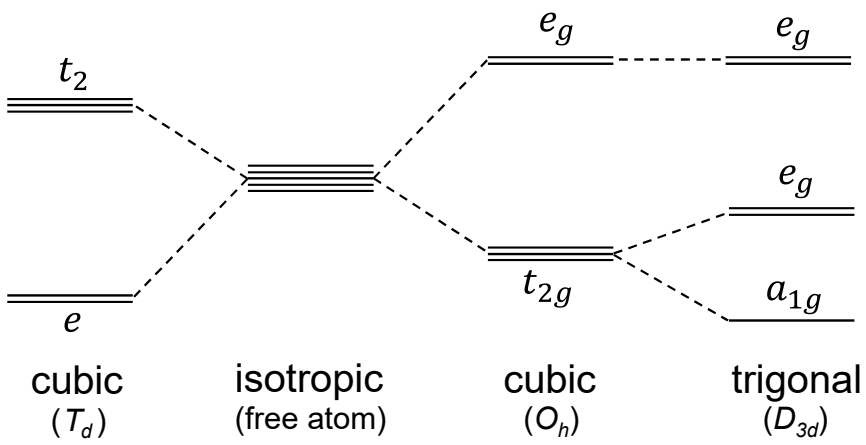

Figure 1.2: Energy-level diagram for the crystal-field splitting of 3d-orbitals under the cubic (T_d), isotropic, cubic (O_h), and trigonal (D_{3d}) symmetry.

the symmetry of surrounding environment. Considering the surrounding oxygen ions as negative point charges, one can simply treat the effects of ligands on the orbital energy levels as electrostatic fields, known as the crystal field. Figure 1.2 shows the energy-level diagram for the crystal-field splittings. The energy levels of the 3d orbitals split into the doubly degenerate e_g (e) and the triply degenerate t_{2g} (t_2) orbitals at the O_h (T_d) site. Strictly speaking, the 'O_h' site does not have full octahedral (O_h) symmetry but trigonal (D_{3d}) symmetry. Therefore, the t_{2g} orbitals further split into the doubly degenerate e_g and the nondegenerate a_{1g} orbitals. As shown in the primitive unit cell in Fig. 1.1 (b), the second nearest neighbors (six B ions) are located only around one of the four trigonal axes of the BO$_6$ octahedron. Therefore, the BO$_6$ octahedron is elongated along the trigonal axis (the $\langle 111 \rangle$ direction in a cubic notation), resulting in symmetry lowering of the crystal field. In addition, the neighboring B ions also induce a trigonal field at the center of the BO$_6$ octahedron. The elongation of the BO$_6$ octahedra favors the e_g ground state, while the trigonal field generated by the neighboring B ions favors the a_{1g} ground state [9]. Therefore, it is difficult to determine which of these two orbitals has lower energy and how large the energy gap is. This trigonal splitting is often neglected [10].

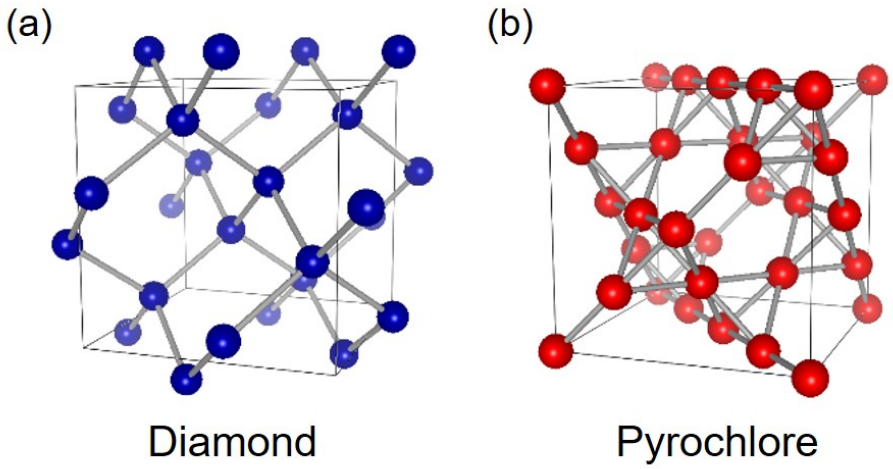

Figure 1.3: Sublattices of the spinel-type structure. (a) Diamond sublattice consisting of T_d sites. (b) Pyrochlore sublattice consisting of O_h sites.

The valence of transition metal ions in the T_d and O_h sites depends on the situation. Therefore, spinel-type oxides can be classified into two groups. One is the normal spinel, in which ions at the T_d and O_h sites are divalent and trivalent, respectively. The other is the inverse spinel, where ions at the T_d sites are trivalent (B^{3+}), and the O_h sites are occupied by divalent and trivalent ions (A^{2+} and B^{3+}) with the $1:1$ ratio. In actual compounds, exchange of the ions between the T_d and O_h sites often occurs [11], namely, the two ions A and B are distributed into both the two sites. This cation distribution is an important parameter to determine the physical properties of spinel oxides. The cation distribution is usually evaluated by the inversion parameter y, which is defined as

$$[A_{1-y}B_y]_{T_d}[A_yB_{2-y}]_{O_h}\mathrm{O}_4. \tag{1.1}$$

Here, $y = 1$ ($y = 0$) represents a perfect inverse (normal) spinel structure.

The spinel structure also provides a strong geometrical frustration for ions at the octahedral site. As shown in Fig. 1.3, the octahedral sites form a pyrochlore lattice, and the frustration caused by this structure is thought to be the origin of the $3d$ heavy electron of the LiV_2O_4 [12]. Also, the tetrahedral sites form a diamond lattice, and provide a geometrical frustration which causes a spin-liquid state in

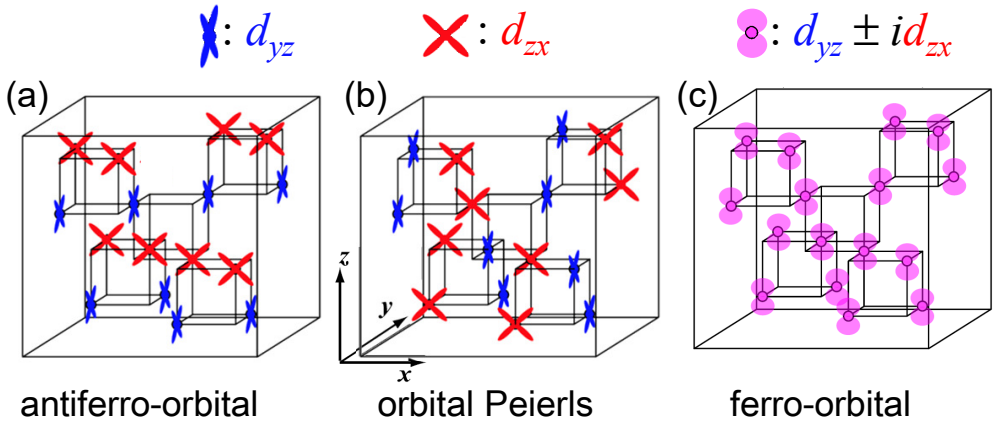

Figure 1.4: Schematic pictures of orbital order proposed by theoretical models [17]. The d_{xy} orbitals are omitted because they are occupied in any models.

$CoAl_2O_4$ [13]. These features of the spinel-type oxides cause a variety of novel phenomena, e.g., the spin-orbital liquid state of $MnSc_2S_4$ [14], the orbital glass state of $FeCr_2S_4$ [15], the multiferroic behavior of $CoCr_2O_4$ [16], and so on.

Orbital order in spinel-type oxides

Similarly to the perovskite manganites, one can realize the system with an orbital degree of freedom in the spinel-type oxides. The orbital-order phenomena in the spinel-type vanadates AV_2O_4 (A = Mn, Fe, Co, Zn...) are well studied, where V^{3+} at the O_h site (t_{2g}^2) is the orbital-active ion. Figure 1.4 shows possible orbital orders predicted by theories [18–20]. In the recent reports, the antiferro-orbital orders were found in MnV_2O_4 and CoV_2O_4 [17, 21]. Ti^{3+} ($3d^1$), Ir^{4+} ($5d^5$), and Fe^{2+} ($3d_{HS}^6$) are also known as orbital active ions in the O_h site [10]. Particularly, the orbital degree of freedom in the Fe^{2+} (O_h) ion play an important role in the Verwey transition (to be introduced in section 1.5).

Ferrimagnetism in spinel ferrites

The interests from both the scientific and technological aspects are important factors of the spinel-type oxides. One of the most prominent examples is the spinel

Table 1.1: Magnetization of spinel ferrites $M\mathrm{Fe_2O_4}$ (M = Mn, Fe, Co, Ni, Cu) in units of μ_B/formula unit. Adapted from Ref. [24].

M^{2+}	Mn^{2+} (d^5)	Fe^{2+} (d^6)	Co^{2+} (d^7)	Ni^{2+} (d^8)	Cu^{2+} (d^9)
m_spin of M^{2+}	5	4	3	2	1
Experiment	5.0	4.2	3.3	2.3	1.3

ferrites. The Fe-Co ferrite ($\mathrm{Fe_3O_4} \cdot 3\mathrm{CoFe_2O_4}$) found in 1932 was industrialized as an oxide magnet [22]. In 1948, Néel has successfully explained the origin of strong magnetism in spinel ferrites $M\mathrm{Fe_2O_4}$ (M = Mn, Fe, Co, Ni, Cu) [23], where the strong antiferromagnetic interaction between the transition-metal ions at the T_d and O_h sites stabilizes the ferrimagnetic order. Since the spinel ferrites tend to take the inverse spinel structure, the M^{2+} ions enter the O_h site. Thus, the spin magnetic moments of the Fe^{3+} ions at the T_d and O_h sites, which are antiferromagnetically coupled, cancel out each other. Therefore, the magnetization of $M\mathrm{Fe_2O_4}$ arises from the remaining magnetic moment of the M^{2+} ion at the O_h site. Note that the $\mathrm{MnFe_2O_4}$ indeed takes normal spinel structure and, therefore, the Mn^{2+} (d^5) ion and Fe^{3+} (d^5) ion enter the T_d and O_h site, respectively. However, the expected spin magnetic moment at the O_h site is unchanged. Table 1.1 shows the magnetization of spinel ferrites in units of μ_B/formula unit, compared with the expected value of spin magnetic moments of M^{2+} ions [24]. One can see a consistent tendency between the experimental values of magnetization and the spin magnetic moments of the M^{2+} ions.

1.2 Spin-filter structure using spinel ferrites

Controlling the charge degree of freedom of electrons in semiconductors, electronics have achieved great success. Adding the spin degree of freedom to existing electronics, a new field of electronics is developing, which is known as spintronics (spin electronics). To integrate the spin degree of freedom into existing semiconductor technologies, room-temperature spin-polarized carriers should be realized in a semiconductor. To realize that, particularly in existing Si-based technology,

the electrical injection of spin-polarized current into a semiconductor is necessary. A spin filter is a promising technology to inject the highly spin-polarized current into a semiconductor. Spinel ferrite thin films are attracting high attention as a promising material for the spin-filter device structures. In this section, the principles and related phenomena of the spin filter will be described.

1.2.1 Spin filter

The spin filter uses a spin-polarized tunneling. Figures 1.5 (a) and (b) schematically show the spin-filter effect in a metal-EuO-metal tunnel junction [25]. EuO is a ferromagnetic semiconductor below the Curie temperature T_C of 69 K [26], where, the Eu 5d band split into spin-up and spin-down bands (Fig. 1.5 (a)). This splitting $2\Delta E_{EX}$ is known as exchange splitting. Figure 1.5 (b) shows the schematic energy band diagram of the metal-EuO-metal tunnel junction. Since the exchange splitting of the EuO layer provides different barrier height for spin-up and spin-down electrons, the tunneling probability strongly depends on the spin state of electrons. Therefore, in this configuration, spin-up current can largely exceed the down-spin current, namely, the spin-polarized current is injected into the right-hand side metal. Figure 1.5 (c) demonstrates the spin-filter property. At low temperature, the injected spin-polarized current makes the right-hand side metal spin-polarized, resulting in the large decrease in the tunnel-junction resistance. The polarization of the tunneling current is also estimated and found that nearly perfect polarization is achieved. Here, the polarization P of tunneling current is defined as

$$P = \frac{J_\uparrow - J_\downarrow}{J_\uparrow + J_\downarrow}, \tag{1.2}$$

where, $J_\uparrow$ and $J_\downarrow$ is the spin-up and spin-down tunneling current, respectively.

1.2.2 Spinel ferrites as a spin-filtering materials

Although the ability of spin filter structure was proven, the T_C's of Eu-chalcogenides are much lower than 300 K (69 K for EuO, 16.6 K for EuS, and 4.6 K for EuSe) [27]. In order to realize the room-temperature spin filter, new materials which have high Curie temperature are desired. Figure 1.6 (a) shows spin-dependent densities of states (DOS) for $CoFe_2O_4$ [28]. One can see that the

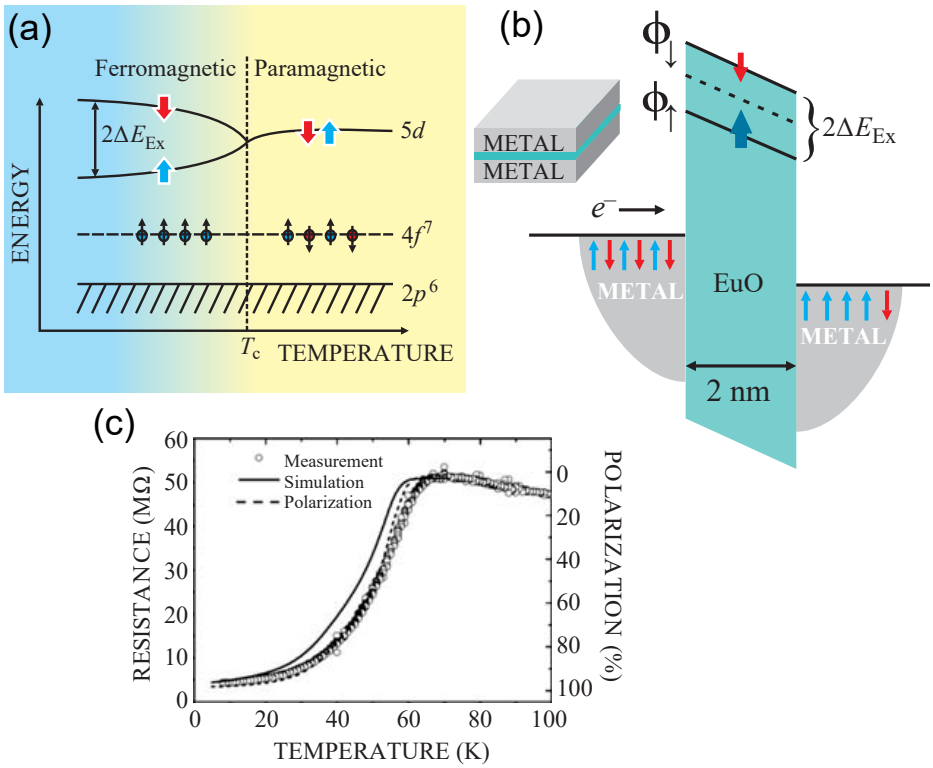

Figure 1.5: Principle of spin-filter effect using EuO thin film. Adapted from Ref. [25]. (a) Exchange splitting in EuO. Below the Curie temperature T_C, the 5-*d* conduction band split into spin-up and spin-down levels separated by an energy $2\Delta E_{EX}$. (b) Schematic diagram of a metal-EuO-metal spin filter. The exchange splitting $2\Delta E_{EX}$ leads different barrier height for spin-up and spin-down electrons. (c) Resistance of the junction and the spin polarization of tunneling current in the device as a function of temperature.

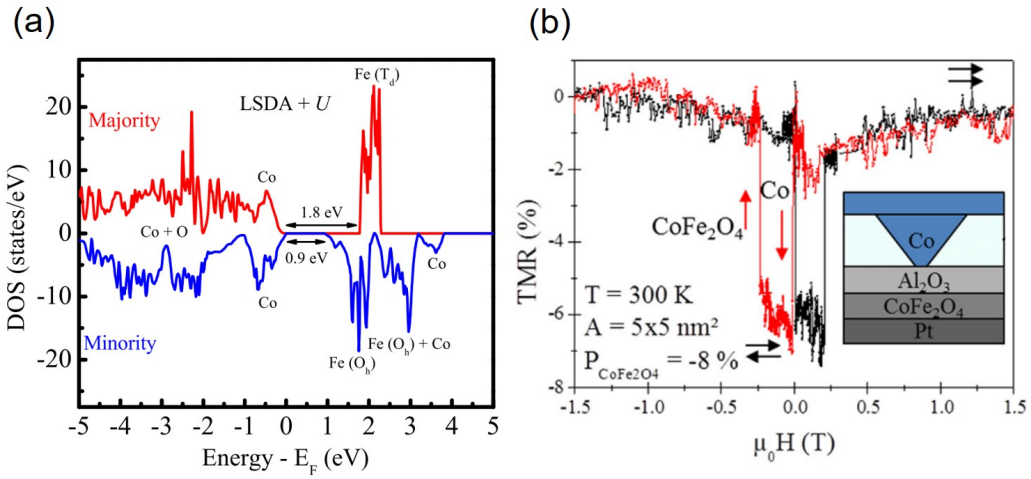

Figure 1.6: (a) Spin-dependent density of states of $CoFe_2O_4$ calculated using density-functional theory. Reproduced from Ref. [28]. (b) Tunnel-magnetoresistance curve of the Pt(20 nm)/$CoFe_2O_4$(3 nm)/γ-Al_2O_3(1.5 nm)/Co(10 15 nm) tunnel junction measured at 300 K. Adapted from Ref. [29].

band gaps are enough different for spin-up and spin-down electrons and, therefore, these band gaps can be used as different barrier heights for spin-up and spin-down electrons. Considering the high Neel temperature of 793 K [24], $CoFe_2O_4$ is a very promising material for the room-temperature spin filter. Therefore, spin-filter structures using $CoFe_2O_4$ (and also other spinel ferrites) are intensively studied [30, 31]. The ability of spinel-ferrite based spin filter structure at room temperature has been examined. Figure 1.6 (b) shows the tunnel magnetoresistance (TMR) curve of a Pt(20 nm)/$CoFe_2O_4$(3 nm)/γ-Al_2O_3(1.5 nm)/Co(10-15 nm) tunnel junction measured at 300 K [29]. One can see a clear hysteretic behavior reflecting spin-polarized tunneling. Although the room-temperature spin filter was achieved, the polarization of tunneling current is low ($P = -8\%$). Note that the band gap for spin-down electrons is smaller than that for spin-up electrons, resulting in the minus sign of P. One recognized origin for this low polarization is the midgap impurity states induced by structural and/or chemical defects [31–33]. For example, the presence of Co^{3+} would reduce the band gaps which are working as the spin-dependent barrier height in the spin-filter structure [33]. Another

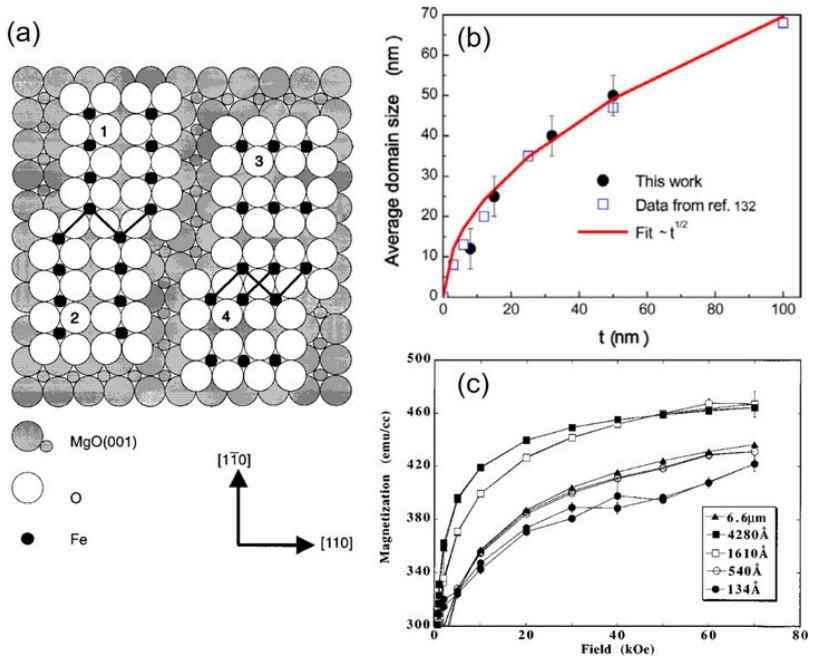

Figure 1.7: (a) Schematic illustration of the formation of a Fe_3O_4 film on MgO(001) substrates. The islands with different 'phases' (1, 2, 3, and 4) and their coalescence are shown. For clarity, the Fe ion at the T_d site is omitted. Solid lines denote the antiferromagnetic 180° Fe-O-Fe superexchange paths. Reproduced from Ref. [36]. (b) Thickness dependence of the average APBs' domain size. Reproduced from Ref. [30]. (c) In-plane M-H curves for Fe_3O_4 films with various thicknesses grown on MgO(001) substrates. Reproduced from [34]. Note that the 6.6 μm-thick film was grown under different oxygen pressure from the others.

recognized origin is the magnetically dead layer induced by antiphase boundaries (APBs), which is well known in the epitaxial Fe_3O_4 thin films [34–38]. Figure 1.7 (a) shows a schematic illustration of the formation of APBs in a Fe_3O_4 thin film which is epitaxially grown on MgO substrates. The independently grown islands 1, 2, 3, and 4 are shifted or rotated with respect to each other. Therefore, coalescence of them results in the boundaries where the crystal structure is imperfect, namely, the APBs. One can see that many antiferromagnetic 180° Fe-O-Fe

superexchange paths exist at the APBs, which results in antiferromagnetic interdomain couplings [35]. Therefore, APBs significantly reduce the ferrimagnetic order of spinel ferrites. Figure 1.7 (b) shows the thickness dependence of the average APBs domain size. The domain size becomes smaller in thinner region, namely, many antiferromagnetic interdomain couplings exist particularly near the interface region of spinel ferrite. Therefore, there is a region where the ferrimagnetic order of spinel ferrite is significantly reduced near the interface, which is known as a magnetically dead layer. Figure 1.7 (c) shows the M-H curves of the Fe_3O_4 thin films with various thicknesses. The magnetization decreases with decreasing thickness. The magnetically dead layer obviously reduce the polarization of the tunneling current.

1.3 MFe$_2$O$_4$(111)/Al$_2$O$_3$(111)/Si(111) structure

Although the above spin-filter structures are metal-insulator-metal configurations, in order to inject spin-polarized current into semiconductors, metal-insulator-semiconductor structures are necessary. Recently, an epitaxial $CoFe_2O_4(111)$ thin film was grown on a Si(111) substrate using a γ-$Al_2O_3(111)$ buffer layer [39]. This $CoFe_2O_4(111)/Al_2O_3(111)/Si(111)$ structure is promising for the room-temperature high-efficiency spin-polarized current injection into Si. Wakabayashi *et al.* have fabricated the $CoFe_2O_4(111)/Al_2O_3(111)/Si(111)$ and the $NiFe_2O_4(111)/Al_2O_3(111)/Si(111)$ structures with the spinel ferrite layer of various thicknesses [40,41]. They also investigated the electronic and magnetic property of these films using x-ray absorption spectroscopy (XAS) and x-ray magnetic circular dichroism (XMCD). In this section, the electronic and magnetic states of these spin-filter structures will be described.

1.3.1 CoFe$_2$O$_4$(111)/Al$_2$O$_3$(111)/Si(111)

Figure 1.8 (a) shows the structure of $CoFe_2O_4(111)/Al_2O_3(111)/Si(111)$. The $CoFe_2O_4$ layers with various thicknesses (d = 1.4, 2.3, 4, and 11 nm) were grown on Si(111) substrates using 2.4 nm-thick γ-Al_2O_3 buffer layers. Figure 1.8 (b) shows the cross-sectional transmission electron microscopy (TEM) image of the 11 nm-thick $CoFe_2O_4$ film. One can confirm that the $CoFe_2O_4$ layer is an epitax-

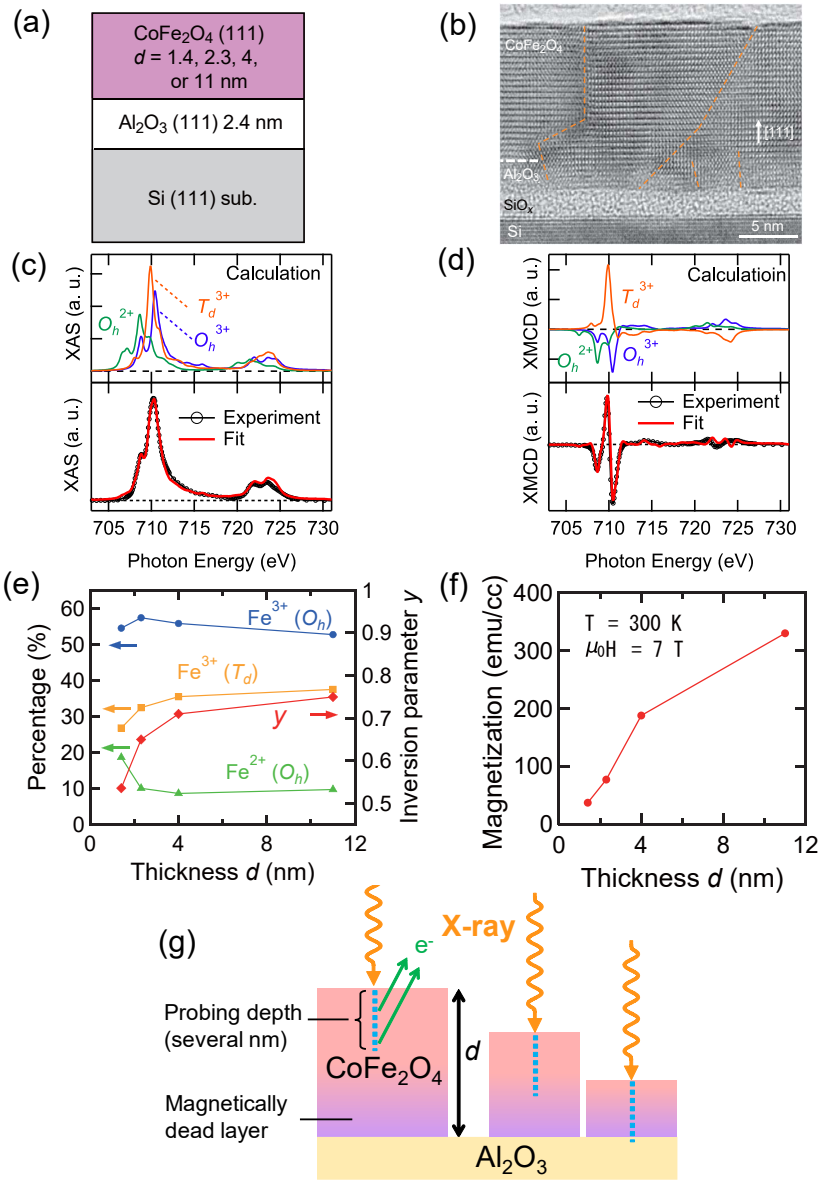

Figure 1.8: (a) Sample structure of $CoFe_2O_4(111)/Al_2O_3(111)/Si(111)$ thin films. (b) Cross-sectional TEM image of the 11 nm-thick $CoFe_2O_4$ film. Orange dashed lines denote the APBs. (c), (d) XAS and XMCD spectra of the 11 nm-thick $CoFe_2O_4$ film, compared with calculated spectra based on cluster model. (e) Cation distribution and inversion parameter y as functions of thickness. (f) Thickness dependence of magnetization derived from the fitting of spectra. (g) Schematic illustration of the probing depth of the XMCD measurements and the magnetically dead layer near the interface. Panels (a), (b), (e), and (f) were adapted from Ref. [40].

ially grown single-crystalline film. The orange dashed lines represent the APBs. Contrary to the case of Fe_3O_4 shown in Fig. 1.7 (b), the density of APBs in the $CoFe_2O_4$ layer does not show significant thickness dependence. The two APBs penetrate the whole $CoFe_2O_4$ layer, and the other APBs vanish in the Al_2O_3 buffer layer. The electronic states and magnetic property of these films were investigated using XAS and XMCD. Figures 1.8 (c) and (d) show the XAS and XMCD spectra of the 11 nm-thick $CoFe_2O_4$ film for example. The upper panels of Figs. 1.8 (c) and (d) show the calculated spectra for the $Fe^{3+}(O_h)$, $Fe^{3+}(T_d)$, and $Fe^{2+}(O_h)$ ions based on the cluster model (see Chapter. 2). By fitting the weighted sum of the these spectra to the experimental spectra as shown in lower panels of Figs. 1.8 (c) and (d), one can decompose XAS and XMCD spectra into three contributions from the $Fe^{3+}(O_h)$, $Fe^{3+}(T_d)$, and $Fe^{2+}(O_h)$ ions. Figure 1.8 (e) shows the ratio of the numbers of the $Fe^{3+}(O_h)$, $Fe^{3+}(T_d)$, and $Fe^{2+}(O_h)$ ions as functions of thickness.The inversion parameter y, which is estimated from the distribution of three Fe ions [see Eq. (1.1)], is also plotted. One can see a sudden decrease of y in thinner region ($d < 4$ nm). Figure 1.8 (f) shows the thickness dependence of magnetization deduced from the fittings (the weighted sum of the calculated magnetic moments for every Fe and Co ion). The magnetization significantly decreases with decreasing thickness particularly in thinner region ($d < 4$ nm). As illustrated in Fig. 1.8 (g), the authors employed surface-sensitive detection mode (probing depth $\sim$ several nm, see section 2.1.4). Therefore, the sudden decrease of y and magnetization in thinner region ($d < 4$ nm) reflects the magnetically dead layers near the interface. Note that the density of the APBs is not clearly changed as shown in Fig. 1.8 (b). To summarize, the magnetically dead layer of $CoFe_2O_4$ thin film was found near the interface, which originates not only from the APBs but also from the cation distribution.

1.3.2 $NiFe_2O_4(111)/Al_2O_3(111)/Si(111)$

Figure 1.9 (a) shows the structure of $NiFe_2O_4(111)/Al_2O_3(111)/Si(111)$. The $NiFe_2O_4$ layers with various thicknesses (d = 1.7, 3.5, and 5.2 nm) were grown on Si(111) substrates using 1.4 nm-thick γ-Al_2O_3 buffer layers. Figure 1.8 (b) shows the cross-sectional TEM image of the 5.2 nm-thick $NiFe_2O_4$ film. Similarly to the $CoFe_2O_4$ case, one can see APBs marked by orange dashed lines and the number

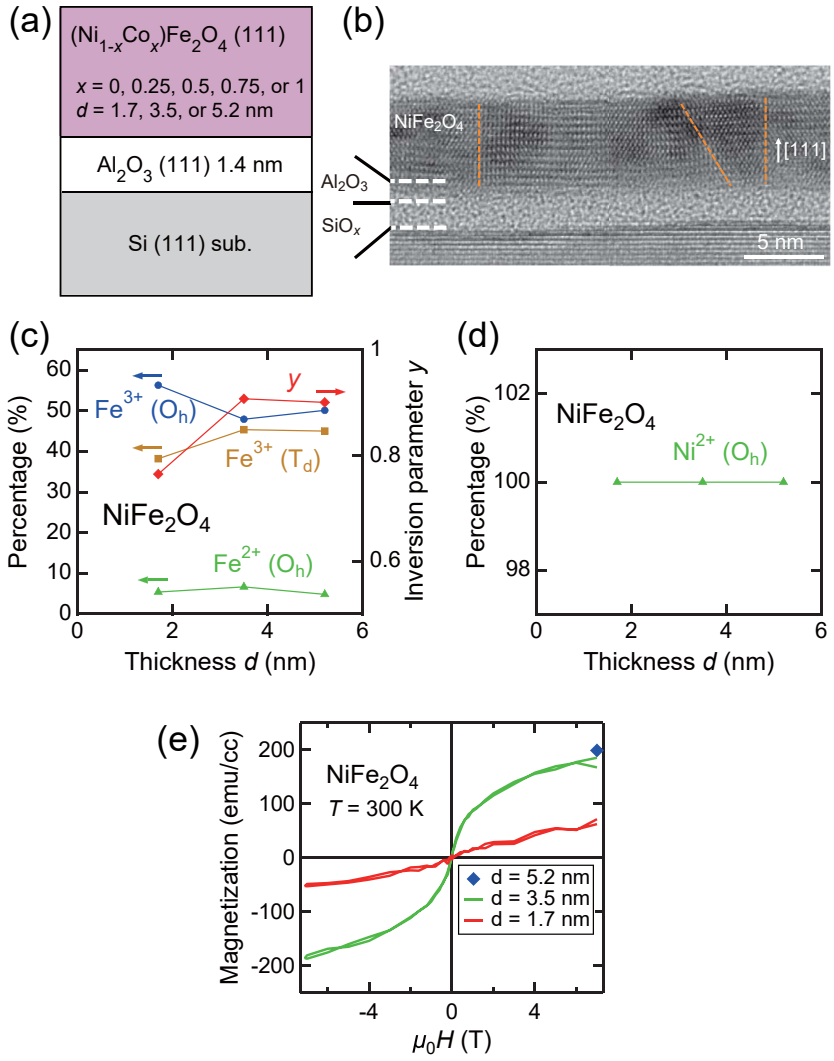

Figure 1.9: (a) Sample structure of $NiFe_2O_4(111)/Al_2O_3(111)/Si(111)$ thin films. (b) Cross-sectional TEM image of the 5.2 nm-thick $NiFe_2O_4$ film. Orange dashed lines denote the APBs. (c) Fe ion distribution and inversion parameter y as a function of thickness. (d) Ni ion distribution as functions of thickness. (e) M-H curve of the $NiFe_2O_4$ films with various thicknesses. All panels were adapted from Ref. [41].

of APBs does not depend on thickness. Figures 1.8 (c) and (d) shows the distribution of the Fe and Ni ions as functions of thickness deduced by the fitting. The inversion parameter y is also plotted in Fig. 1.8 (c). The inversion parameter y (0.79–0.91) is much larger than that of $CoFe_2O_4$ films (0.54–0.75), and the Ni ion takes only the divalent state at the O_h site. This behavior was attributed to the high site selectivity of Ni ions. Figure 1.8 (e) shows the M-H curves of the $NiFe_2O_4$ films with various thicknesses deduced from the magnetic-field dependence of XMCD intensities. One can see that the magnetization of $NiFe_2O_4$ thin films is unchanged between the 5.2 and 3.5 nm-thick films, whereas that of the $CoFe_2O_4$ films show a rapid decrease in the same thickness range (see also Fig. 1.8 (f)). On the other hand, the magnetization of the 1.7 nm-thick film is reduced, indicating that the magnetically dead layer exists near the interface. To summarize, the $NiFe_2O_4$ thin films showed large y and reduced magnetically dead layers compared to $CoFe_2O_4$ thin films probably because of the high site selectivity of Ni ions.

1.4 Verwey transition in Fe_3O_4

Magnetite Fe_3O_4 has attracted strong attention for a long time as the first magnetic material in the era of ancient Greece, and also as a promising room-temperature half-metallic magnetic material for spintronic applications [30, 42]. The epitaxial Fe_3O_4/γ-Al_2O_3/Si(111) structures, which are almost the same structure studied in previous sections, were recently fabricated as a possible application for spin injection devices [43]. From the viewpoint of fundamental physics, there is a particularly attractive phenomenon in this material, that is the Verwey transition. Figure 1.10 shows the conductivity of a bulk Fe_3O_4 single crystal as a function of temperature [44]. The conductivity in Fe_3O_4 at room temperature is about $10^2\,\Omega^{-1}\mathrm{cm}^{-1}$ [45, 46], and this high conductivity for an oxide has been attributed to electron hopping between $Fe^{3+}(O_h)$ and $Fe^{2+}(O_h)$ ions [47]. In 1939, E. W. J. Verwey found that such electrical conduction was frozen at low temperature [48]. Upon cooling, the resistivity suddenly increased at $\sim$ 120 K (called the Verwey temperature T_V) by two orders of magnitude. Initially, this first-order phase transition was interpreted as a formation of the charge-ordered state of 2+ and 3+ valence states of Fe ions [47]. However, subsequent experimental studies have

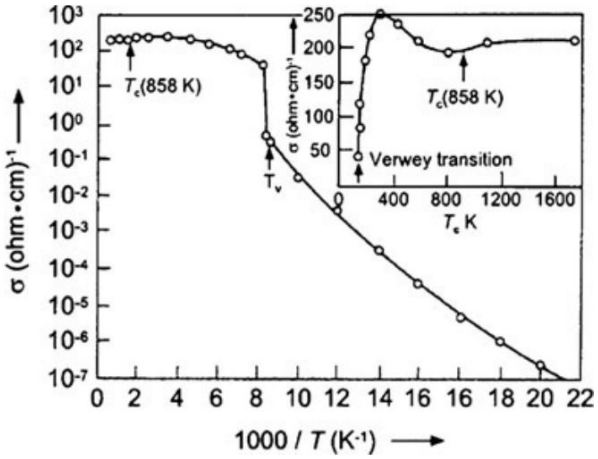

Figure 1.10: Conductivity of a bulk Fe_3O_4 single crystal as a function of temperature. Reproduced from Ref. [44].

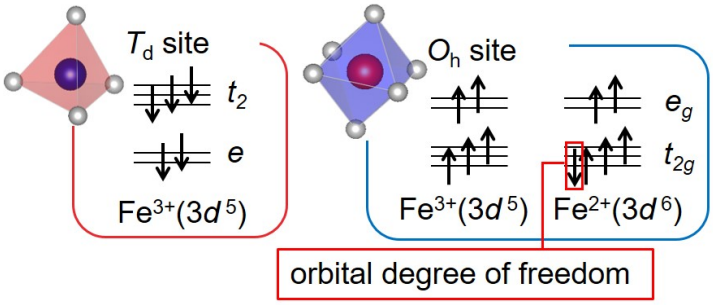

Figure 1.11: Electronic configuration of Fe_3O_4.

revealed that the above simple charge-order model is not sufficient [49–52]. Until now, the nature of the Verwey transition has remained a controversial issue for 80 years [44, 53]. Although it is still controversial, there is widely accepted consensus. Recent experimental and theoretical studies on the low-temperature phase ($T < T_V$) showed that a charge- and orbital-ordered states is realized [54–58], and the symmetry of the crystal structure is monoclinic Cc below T_V [59]. Here, the orbital degree of freedom in $t_{2g\downarrow}$ orbitals play a role in the orbital order (shown in Fig. 1.11). On the other hand, the ordered orbitals and their texture are still vague. The DFT calculation predicted real-number orbital orders (ROO), in which the

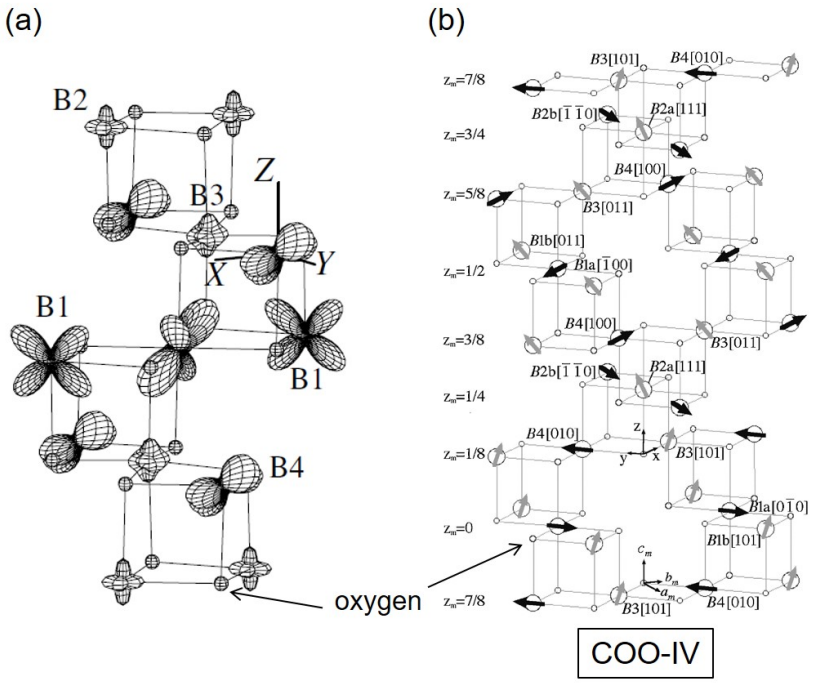

Figure 1.12: Proposed model for orbital order below T_V. For clarity, the T_d site is omitted. (a) ROO model proposed by Leonov *et al.*. Reproduced from Ref. [54]. The angular distribution of the Fe 3*d* electron in $t_{2g\downarrow}$ orbitals is illustrated. The size of orbital corresponds to its occupancy. (b) COO model proposed by Uzu and Tanaka [61,62]. The black and grey arrows represent the directions of orbital moments of Fe ions at the electron-rich and electron-poor sites, respectively. This COO model is labeled as 'COO-IV' in the original literature [61,62]. Reproduced from Ref. [61].

ordered orbitals are expressed by linear combinations of the spin-down d_{xy}, d_{yz}, and d_{zx} orbitals with real-number coefficients [54–56, 60]. For example, an ROO model proposed by Leonov *et al.* is shown in Fig. 1.12 (a). Also, complex-number orbital orders (COO), in which the ordered orbitals are expressed by linear combinations with complex-number coefficients, was proposed as a result of Hartree-Fock calculation [61,62]. Both models have predicted nearly correct local atomic displacement in the Verwey state compared with the experimental result of quasi single-domain micro XRD experiment [56, 59, 61, 63]. The most prominent

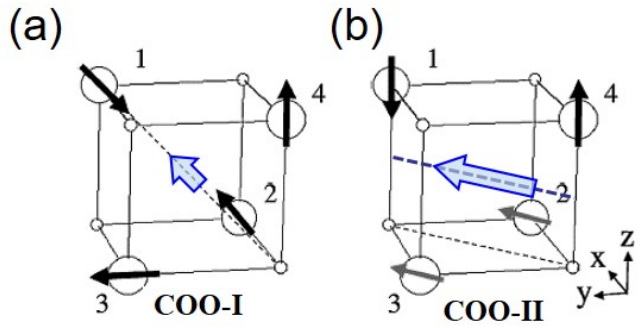

Figure 1.13: Two possible COO models 'COO-I' (a) and 'COO-II' (b) for short-range orbital order above T_{V}. Black arrows denote the orbital magnetic moments at the O_h site. Blue arrows denote average orbital magnetic moments. Adapted from Ref. [61].

difference between the ROO and COO models is the orbital magnetic moment. In the COO model, each Fe ion at the O_h site has a large orbital magnetic moment of about 0.5 μ_{B}, whereas a small orbital magnetic moment would be induced in the ROO state via spin-orbit interaction [61,62]. Here, the large orbital magnetic moments in the COO model are spatially arranged complicated pattern depending on its model parameters and, therefore, most of the orbital magnetic moments may be canceled out each other and the observed average orbital magnetic moment in the COO model depends on its model parameters. The COO model is shown in Fig. 1.12 (b), where arrows denote the orbital magnetic moment at O_h site.

Recently, resonant soft x-ray diffraction (RSXD) experiments on partially detwinned thin films revealed that the strongly lowered symmetry of the Fe 3*d* orbital order below T_V, which was consistent with the COO model [63, 64]. The COO model also predicts possible short-range orbital orders above T_{V}, which has been pointed out from the studies of neutron diffuse scattering [65–67]. Figure 1.13 (a) and (b) show the predicted short-range orbital orders above T_{V}. The black and blue arrows denote the local and averaged orbital magnetic moment, respectively. The averaged orbital magnetic moment of the COO-I and COO-II models are $0.09\mu_{\mathrm{B}} \parallel [111]$ and $0.24\mu_{\mathrm{B}} \parallel [110]$, respectively. These short-range orbital orders are expected to be randomly oriented and fluctuating and, therefore, there is no global symmetry lowering from cubic. However, the anisotropy of orbital mag-

netic moment arisen from the short-range orbital orders would be detectable by applying an external magnetic field and aligning the short range orbital orders. In the present thesis, detection of the short-range orbital order has been attempted by employing precise experimental and analysis methods. Details will be presented in Chapter 5.

1.5 Objectives and outlines of this thesis

As described above, there are many interesting phenomena in the spinel ferrites both from the technological application viewpoint and from the fundamental science point of view. Although the spin-filter structures using spinel ferrites are promising, experimentally obtained spin-filtering efficiency at room temperature is still not sufficient. One possible origin of the low spin-filtering efficiency is the magnetically dead layer of the spinel ferrites. So far, it has been revealed that, in addition to the APBs, the sudden decrease of inversion parameter y near the interface is thought to be an origin of the magnetically dead layer. However, it is still vague why the low inversion parameter degrades the ferrimagnetic order. Even though a Co ion replace the Fe ion at T_d site, strong antiferromagnetic coupling between O_h and T_d site still exist and the ferrimagnetic order would not be significantly affected. To address this issue, we have investigated the MFe$_2$O$_4$(111)/Al$_2$O$_3$(111)/Si(111) (M = Co, Ni) structures using XAS and XMCD. In Chapter 3, the magnetocrystalline anisotropy, which is intrinsic to the material and has a microscopic origin, at the magnetically dead layer of CoFe$_2$O$_4$ was investigated by angle-dependent XMCD. In order to redistribute cations, we have annealed the MFe$_2$O$_4$(111)/Al$_2$O$_3$(111)/Si(111) structures, and investigated how the electronic and magnetic states are changed, which will be presented in Chapter 4. From a viewpoint of fundamental science, the Verwey transition of Fe$_3$O$_4$ has also been studied. By using accurate experimental techniques, we have attempted to detect the short-range orbital order, which will be presented in Chapter 5.

Chapter 2

Experimental methods

2.1 X-ray absorption spectroscopy

Spectroscopic techniques provide rich information about materials. Numerous spectroscopic researches have been performed to investigate interesting phenomena in materials. The core-level spectroscopy is a class of the spectroscopic techniques using the excitation of core electrons. Since the energy levels of core electrons depend on element, one can selectively excite the core electrons by tunning the photon energy to the energy difference between the core and unoccupied states. This process is called x-ray absorption. By measuring the absorption intensity as a function of photon energy, one can element-specifically obtain a spectrum reflecting the density of states of the unoccupied states. This experimental method is known as x-ray absorption spectroscopy (XAS). In this section, we will focus on the principles of XAS.

2.1.1 Formulation

As stated above, the x-ray absorption process is the excitation of the core electrons to shallow unoccupied states and the XAS spectrum is the energy dependence of the excitation probability. Let us introduce the brief formulation about the excitation.

The Hamiltonian of an unperturbed potential V and electron in an electromag-

netic field created by the light is given by

$$\mathcal{H} = \frac{1}{2m}(\mathbf{p} + e\mathbf{A})^2 - e\phi + V. \tag{2.1}$$

Here, $m, \mathbf{p}$, and $-e$ are the mass, momentum, and charge of an electron, respectively and, $\mathbf{A}$ and ϕ are the vector and scalar potentials of the incident light, respectively. Equation (2.1) can be expanded to

$$\mathcal{H} = \frac{1}{2m}\left(\mathbf{p}^2 + e^2\mathbf{A}^2\right) + \frac{e}{2m}(2\mathbf{A}\cdot\mathbf{p} - i\hbar\nabla\cdot\mathbf{A}) - e\phi + V. \tag{2.2}$$

Here, the commutation relation $[\mathbf{A}, \mathbf{p}] = i\hbar\nabla\cdot\mathbf{A}$ has been used. Taking the radiation gauge ($\phi = 0, \nabla\cdot\mathbf{A} = 0$) and ignoring the $\mathbf{A}^2$ term, Eq. (2.2) can be rewritten as

$$\mathcal{H} = \frac{\mathbf{p}^2}{2m} + V + \frac{e}{m}\mathbf{A}\cdot\mathbf{p}. \tag{2.3}$$

Equation (2.3) can be regarded as the sum of an unperturbed Hamiltonian of an electron $\mathcal{H}_0 = \frac{\mathbf{p}^2}{2m} + V$ and a perturbed Hamiltonian $\mathcal{H}_{per} = \frac{e}{m}\mathbf{A}\cdot\mathbf{p}$. Therefore, applying the Fermi's golden rule to Eq. (2.3), the excitation probability from the initial state $|\psi_i\rangle$ to the final state $|\psi_f\rangle$ can be written as

$$w_{i\to f} = \frac{2\pi}{\hbar}|\langle\psi_f|\frac{e}{m}\mathbf{A}\cdot\mathbf{p}|\psi_i\rangle|^2\delta\left(E_f - E_i - h\nu\right). \tag{2.4}$$

Since we took the radiation gauge, $\mathbf{A}$ is expressed as $A_0\mathbf{e}\exp[-i\omega t]$ (where $\mathbf{e}$ is the polarization vector) in the long wavelength limit. Therefore, using the commutation relation $[\mathbf{r}, \mathcal{H}_0] = \frac{i\hbar}{m}\mathbf{p}$, the matrix element of Eq. (2.4) can be written as

$$\begin{aligned}\langle\psi_f|\frac{e}{m}\mathbf{A}\cdot\mathbf{p}|\psi_i\rangle &= \langle\psi_f|\frac{e}{m}A_0\mathbf{e}\cdot\frac{m}{i\hbar}[\mathbf{r}, \mathcal{H}_0]|\psi_i\rangle &(2.5)\\ &= \frac{eA_0}{i\hbar}(E_i - E_f)\langle\psi_f|\mathbf{e}\cdot\mathbf{r}|\psi_i\rangle. &(2.6)\end{aligned}$$

The absorption intensity is proportional to the summation of the excitation probability for all final states, as shown below.

$$I(h\nu) \propto \sum_f |\langle\psi_f|\mathbf{e}\cdot\mathbf{r}|\psi_i\rangle|^2\delta\left(E_f - E_i - h\nu\right). \tag{2.7}$$

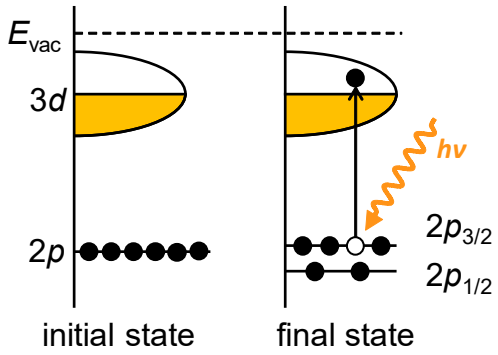

Figure 2.1: Schematic illustration of the initial and final state in a $2p$-$3d$ XAS process. E_{vac} denotes the vacuum level.

This is known as the electric dipole ($\mathbf{e} \cdot \mathbf{r}$) transition. The initial state is the ground state and the final state is the state with a core hole and an electron exited above the Fermi level. Figure 2.1 shows a schematic illustration of the initial and final states of the $2p$-$3d$ excitation for example. Since the unoccupied d states are determined by the local environment around the photoexcited atom, the XAS spectra reflect the valence, local symmetry, crystal-field splitting, hybridization with ligands, and so on. Therefore, by analyzing the XAS spectra, one can element-specifically investigate the electronic states of materials. The energy levels corresponding to the excitation from specific core levels are labeled as *K, L, M,* ... edges, named after the electron shells of the excited electron. In addition, the different angular momenta are further labeled by subscripts 1, 2, 3, ... in the descending order of their binding energies. For example in L edges, excitations from the $2s$, $2p_{1/2}$, and $2p_{1/2}$ levels are labeled as L_1, L_2, and L_3 edges, respectively.

2.1.2 X-ray magnetic circular dichroism and the sum rules

The absorption intensity of x rays by a material depends on the polarization of light. Especially, the difference in the absorption intensities between right- and left-handed circularly polarized light is called circular dichroism (CD). X-ray magnetic circular dichroism (XMCD) is the CD in the x-ray region under a magnetic field, as shown in Fig. 2.2(a). In the present study, XMCD signal is defined

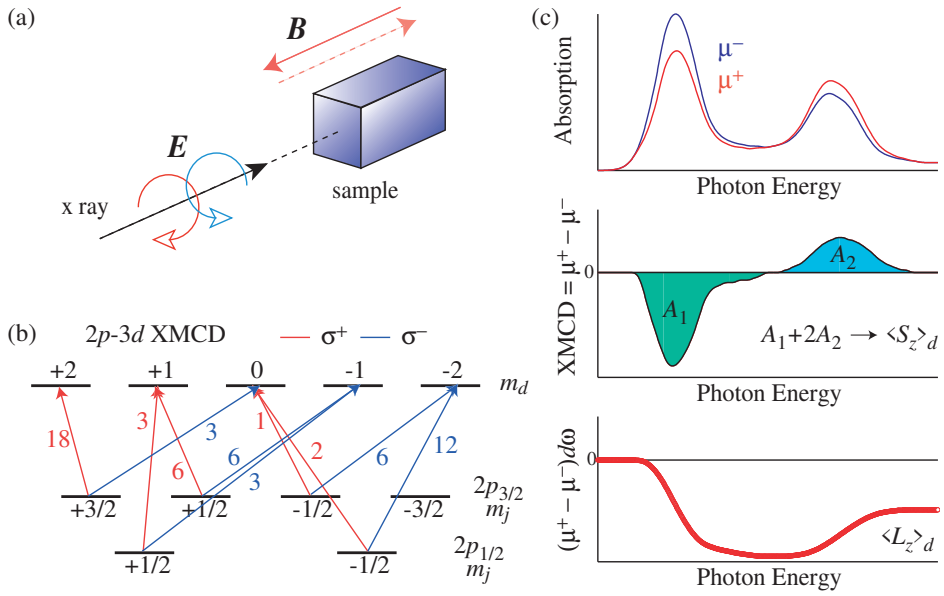

Figure 2.2: Schematic illustration of the $L_{2,3}$-edge XMCD experiment [68]. (a) Typical experimental geometry of the XMCD measurement. (b) $2p$–$3d$ relative transition probabilities for right- (red) and left-handed (blue) circular polarized light of the $3d$ transition-metal element. (c) (top) XAS spectra of right- and left-handed polarized light (μ^+, μ^-), (middle) XMCD spectrum ($\mu^+ - \mu^-$), and (bottom) the integral of the XMCD spectrum with respect to the photon energy. The spin and orbital magnetic moments can be obtained from these spectra by using the sum rules [69, 70].

by

$$\mathrm{XMCD}(h\nu) = I\left(h\nu, \mu^{+}\right) - I\left(h\nu, \mu^{-}\right). \tag{2.8}$$

Here, μ^{+} and μ^{-} are the absorption coefficients for right- and left-handed circular polarized light, respectively, and they are defined by the helicity $h = +1$ and $h = -1$. If the $3d$ electrons are spin-polarized, the transition probabilities from the $2p$ core to $3d$ levels depend on the electron orbitals of the initial and final states, as shown in Fig. 2.2 (b). Therefore, the XMCD spectra contain information about magnetic states of $3d$ electrons in addition to the information from XAS spectra.

Calculating the transition probabilities quantitatively based on the localized model, the orbital and spin sum rules have been derived by Thole *et al.* [69] and Carra *et al.* [70], respectively. The derived relationships are

$$m_{\mathrm{orb}}^{\mathrm{proj}} = -\frac{4\int_{L_3+L_2}\left(\mu^{+}-\mu^{-}\right)d\nu}{3\int_{L_3+L_2}\left(\mu^{+}+\mu^{-}\right)d\nu}\left(10-n_d\right)\mu_{\mathrm{B}}, \tag{2.9}$$

and

$$m_{\mathrm{spin}}^{\mathrm{proj}} - 7m_{\mathrm{T}}^{\mathrm{proj}} = -\frac{2\int_{L_3}\left(\mu^{+}-\mu^{-}\right)d\nu - 4\int_{L_2}\left(\mu^{+}-\mu^{-}\right)d\nu}{\int_{L_3+L_2}\left(\mu^{+}+\mu^{-}\right)d\nu}\left(10-n_d\right)\mu_{\mathrm{B}}. \tag{2.10}$$

Here, $m_{\mathrm{orb}}^{\mathrm{proj}}$, $m_{\mathrm{spin}}^{\mathrm{proj}}$, and $m_{\mathrm{T}}^{\mathrm{proj}}$ are the orbital magnetic moment, spin magnetic moment, and an additional term called 'magnetic dipole moment' [71], respectively. L_3 (L_2) denotes the $2p_{3/2} \rightarrow 3d$ ($2p_{1/2} \rightarrow 3d$) absorption edge and n_d is the number of $3d$ electrons. It should be noted that, in Eqs. (5.2) and (5.3), $m_{\mathrm{orb}}^{\mathrm{proj}}$, $m_{\mathrm{spin}}^{\mathrm{proj}}$, and $m_{\mathrm{T}}^{\mathrm{proj}}$ are the magnetic moments projected along the incident x-ray direction, that is, only the magnetization component parallel to the x-ray momentum is obtained. Although the existence of the m_{T} term in Eq. (5.3) limits the quantitative determination of the spin moment in general, this term is negligible for ions with cubic symmetry [72–74]. The validity of these sum rules was confirmed by Chen *et al.* for Fe and Co metal [75]. They measured the XMCD spectra of *in-situ* grown Fe and Co thin films with transmission method, and applied these sum rules to the spectra ignoring the m_{T} term. The obtained spin and orbital magnetic moments which were in good agreement with the individual moments obtained from Einstein–de Haas gyromagnetic ratio measurements [76].

Using the XMCD sum rules, one can independently determine the spin and orbital moments from the XAS and XMCD spectra. Since these spectra are element-specific, XMCD is a powerful tool to study the magnetism of materials including different magnetic elements such as the spinel ferrites.

2.1.3 Correction factors for the spin sum rule

The applicability of the spin sum rule to light transition-metal ions is limited because of the overlapping absorption L_2 and L_3 peaks. As given by Eq. (5.3), the spin sum rule needs the integral of the XMCD spectra at the L_2 and L_3 edges [$\int_{L_2} (\mu^+ - \mu^-)\, d\nu$ and $\int_{L_3} (\mu^+ - \mu^-)\, d\nu$] individually. Therefore, the overlap between the L_2 and L_3 edges causes the underestimation of the spin magnetic moment. In particular, in the light transition-metal ions, due to the weak spin-orbit coupling in the $2p$ core level, the separation of the core levels into the L_2 and L_3 edges becomes even more difficult, lowers the accuracy of the spin sum rule [77].

Teramura *et al*. [77] have calculated the XAS and XMCD spectra of transition-metal ions with various valences, and have evaluated the ratio of the spin magnetic moment deduced from the XMCD integral X_I [the right-hand side of Eq. (5.3)] to the calculated value X_E (the left-hand side). The ratio X_I/X_E can be used as a correction factor to deduce the true spin magnetic moment from the experimentally-obtained one from the sum rule. The evaluated values are listed in Table 2.1. The application of this method, however, is impossible for Mn^{3+}, Cr, and V because of too strong overlap of the L_2 and L_3 edges.

2.1.4 Detection methods

There are several methods to measure the absorption intensity, as shown in Fig. 2.3. The most direct method to determine the absorption coefficient of x rays, is to measure the intensities of the incident and transmitted light. However, it is hard to be applied in the soft x-ray region because of the small penetration depth (a few hundred nm). Therefore, other physical quantities proportional to the absorption intensity are alternatively measured. As stated in section 2.1.1, the XAS process creates core holes. The core holes are unstable and then decay after a certain lifetime. Therefore, electrons or fluorescence photons are emitted as a result of

Table 2.1: "Correction factors" X_I/X_E evaluated for transition-metal ions with various valence states, and the ground-state expectation values of the orbital angular momentum operator L_z, the spin operator S_z, and the magnetic dipole operator T_z calculated with $10Dq = 1.5$ eV. Reproduced from [77].

	n	$\langle L_z \rangle$	$\langle S_z \rangle$	$\langle T_z \rangle$	X_I/X_E
Ni^{2+}	8	−0.264	−0.995	−0.00291	0.921
Ni^{3+}	7	−0.788	−0.969	0.00491	0.923
Co^{2+}	7	−0.812	−1.01	0.00452	0.921
Co^{3+}	6	−0.711	−1.65	0.0195	0.874
Fe^{2+}	6	−0.736	−1.69	0.0126	0.875
Fe^{3+}	5	−0.002	−2.50	0.00048	0.685
Mn^{2+}	5	−0.002	−2.50	0.00031	0.680
Mn^{4+}	3	0.176	−1.50	0.00015	0.587

the decay process. By counting them, one can alternatively obtain absorption signals which are proportional to the number of core holes.

The measurement mode which counts the number of electrons is called electron-yield (EY) mode. The EY mode can be classified into two methods. The most simple method is to measure the drain current, namely, the number of all the emitted electrons. This method is called the total electron-yield (TEY) mode. The other method is to count the number of electrons of certain energies using an energy analyzer or a retarding voltage, which is known as partial electron-yield (PEY) mode. Since the mean free path of electrons depends on the energy, the probing depth is tunable in the PEY mode [78]. In the TEY mode, since the low-energy secondary electrons also contribute to the signal, one can obtain a larger signal than that of the PEY mode. Because of the larger signal and the simpler measurement configuration, the TEY mode is commonly used for the XAS measurements in the soft x-ray region. The probing depth of the TEY mode is known as a few nm (typically $\sim$ 5 nm, thouhg it depends on material) [79].

The method which measures the intensity of fluorescence photons is called the

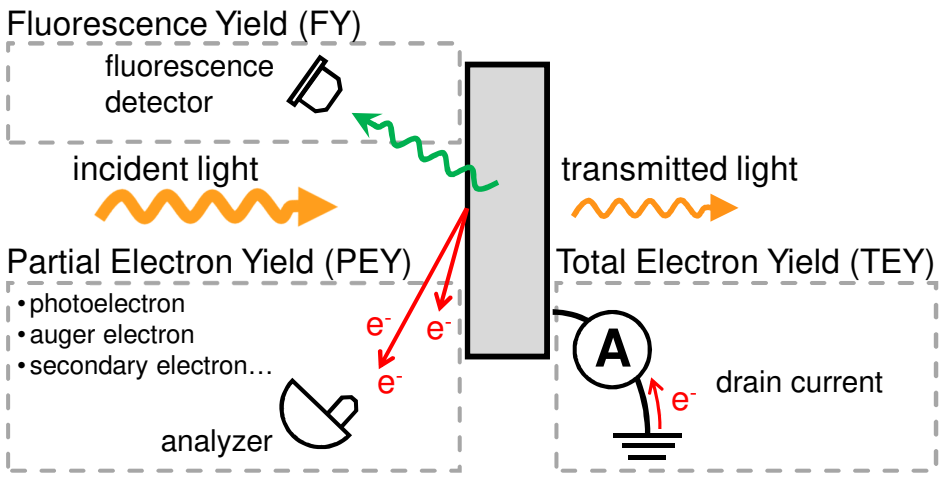

Figure 2.3: Detection methods of the x-ray absorption intensity.

fluorescence-yield (FY) mode. Similarly to the electron-yield mode, this mode can be classified to the partial and total fluorescence-yield (PFY and TFY) mode. The PFY and TFY modes measure the photons of certain and all energies, respectively. The PFY mode can remove undesired background signals such as reflected incident x-ray beam. Since the FY mode uses only photons, probing depth is as large as the penetration depth of x rays ($\sim$ 100 nm or more). Therefore, it is used as a bulk-sensitive method. However, in concentrated bulk samples, the measured FY signal is not proportional to the absorption coefficient. In particular, the intensities of prominent absorption peaks are significantly reduced. This effect is called the self-absorption effect [80]. Actually, the same effect weakly occurs in the EY mode, which is known as a saturation effect. Because of its weakness, the saturation effect in the EY mode is often ignored. However, in the case of grazing-incidence geometry, this effect is not negligible [81]. Figure 2.4 (a) shows a schematic illustration of the principle of the saturation effect. The left panel shows the x-ray intensity at the depth z. Since the x rays passed certain distance in the material, the intensities of the incident x rays are reduced at deep inside the material, especially at the photon energy of prominent absorption

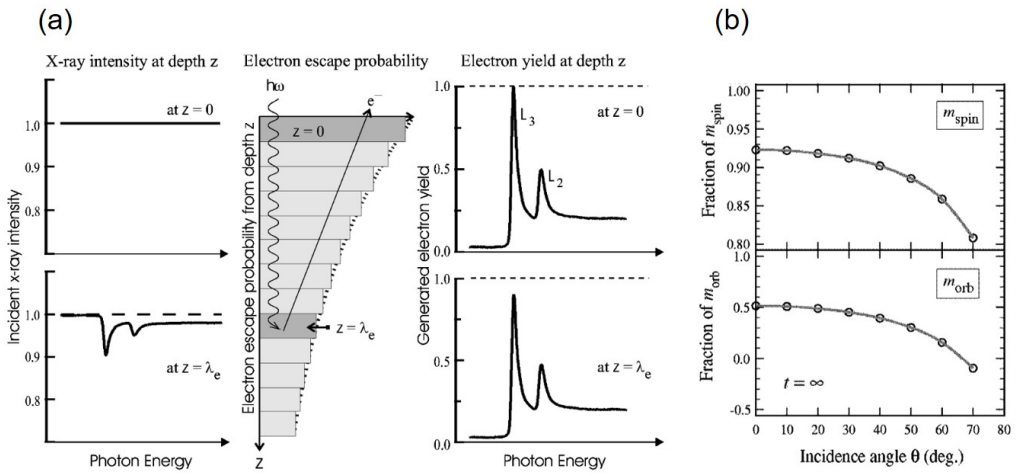

Figure 2.4: Illustrations and model calculation for the saturation effect. Reproduced from Ref. [81]. (a) Schematic illustration of the principle of the saturation effect. (b) Model calculation of how the saturation effect changes the results of sum rules in bulk Fe metal. The spin magnetic moment (m_{spin}) and the orbital magnetic moment (m_{orb}) obtained by the sum rules are plotted as a function of x-ray incidence angle (0° for the normal incidence).

peaks. Therefore, the prominent absorption peaks in the electron yield spectrum are also reduced (right panel). The contributions from these distorted spectra to the total spectrum are the origin of the saturation effect (center panel). In the case of grazing incidence, the intensity of the x rays at z is more distorted because the x rays pass a longer distance in the material. Therefore, the total spectrum gets more distorted. Figure 2.4 (b) shows a model calculation of how the saturation effect changes the results of sum rules. The spin and orbital magnetic moments decrease with increasing incidence angle.

2.2 Configuration interaction cluster-model calculations

In order to analyze the spectral line shape of the XAS and XMCD spectra, model-based calculation techniques are useful. Atomic multiplet calculation is a method

to calculate the electronic structure of an ion under a crystal field. In this method, one can explicitly take account of intra-atomic $3d$-$3d$ Coulomb interactions (including an exchange interaction), and reproduce multiplet structures.

The cluster-model calculation is a method to calculate the electronic structure of a 'cluster' which consists of a central ion and surrounding ligands, as shown in Fig. 2.5. In this model, in addition to atomic multiplet calculation, the interaction between the central-ion and the ligands and charge transfer between them are explicitly taken into account. On the other hand, inter-cluster interaction and charge transfer are not considered. Therefore, this model is most suitable for localized electron systems. In the present study, the central ion is a transition metal (TM) ion and the ligand is oxygen.

One-electron transfer integrals between the TM $3d$ and O $2p$ orbitals are expressed using Slater–Koster parameters $(pd\sigma)$ and $(pd\pi)$, which represent the strength of TM $3d$–O $2p$ hybridization. The one-electron transfer integrals for O_h symmetry (MO$_6$ cluster) is given by [82]

$$T_{t_{2g}} = 2(pd\pi),\ T_{e_g} = -\sqrt{3}(pd\sigma), \tag{2.11}$$

and those for T_d symmetry (MO$_4$ cluster) by [83]

$$T_{t_2} = \sqrt{\frac{4}{3}(pd\sigma)^2 + \frac{8}{9}(pd\pi)^2},\ T_e = \frac{2\sqrt{6}}{3}(pd\pi). \tag{2.12}$$

Here, the subscripts of T denote the symmetry of hybridizing orbitals. There is an approximate relationship between the two Slater–Koster parameters: $(pd\sigma)/(pd\pi) = -2.17$ [82]. In our calculation, the transfer integrals T's have been adjusted only by $(pd\sigma)$, and $(pd\pi)$ has been calculated using the above relationship.

In order to treat multi-electron states more precisely, different electronic configurations of the TM $3d$ and O $2p$ orbitals are taken into account. Then the wave function of the ground state of the $3d^n$ configuration can be written as a linear combination of basis functions which represent O $2p$-to-TM $3d$ charge-transferred states:

$$\psi_N^{\mathrm{CI}} = C_0\psi(d^n) + C_1\psi(d^{n+1}\underline{L}) + C_2\psi(d^{n+2}\underline{L}^2) + \cdots . \tag{2.13}$$

Here, $\underline{L}$ denotes a hole in the ligand O $2p$ orbitals. The wave function of the excited state is also expanded using the basis functions in a similar way to Eq.

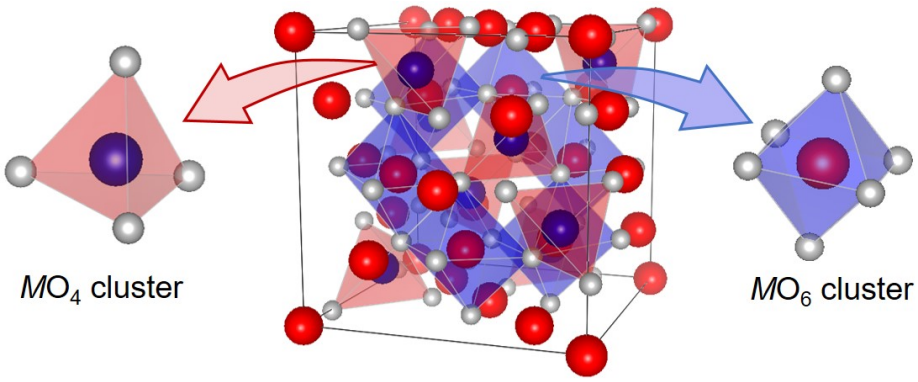

Figure 2.5: MO_4 and MO_6 clusters extracted from a solid.

(2.13). In the present study, terms up to C_3 have been taken into account. This method is called the configuration interaction (CI) theory. The charge-transfer energy between TM $3d$ and O $2p$ is defined as an energy difference between the d^n and $d^{n+1}\underline{L}$ configurations, which is written as

$$\Delta \equiv E(d^{n+1}\underline{L}) - E(d^n). \tag{2.14}$$

Also, intra-atomic $3d$–$3d$ Coulomb energy U_{dd} is defined as

$$U_{dd} \equiv E(d^{n-1}) + E(d^{n+1}) - 2E(d^n). \tag{2.15}$$

Here, $E(d^{n+1}\underline{L})$, $E(d^n)$,and $E(d^{n\pm1})$ denote the center-of-gravity energy of multiplets of individual configurations. The ionic Hartree-Fock values have been adopted for the $2p$ and $3d$ spin-orbit interaction and 80% of the values for the Slater integrals [84]. The molecular field $\mu_0 H_{\mathrm{mol}}$ is assumed to be 0.07 eV along the cubic [001] direction. The intra-atomic $3d$–$2p$ Coulomb energy U_{dc} is assumed to be $U_{dc} = 1.3\,U_{dd}$. This relationship is consistent with many experimental results [85].

2.3 Experimental setup

All the XMCD measurements in this thesis were performed at the BL-16A of Photon Factory [86], the High Energy Accelerator Research Organization (KEK-

Table 2.2: The available energy range in the various polarization modes at the BL-16A of KEK-PF [86].

Polarization	Energy range (eV)
Circular	297–1000
Linear (Horizontal)	180–1500
Linear (Vertical)	380–1500
Elliptical	218–1500

PF). In this section, I will describe the details of the beamline and apparatuses therein.

2.3.1 Photon Factory BL-16A

The BL-16A is a soft x-ray beamline designed for the various spectroscopic techniques including XAS, XMCD, magnetic linear dichroism, and resonant scattering. The beamline is equipped with two Apple-II type undulators in a tandem configuration, which provide circularly, linearly, and elliptically polarized x-rays in the range of 200–1500 eV. Detailed energy ranges for each polarizations are summarized in Table 2.2. A typical photon flux is about 1×10^{11} photons/s when the energy resolution $E/\Delta E$ is 8000. A typical beam-spot size at the focus position is $\sim$ 0.1–0.2 and $\sim$ 0.2–0.5 mm in the vertical and horizontal directions, respectively. The beamline optics of the BL-16A is schematically illustrated in Fig. 2.6. The photon energy is scanned using a varied-line-spacing grating (VLSG). The x rays which generated in the undulators are guided to the VLSG by a pre-focusing mirror M0, an entrance slit S1, a cylindrical mirror M1, and a plane mirror M2. After being diffracted in the VLSG, x rays are guided to the focus positions F1, F2, and F3 by a plane mirror Mp, an exit slit S2 (S2'), and post-focusing mirror M3 (M3'). Here, the Mp changes the direction of the x rays into one of the two branch beamlines BL-16A1 and BL-16A2. Fast polarization switching (at 10 Hz) is available in this beamline. The principle of fast polarization switching using the tandem undulators is schematically illustrated in Fig. 2.7. By changing the electron trajectory using the kicker magnets, one can quickly switch the x-ray

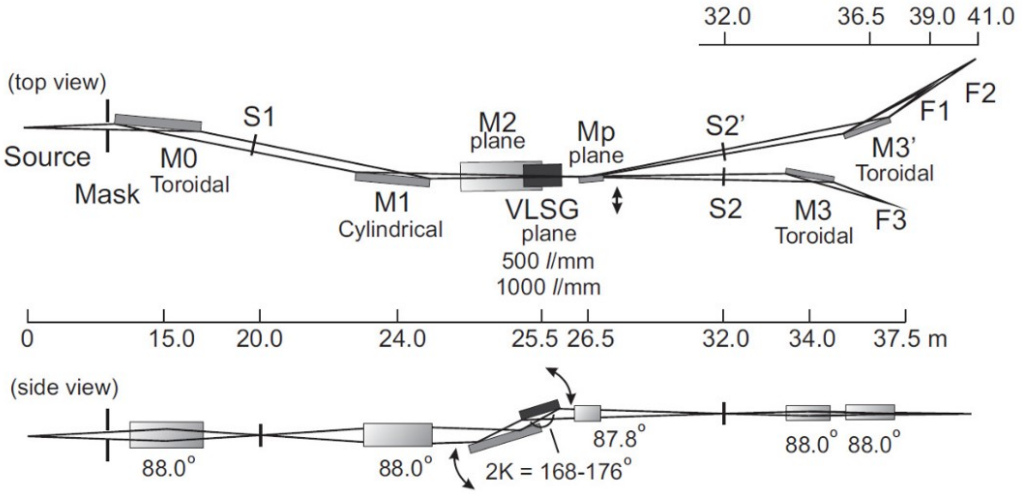

Figure 2.6: Schematic illustration of the beamline optics at the BL-16A, KEK-PF. Reproduced from [87].

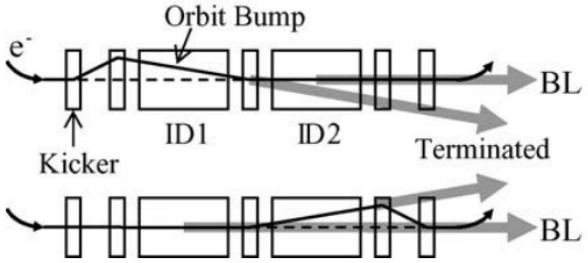

Figure 2.7: Schematic illustration of the method for fast polarization switching using the tandem undulators and kicker magnets. Reproduced from [88].

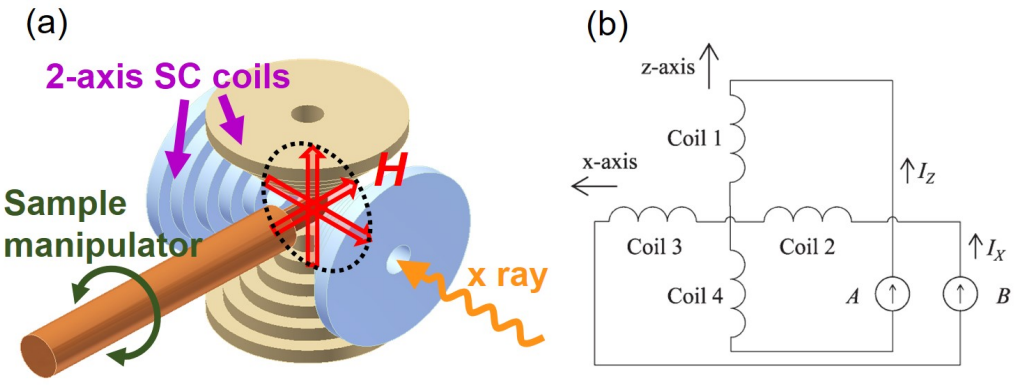

Figure 2.8: (a) Schematic illustration of the vector-magnet XMCD apparatus. Adapted from Ref. [90]. (b) Circuit configuration of the vector-magnet XMCD apparatus. Bipolar current sources A and B control the magnetic fields generated by the two pairs of magnets. Reproduced from Ref. [89].

source between the two undulators ID1 and ID2. Thus, fast circular polarization switching is achieved by setting the polarizations of ID1 and ID2 to the left- and right-handed circular polarization, respectively.

2.3.2 Vector-magnet XMCD apparatus

In a typical XMCD apparatus, the magnetic field can be applied only parallel or antiparallel to the incident x-ray beam. Therefore, one has to rotate the sample to measure the angle dependence of the XMCD spectra. However, this results in the change of the incident angle of the x rays. Therefore, the magnitude of the extrinsic saturation effect (see section 2.1.4) also changes. This extrinsic effect makes it difficult to discuss the true anisotropy of the XMCD spectra. If the magnetic field is rotatable, one can fix the incident angle and, therefore, the change of saturation effect can be eliminated from the angle dependence. In this section, I will describe an XMCD apparatus called 'vector-magnet XMCD apparatus', which allows us to rotate the magnetic field [89, 90].

Figure 2.8 (a) shows the schematic illustration of the vector-magnet XMCD apparatus installed at the BL-16A. Two pairs of superconducting (SC) magnets are orthogonally arranged along the vertical and horizontal directions. The horizontal

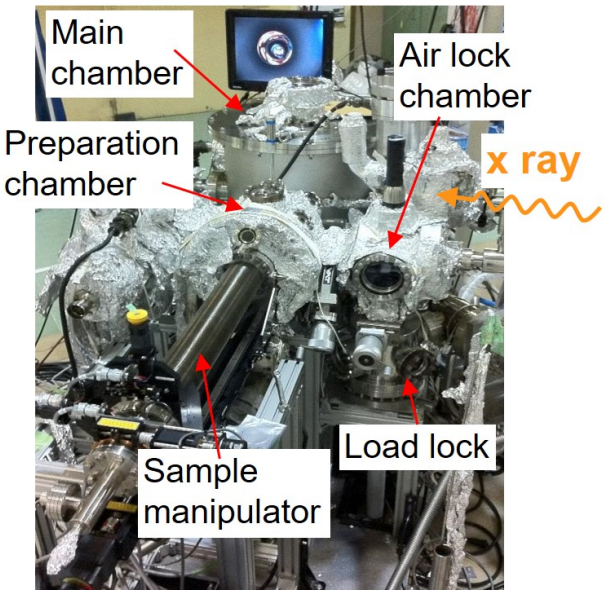

Figure 2.9: Overview of the vector-magnet XMCD apparatus.

magnet is aligned parallel to the x-ray incident direction. Figure 2.8 (b) shows the circuit diagram of the vector-magnet XMCD apparatus. By tuning the magnitudes of magnetic fields generated by the two pairs of magnets independently, one can control the magnitude and direction of the magnetic field at the sample position (the center of the two magnets). Figure 2.9 shows the overview of the vector-magnet XMCD apparatus. The apparatus is composed of four chambers: the load lock chamber, the air lock chamber, the preparation chamber, and the main chamber. The sample temperature is controlled by a liquid-helium cryostat down to $\sim$ 20 K. The absorption signal is detected in the TEY mode.

2.3.3 5 T-magnet XMCD apparatus

An XMCD apparatus, which is equipped with a high magnetic-field superconducting magnet, is installed at BL-16A. One can apply the magnetic field up to 5 T parallel or antiparallel to the incident x-ray beam. Figure 2.10 shows an overview of the apparatus. The apparatus is composed of three chambers: the load lock chamber, the preparation chamber, and the main chamber. The magnetic-field di-

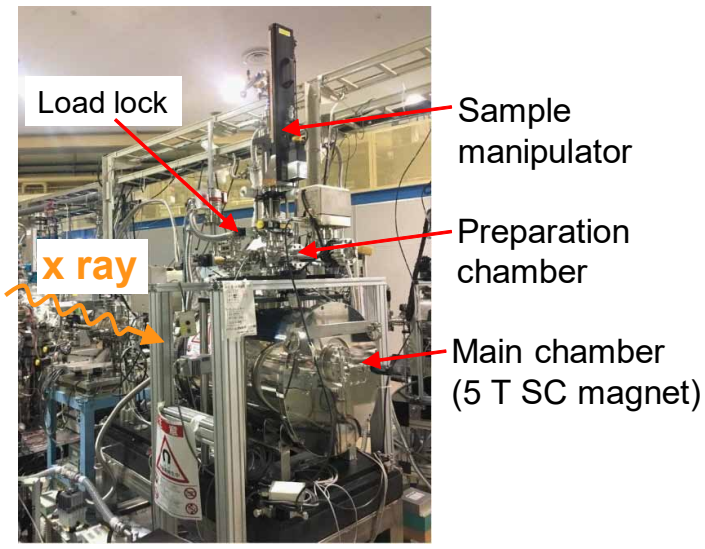

Figure 2.10: Overview of the 5 T-magnet XMCD apparatus.

rection relative to the sample can be adjusted by rotating the sample using the manipulator. The sample temperature is controlled by a liquid-helium cryostat down to ~ 30 K [86]. Both the TEY and FY measurement modes are available.

Chapter 3

Angle-dependent XMCD study of $CoFe_2O_4$ thin films

3.1 Introduction

Spintronic devices are attracting strong attention as next-generation electronic devices in order to realize highly efficient information processing and storage using the spin degrees of freedom in addition to the charge degree of freedom. Among them, Si-based spintronic devices have significant advantages because of the compatibility to the nowadays mature Si-based nanotechnologies. However, there are problems to realize such devices. A highly spin-polarized current injection into Si is a crucial but technically difficult issue. Spin filters are thought to be a promising way to break through it [25]. So far, highly efficient spin-filter structures (nearly 100%) have been achieved using Eu chalcogenides [91, 92]. However, the high spin polarization can be achieved only below 10 K. Therefore, spin-filter structures composed of a magnetic insulator which has a spontaneous magnetization at room temperature is required. Recently, epitaxial $CoFe_2O_4(111)$ thin films were grown on Si(111) substrates using γ-Al_2O_3 buffer layers [39]. Since $CoFe_2O_4$ is an insulating ferrimagnet with a high Neel temperature over 790 K [11] and its spin-dependent band gap [33] can be used as a spin-dependent barrier for tunneling electrons, this is a promising spin injector to Si. Although the $CoFe_2O_4(111)/Al_2O_3(111)$ bilayer is promising, experimentally obtained spin-filtering efficiency at room temperature is still low as estimated from the tunnel

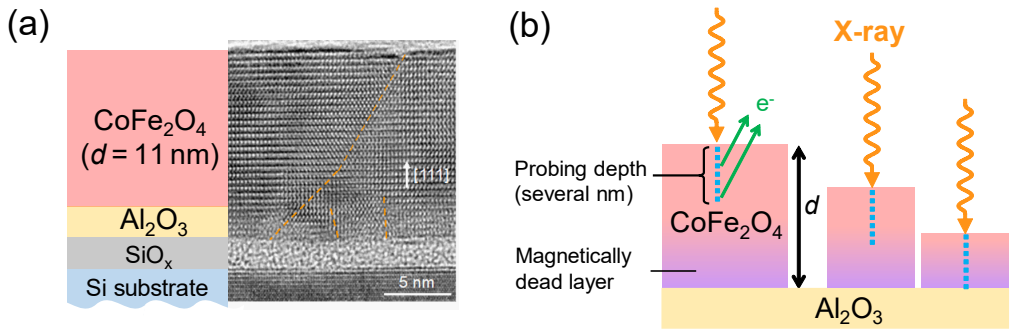

Figure 3.1: Schematic pictures of the sample structure and the method to probe the magnetically dead layers. (a) Schematic picture and cross sectional TEM image of $CoFe_2O_4(111)/Al_2O_3(111)/Si(111)$ structure (d = 11 nm), adapted from Ref. [40]. (b) Illustration of the way to probe the magnetically dead layers near the interface. By changing the thickness of the $CoFe_2O_4$ layer, one can see the effects from the magnetically dead layer as a thickness dependency.

magnetoresistance ratio [27, 29, 30]. Possible origins of the low spin-filtering efficiency have been pointed out in many reports. Structural and/or chemical defects form impurity states in the spin-dependent gap, resulting in the reduced exchange splitting [31–33]. The degradation of magnetic properties at the interface between the spinel ferrites and the substrates, so-called magnetically dead layer, are also reported in Fe_3O_4 thin films [35, 36, 38], where antiphase boundaries are pointed out as an origin of the degradation. Recently, Wakabayashi *et al.* have fabricated $CoFe_2O_4(111)/Al_2O_3(111)/Si(111)$ structures with a few-nanometer-thick $CoFe_2O_4$ layers, which are thin enough for electron tunneling [40]. A schematic illustration of the structure is shown in Fig. 3.1 (a). The $CoFe_2O_4$-thickness dependence of x-ray absorption spectroscopy (XAS) spectra and x-ray magnetic circular dichroism (XMCD) spectra have revealed the formation of the magnetically dead layer and sudden change of cation distribution near the interface between $CoFe_2O_4$ and Al_2O_3. The way to probe the magnetically dead layers is illustrated in Fig. 3.1 (b). Since they employed total the electron yield (TEY) mode to detect the absorption signal, several-nanometer region from the surface was probed [79, 93]. By reducing film thicknesses from 11 nm to 1.4 nm, they could obtain the XAS and XMCD spectra reflecting the magnetically dead layers near

the interface between $CoFe_2O_4$ and Al_2O_3 buffer layers. Note that the effects from the surface may also be included in the probed signals. However, the surface effect would equally contribute to the results at all the thicknesses and, therefore, observed thickness dependence should arise from the film/substrate interface. This is also supported by the fact that the sudden change of cation distribution was observed below 4 nm-thick film whose thickness was comparable to the probing depth of TEY mode (see 1.8 (e)). In the present study, in order to obtain more detailed information about the magnetic and electronic properties of magnetically dead layers such as the magnetocrystalline anisotropy, we have investigated these thin films by using angle-dependent XMCD measurements [90].

3.2 Experimental Methods

Epitaxial $CoFe_2O_4(111)$ thin films (thicknesses d = 1.4, 2.3, 4, and 11 nm) were grown on a 2.4 nm-thick γ-$Al_2O_3(111)$ buffer layer/n^+-Si(111) substrate using pulsed laser deposition (PLD) by Dr. Yuki. K. Wakabayashi and Prof. Ryosho Nakane of the University of Tokyo. In order to avoid charging up of the samples during the XAS and XMCD measurements, we used highly phosphorus-doped Si(111) wafers with a low resistivity of 2 mΩ cm as the substrates. For the epitaxial growth of the γ-Al_2O_3 buffer layers on the Si substrates, we used solid-phase reaction of Al and SiO_2. More detailed description of sample preparation and characterization are provided in Ref. [40].

Magnetic field-angle dependent XAS and XMCD measurements were performed at room temperature ($\sim$ 300 K) using the vector-magnet XMCD apparatus installed at the undulator beamline BL-16A of Photon Factory, the High Energy Accelerator Research Organization (KEK-PF). The absorption signals were detected in the TEY mode. The XMCD signals were collected by switching the photon helicity in 10 Hz [94]. In order to eliminate the saturation effect [81] which induces an extrinsic angle dependency to spectral line shapes, we fixed the x-ray incident angle at 45° and applied the magnetic field of 0.7 T to various directions. The geometry of the present measurements is illustrated in Fig. 3.2 (a). The magnetic-field angle θ_H and magnetization angle θ_M are defined as an angle measured from the surface normal.

3.3 Results and Discussion

Figures 3.2 (b) and (c) show the Fe $L_{2,3}$-edge XAS ($\mu^+ + \mu^-$) and XMCD ($\mu^+ - \mu^-$) spectra of the 11 nm-thick $CoFe_2O_4$ thin film for various θ_H. Here, μ^+ (μ^-) denotes the absorption coefficient for photons whose helicity is parallel (antiparallel) to the majority-spin direction. The XAS spectra do not show notable θ_H dependence. The XMCD intensity systematically changes depending on θ_H. Since the XMCD intensity is proportional to the projected magnetic moment onto the x-ray incident direction ($M_{\mathrm{proj}} = M\cos(\theta_M - 45°)$), this change reflects the magnetization direction θ_M under varying θ_H. Since the total magnetic moment and Fe $L_{2,3}$-edge XMCD spectra of these samples were already obtained [40], we deduced M_{proj} from the XMCD intensities. Figure 3.2 (d) shows the θ_H dependence of M_{proj} and a simulation without magnetic anisotropy. If the magnetization of this film is fully aligned by magnetic field, θ_H should be qual to θ_M, and thus M_{proj}/M should be $\cos(\theta_H - 45°)$. This simulation is corresponding to a simulation using only the first term of following equation (Eq. 3.1). Experimental data shows a clear deviation from the simulated curve (gray dashed curve). This indicates that the measured angle dependence reflects the magnetic anisotropy of the 11 nm-thick $CoFe_2O_4$ film.

In order to analyze the obtained θ_H dependence of M_{proj}, we have simulated their behavior based on a model which is similar to the Stoner-Wohlfarth model [90, 95]. The Stoner-Wohlfarth model [95] is a classical model for ferromagnets with uniaxial magnetic anisotropy under an external magnetic field. Here, the magnetic energy is described as the sum of the Zeeman energy and the magnetic anisotropy energy. In addition, one can classify the magnetic anisotropy into two major contributions. One is the magnetocrystalline anisotropy (MCA), which is intrinsic to the material and has a microscopic origin, and the other is the shape anisotropy (SA), which originates from the demagnetization field. For magnetic thin films, the magnetic energy E is thus given by

$$E = -\mu_0 MH\cos(\theta_M - \theta_H) + \frac{\mu_0}{2}M^2\cos^2\theta_M + E_{\mathrm{MCA}}. \tag{3.1}$$

Here, μ_0 and M are the vacuum permeability and magnetization, respectively, and the other variables are defined in Fig. 3.2 (a). The first, second, and third terms denote the Zeeman, SA, and MCA energy, respectively. By minimizing E with

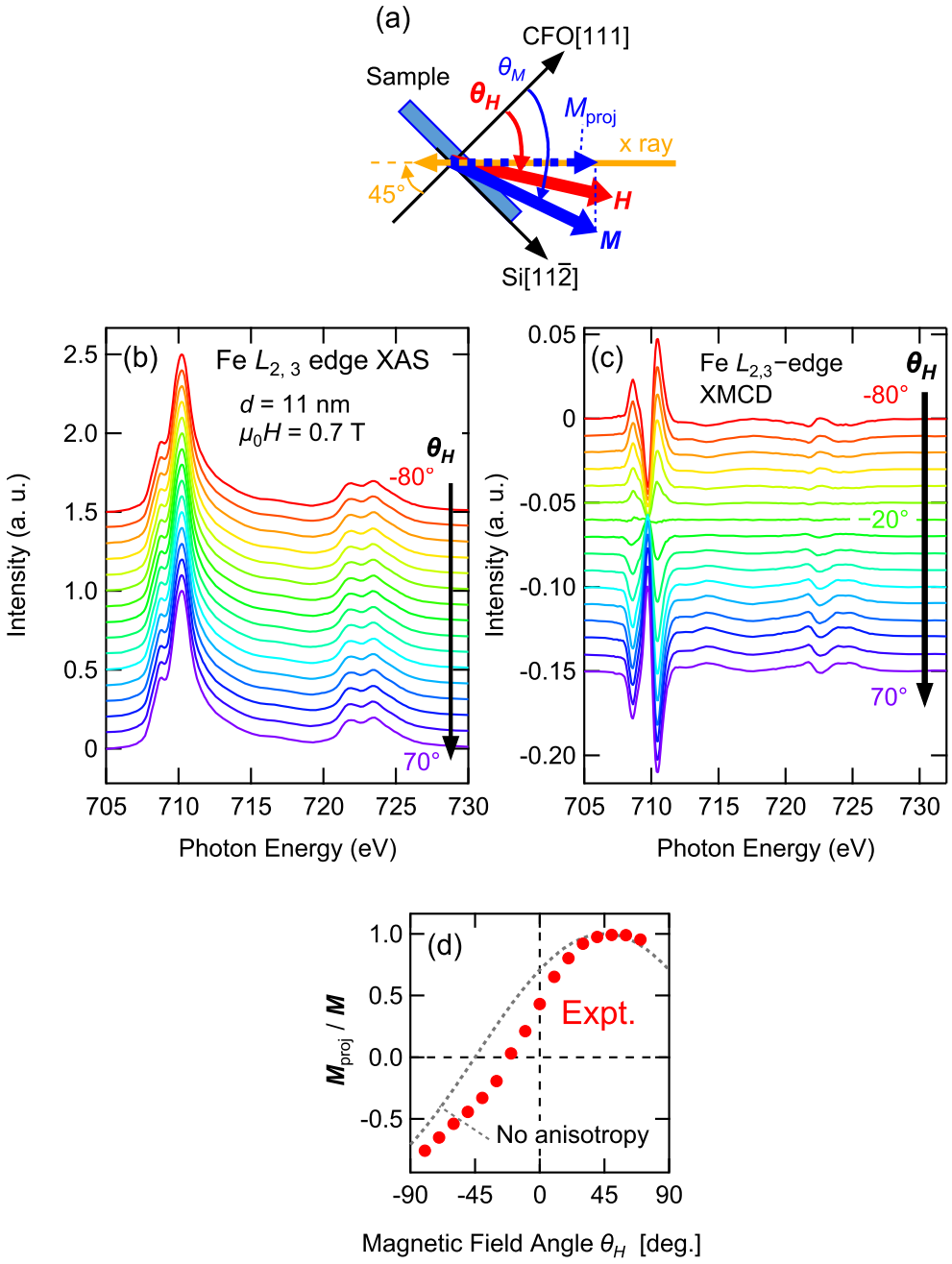

Figure 3.2: Angle-dependent XMCD of 11 nm-thick $CoFe_2O_4$ film at the Fe $L_{2,3}$ edges. (a) Experimental geometry of the angle-dependent XMCD measurements. (b), (c) XAS and XMCD spectra for various θ_H. (d) θ_H-dependence of the relative magnetic moment projected onto the x-ray incident axis, deduced from the L_3-edge XMCD intensity (see main text). The gray dashed curve ($\cos(\theta_H - 45°)$) shows a simulation for a magnetically isotropic situation.

respect to θ_M for each θ_H, one can obtain θ_M as a function of θ_H, then the M_{proj} observed by XMCD can be calculated as $M\cos(\theta_M - 45^\circ)$. Since $CoFe_2O_4$ has a cubic MCA in addition to the uniaxial anisotropy and there are crystal domains in the present samples [40], the MCA term cannot be simulated by such a simple model as the Stoner-Wohlfarth model. Therefore, we have simulated M_{proj} based on only the Zeeman and SA terms, and discuss the MCA as a difference between the measured M_{proj} and the simulated one. It should be noted that the M depends on thicknesses and, therefore, it was adopted as an adjustable parameter to fit the simulation to the experimental results. Figures 3.3 (a)-(d) show comparisons between the simulation and experiment for all the samples. One can see a clear discrepancy between the simulation without MCA and the experiment in panel (a) reflecting a bulk-like large MCA in the 11 nm-thick film. The discrepancy is largest around $\theta_H = 0^\circ$ [see Fig. 3.3 (e)], which is consistent with the fact that the hard axis of bulk $CoFe_2O_4$ is along the $\langle 111 \rangle$ direction [96]. The discrepancy significantly decreases with decreasing thickness as shown in panels (b), (c), and (d). This behavior suggests that the MCA of $CoFe_2O_4$ thin film significantly decrease with decreasing thickness. Considering that the thickness dependence of the present experiment should reflect the properties of the magnetically dead layer, this behavior indicates the reduction of MCA of $CoFe_2O_4$ in the magnetically dead layer. We have plotted the difference between the simulations and experiments in Fig. 3.3 (e), and plotted their area from $\theta_H = -80^\circ$ to 40° as a function of thickness d [Fig. 3.3 (f)]. Note that each film has magnetization M and, therefore, we have we divided the areas by M to compensate the different magnetization states.

Let us discuss the origin of the significant reduction of the MCA near the interface. Since the MCA of $CoFe_2O_4$ is well explained by the single-ion model [97], in which the exceptionally high single-ion anisotropy of $Co^{2+}(O_h)$ governs the MCA, the distribution of $Co^{2+}(O_h)$ should have dominant effects on the MCA. The cation distribution of these films has been reported in Ref. [40] and , therefore, we have plotted the inversion parameter y, defined by the chemical formula $[Co_{1-y}Fe_y]_{T_d}[Fe_{2-y}Co_y]_{O_h}O_4$. The y was estimated by the cluster-model analysis of XAS and XMCD spectra. Details will be described in section 4.2. Figure 3.3 (f) shows that y decreases with decreasing thickness, indicating that the fraction of $Co^{2+}(O_h)$ in $CoFe_2O_4$ decreases with thickness. This behavior qualitatively agrees with the reduction of MCA. Here, we should also note that the

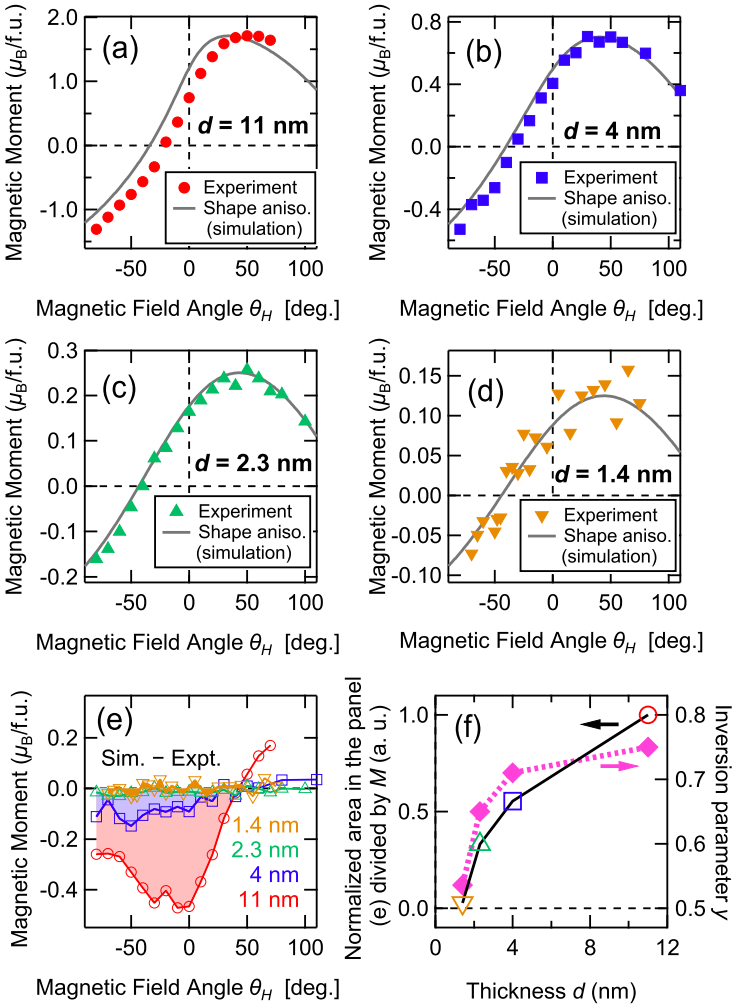

Figure 3.3: Comparison between the experimental and simulated M_{proj} of $CoFe_2O_4$ thin films. (a)-(d) Experimentally obtained M_{proj} and simulations for the films with various thicknesses (d = 11, 4, 2.3, and 1.4 nm). (e) Difference between the experimental and simulated M_{proj} in panels (a)-(d). (f) Comparison between the differences shown in panels (a)-(d) and the previously reported inversion parameter y [40]. In order to compensate the different magnetization states in each film, the differences (shaded area in panel (e)) are divided by M before comparison.

decreasing rate of y is very small above 4 nm, whereas the discrepancy between the experiment and simulation decreases more monotonically. The different behaviors between the inversion parameter y and the MCA suggest that an other origin also contributes to the reduction of MCA. The most plausible origin of the discrepancy is the epitaxial strain. As has been reported repeatedly [98–100], the epitaxial strain largely changes the MCA of $CoFe_2O_4$ significantly. According to previous studies on (111)-oriented $CoFe_2O_4$ thin films [101–104], in-plane compressively and tensilely strained films tend to result in out-of-plane and in-plane easy magnetization, respectively, indicating that out-of-plane easy uniaxial MCA should be induced to compressively strained films. Since our films are slightly compressively strained [40], the MCA would be the sum of original cubic MCA and induced uniaxial MCA. Considering that the surface normal ([111] direction) is the hard and easy axes of the cubic and uniaxial MCA, respectively, the MCA of $CoFe_2O_4$ thin film under a compressive strain would be reduced.

3.4 Conclusion

We have investigated the magnetically dead layers in the epitaxial $CoFe_2O_4(111)$ thin films (thicknesses d =11, 4, 2.3, and 1.4 nm) grown on 2.4 nm-thick γ-$Al_2O_3(111)$ buffer layer/n^+-Si(111) substrates using XAS and XMCD. From the magnetic-field-angle dependence of XMCD spectra, we revealed that the MCA in the magnetically dead layers is significantly reduced. This reduction is qualitatively correlated with the previously reported thickness dependence of cation distribution [40]. Detailed behaviors of the MCA reduction are not fully explained by the cation distribution, suggesting that an other origin contributes to the reduction. We pointed out that out-of-plane easy uniaxial MCA induced by the in-plane compressive epitaxial strain also plays an role in addition to the cation distribution.

Chapter 4

Origin of the magnetically dead layer in spinel ferrites $M\mathrm{Fe_2O_4}$ and its restoration by post-deposition annealing

4.1 Introduction

As introduced in Chapter 1, it is widely accepted that the magnetically dead layers near the interface of spinel ferrites with other materials is originated from antiphase boundaries (APBs) and their antiferromagnetic interdomain exchange interaction [34, 35, 38]. However, recent reports by Wakabayashi *et al.* [40, 41] revealed the correlation between the inversion parameter y (= $[\mathrm{Co}_{1-y}\mathrm{Fe}_y]_{T_d}[\mathrm{Fe}_{2-y}\mathrm{Co}_y]_{O_h}$) and the ferrimagnetic ordered moments in the magnetically dead layer of $\mathrm{CoFe_2O_4}(111)/\mathrm{Al_2O_3}(111)$ and $\mathrm{NiFe_2O_4}(111)/\mathrm{Al_2O_3}(111)$. Figure 4.1 (a) shows the thickness dependence of Fe-ion distribution in $\mathrm{CoFe_2O_4}(111)/\mathrm{Al_2O_3}(111)$. One can see the sudden decrease and increase of $\mathrm{Fe}^{3+}(T_d)$ and $\mathrm{Fe}^{2+}(O_h)$ below the $\mathrm{CoFe_2O_4}$ thickness 4 nm, respectively, which results in a low y. Considering the probing depth of the TEY mode of about several nanometer, the sudden decrease of y below 4 nm may reflect the electronic states near the interface between the $\mathrm{CoFe_2O_4}$ layer and the under lying $\mathrm{Al_2O_3}$ buffer layer. Therefore, the low inversion parameter near the interface is thought

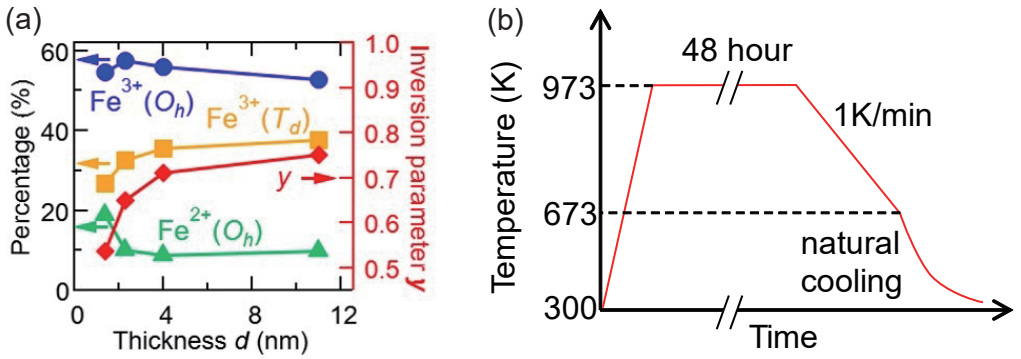

Figure 4.1: (a) Fe-ion distribution near the interface of as-grown $CoFe_2O_4(111)/Al_2O_3(111)/Si(111)$ structure, reconstructed from Ref. [40]. (b) Schematic graph of annealing process.

to be an origin of the magnetically dead layer in addition to the APBs. However, even if a Co ion replace the Fe ion at T_d site, strong antiferromagnetic coupling between O_h and T_d site still exist and the ferrimagnetic order would not be significantly affected. It is not clear how the low inversion parameter degrade the ferrimagnetic order in spinel ferrites.

On the other hand, it has been reported that the cation distribution in $CoFe_2O_4$ is modified by annealing [11,105]. In the present study, we have studied electronic and magnetic states of annealed $CoFe_2O_4$ and $NiFe_2O_4$ thin films.

4.2 Experimental Methods

$CoFe_2O_4$ and $NiFe_2O_4$ thin films with various thicknesses were grown on $Al_2O_3(111)$ buffer layers deposited on Si(111) substrates using pulsed laser deposition (PLD) by Dr. Yuki. K. Wakabayashi and Prof. Ryosho Nakane of the University of Tokyo. The epitaxial $CoFe_2O_4(111)$ thin films (thicknesses of d = 1.4, 2.3, 4, and 11 nm) were grown with a 2.4 nm-thick γ-$Al_2O_3(111)$ buffer layer. The epitaxial $NiFe_2O_4(111)$ thin films (thicknesses of d = 1.7, 3.5, and 5.2 nm) were grown on a 1.4 nm-thick γ-$Al_2O_3(111)$ buffer layer. In order to avoid the charging of samples during the XAS and XMCD measurements, we used highly phosphorus-doped Si(111) substrates with the low resistivity of 2 mΩ cm. For

the epitaxial growth of the γ-Al_2O_3 buffer layers on the Si substrates, we used solid-phase reaction of Al and SiO_2. More detailed description of sample preparation and characterization are provided in Refs. [40, 41]. In order to redistribute cations in the thin films and to recover the inversion parameter, we have annealed the $CoFe_2O_4$ and $NiFe_2O_4$ thin films. In order to reduce the oxidization of Si substrate, we chose 973 K (700 °C) as an annealing temperature because the oxidization rate of Si tends to be high particularly over 1073 K (800 °C). Figure 4.1 (b) shows the temperature variation during the annealing procedure. The films were annealed at 973 K (700 °C) for 48 hours. Since higher inversion parameters of $CoFe_2O_4$ have been reported in slowly cooled bulk crystals rather than in rapidly quenched ones [11], we set a slow cooling rate at 1 K/min down to 673 K (400 °C), then, naturally cooled down to room temperature.

The XMCD measurements were performed at the BL-16A of Photon Factory, High Energy Accelerator Research Organization (KEK-PF).Magnetic field of 5 T was applied parallel to incident x rays. The measurement temperature was room temperature ($\sim$ 300 K). The absorption signals were detected in the total-electron-yield (TEY) mode. Due to the probing depth of several nanometer of the TEY mode [79], we could measure the near interface region of the spinel ferrites in thinner films as explained in the section 3.1. The XMCD signals were collected in "on-the-fly" mode by switching the photon helicity at every energy point.

In order to analyze the XAS and XMCD spectra quantitatively, we employed configuration-interaction (CI) cluster-model calculation. For the localized electrons in these insulating oxides, the CI cluster model is a good approximation. In the present study, we used 'Xtls version 8.5' program developed by Prof. Arata Tanaka of Hiroshima University [84]. In the calculation, we adopted the following empirical relationship or assumptions. The ratio between the on-site Coulomb energy between $3d$ electrons U_{dd} and the attractive $2p$ core hole-$3d$ electron Coulomb energy U_{dc} was fixed to $U_{dc}/U_{dd} \sim 1.3$ [85, 106]. The ratio between Slater-Koster parameters $pd\sigma$ and $pd\pi$ was fixed to $pd\sigma/pd\pi = -2.17$ [82]. The hybridization strength between O $2p$ orbitals T_{pp} was fixed to 0.7 eV for the O_h site and 0 eV for the T_d site [84, 106]. The Slater integrals were set to be 80% of the Hartree-Fock values. Thus, the crystal-field splitting $10Dq$, the charge-transfer energy Δ, U_{dd}, and $pd\sigma$ were treated as adjustable parameters. As for the Fe cations, the parameters were adjusted to reproduce the various experimental

Table 4.1: Parameter values for the CI cluster-model calculations used for the present study in units of eV. Parameters for $Fe^{2+}(O_h)$ were adopted from Ref. [41]

	Δ	$10Dq$	$pd\sigma$	U_{dd}
$Fe^{3+}(O_h)$	3.0	0.8	1.5	7.0
$Fe^{3+}(T_d)$	2.5	-0.5	1.8	6.0
$Fe^{2+}(O_h)$	6.5	0.9	1.4	6.0

Fe $L_{2,3}$-edge spectra by the weighted sum of calculated spectra for the $Fe^{2+}(O_h)$, $Fe^{3+}(T_d)$, and $Fe^{3+}(O_h)$ ions. Here, parameters for $Fe^{2+}(O_h)$ are adopted from the previous report on $NiFe_2O_4$ [41]. The parameter values used in the present study are listed in Table 4.1. As performed in previous work [40, 41] (see Figs. 1.8 (c) and 1.8 (d)), we can decompose experimental XAS and XMCD spectra into three contributions from $Fe^{2+}(O_h)$, $Fe^{3+}(T_d)$, and $Fe^{3+}(O_h)$ ions by fitting the weighted sum of the calculated three spectra. From this analysis, we can obtain the ratio of the numbers of the three ions and the inversion parameter y as defined in Eq. 1.1.

4.3 Results and Discussion

4.3.1 Results on $CoFe_2O_4$ thin films

Figure 4.2 shows the Fe $L_{2,3}$-edge XAS ($\mu^+ + \mu^-$) and XMCD ($\mu^+ - \mu^-$) spectra of the $CoFe_2O_4$ thin films with various thicknesses. Here, μ^+ (μ^-) denote the absorption coefficients for photons whose helicity is parallel (antiparallel) to the majority-spin direction. Figure 4.2 (b) shows that the Fe $L_{2,3}$-edge XMCD intensity of annealed samples are dramatically increased compared to as-grown ones particularly in thinner films (d = 1.4 and 2.3 nm). The XMCD intensities and increasing ratio are shown in Fig. 4.4. The increase of the XMCD spectra clearly demonstrates that the magnetic order of Fe spins at the magnetically dead layer are recovered in the annealed films. The L_3-edge XMCD spectra are composed of characteristic three peaks denoted by **a**, **b**, and **c**. It is established that the three peaks **a**, **b**, and **c** are contributed from the $Fe^{2+}(O_h)$, $Fe^{3+}(T_d)$, and $Fe^{3+}(O_h)$ ions, respectively, in spinel ferrite [30, 107–109]. Therefore, one can discuss the Fe-ion

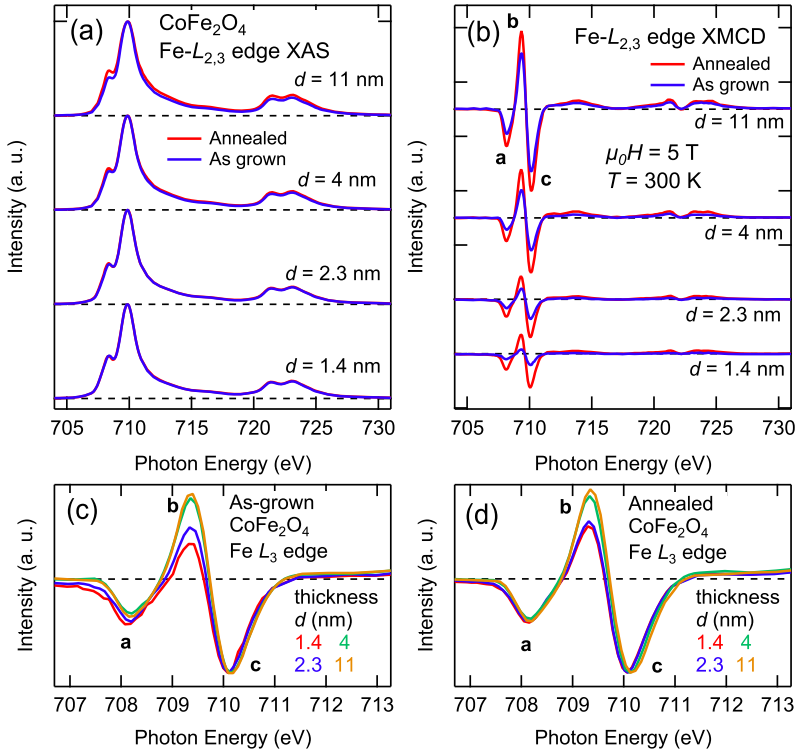

Figure 4.2: Fe L-edge XAS and XMCD spectra of as-grown and annealed $CoFe_2O_4$ thin films with various thicknesses. (a), (b) Fe $L_{2,3}$-edge XAS and XMCD spectra. (c), (d) Magnified views of the Fe L_3-edge XMCD spectra normalized at peak **c**.

distribution in spinel ferrites from the XMCD spectral line shapes. The spin of the $Fe^{3+}(T_d)$ ion antiferromagnetically couple with the other spins at the O_h sites, resulting in the opposite sign of peak **b** relative to those of peaks **a** and **c**. Thus, XMCD spectra are more sensitive to the cation distribution in spinel ferrites than XAS. Therefore, many researchers use XMCD spectra as a probe to discuss the cation distribution in spinel ferrites [30, 107, 108]. Figures 4.2 (c) and (d) show comparison of the Fe L_3-edge XMCD spectral line shapes of as-grown and annealed $CoFe_2O_4$ films. The spectra have been normalized at the height of peak **c**. Peak **b** in Fig. 4.2 (c) decreases with decreasing thickness , the same as the previous report [40], indicating that the reduction of $Fe^{3+}(T_d)$ near the interface. After annealing, as shown in Fig. 4.2 (d), peak **b** is increased particularly in the 1.4 nm-thick film, indicating that the ratio of the $Fe^{3+}(T_d)$ ion is increased by annealing near the interface. This is clear evidence that the Fe ions were redistributed near the interface by the post-deposition annealing.

To clarify the correlation between the redistribution of the cations and the recovery of ferrimagnetic order, quantitative spectral line-shape analysis was necessary. Therefore, we performed CI cluster-model calculation to reproduce the experimental XAS and XMCD spectra by the weighted sum of calculated $Fe^{2+}(O_h)$, $Fe^{3+}(T_d)$, and $Fe^{3+}(O_h)$ spectra using the parameters listed in Table. 4.1. Figure 4.3 shows the experimental and calculated XAS and XMCD spectra at the Fe $L_{2,3}$ edge. All the experimental spectra are well reproduced by the calculated spectra. Here, the weight of each calculated spectrum for the three Fe ions is proportional to the ratio of the numbers of the $Fe^{2+}(O_h)$, $Fe^{3+}(T_d)$, and $Fe^{3+}(O_h)$ ions. Ratios deduced from the fitting are summarized in Fig. 4.4 (a). The inversion parameter y was also deduced and plotted. One can see that y is increased particularly in thinner region. Figure 4.4 (b) shows comparison between the increase of y and the recovery of the XMCD intensity as functions of film thickness. One can see similar thickness dependences between them, which gives clear evidence that the recovery of the magnetically dead layer is achieved by the redistribution of the cations.

Based on the above results and the definition of the inversion of spinel ferrites ($[Co_{1-y}Fe_y]_{Td}[Fe_{2-y}Co_y]_{Oh}$), the recovery of magnetically dead layer by annealing seems to be caused the replacement of irregularly occupying Co ions at the T_d sites near the interface by Fe ions during the annealing process. However, results

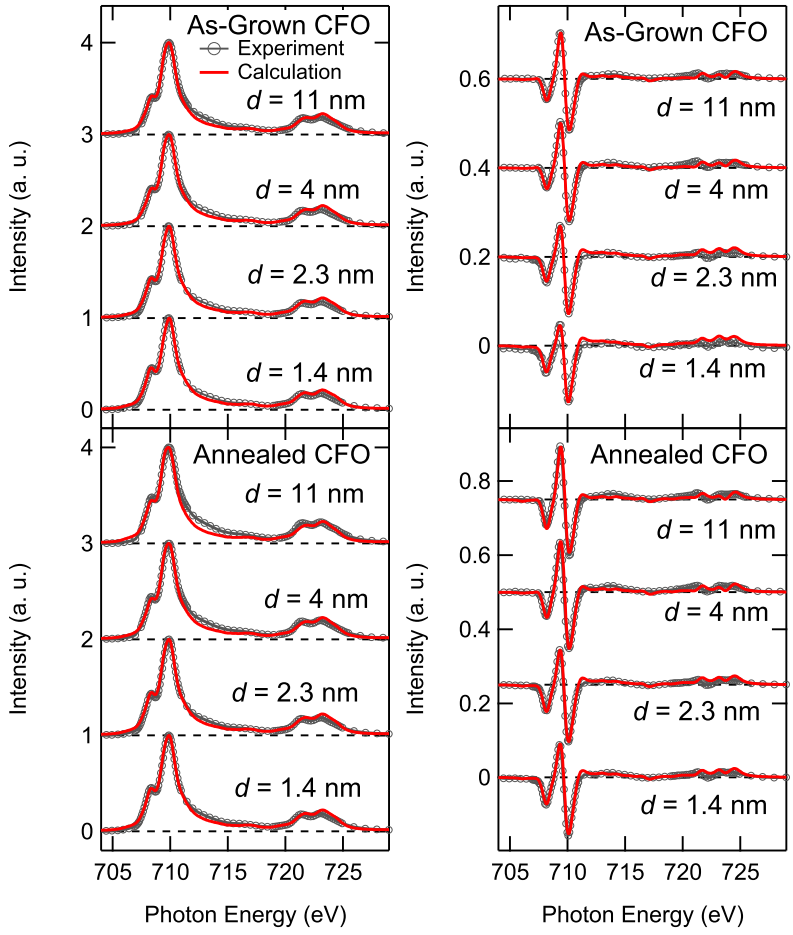

Figure 4.3: Comparison between experimental and calculated XAS and XMCD spectra at the Fe $L_{2,3}$ edge of as-grown and annealed $CoFe_2O_4$ thin films.

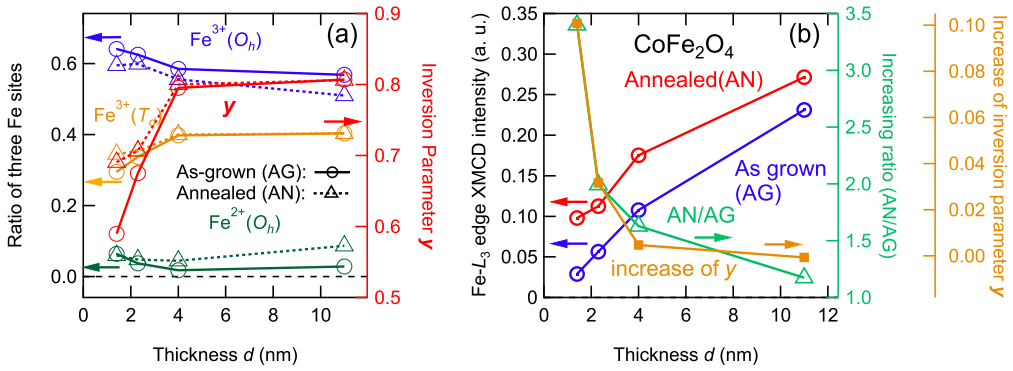

Figure 4.4: Thickness dependences of the Fe-ion distribution and the L_3-edge XMCD intensities for as-grown and annealed $CoFe_2O_4$ thin films. (a) Ratio of the numbers of the $Fe^{2+}(O_h)$, $Fe^{3+}(T_d)$, and $Fe^{3+}(O_h)$ ions as functions of film thickness. The inversion parameter y is also plotted against right axis. Solid lines with open circles and dashed line with open triangles indicate the as-grown and annealed samples, respectively. (b) The Fe L_3-edge XMCD intensity of as-grown and annealed films. Increase of the y and the increasing ratio of XMCD intensities are plotted against the right axes.

at the Co edge does not completely agree with this scenario. Figure 4.5 shows the Co-edge XAS and XMCD spectra for various film thicknesses. In contrast to those at the Fe edge, the XMCD intensities of the annealed films are not so much increased compared to the as-grown ones. Figures 4.5 (c) and (d) show the Co-L_3 edge XMCD spectra normalized at peak **e**. One can see that the positive peak **d** is increased by annealing, particularly in the thinner films. As described in the previous report [40], the positive peak of Co L_3 edge should be originated from $Co^{2+}(T_d)$. Therefore, the increase of peak **d** indicates the increase of the number of $Co^{2+}(T_d)$ ions near the interface after annealing. The increase of positive peak components could also explain the smallness of the increase of the Co-edge XMCD spectra of the annealed sample. Interestingly, not only the $Fe^{3+}(T_d)$ ions but also the $Co^{2+}(T_d)$ ions are increased by annealing. We could not estimate the ratio of the Co ions at the T_d sites relative to those at the O_h sites near the interface because it is difficult to fit the calculation to experiments at the Co edge [40]. However, the above results indicate that there are a number of vacant T_d sites near

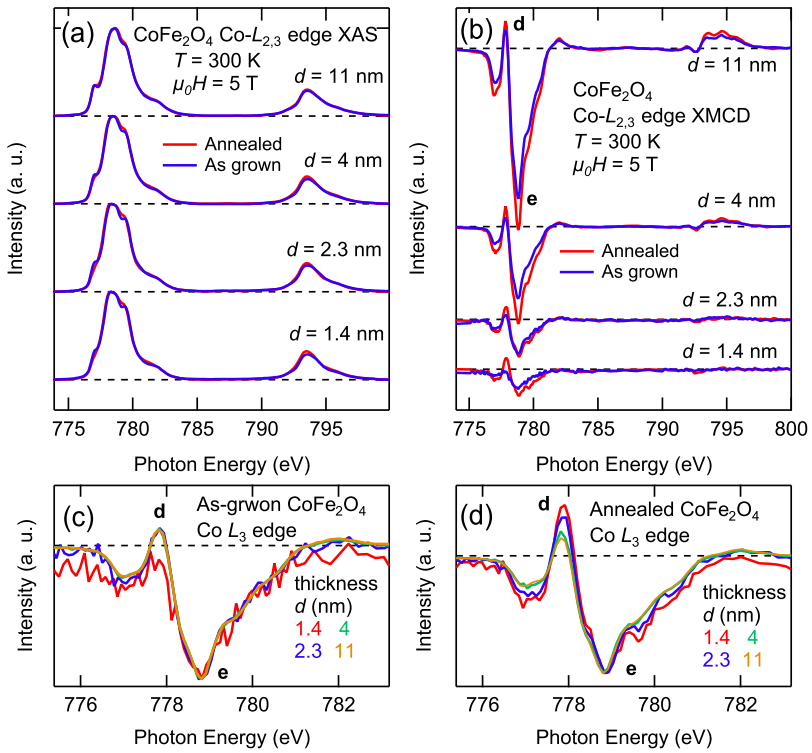

Figure 4.5: Co-edge XAS and XMCD spectra of as-grown and annealed $CoFe_2O_4$ thin films with various thicknesses. (a), (b) Co $L_{2,3}$-edge XAS and XMCD spectra. (c), (d) Magnified views of Co L_3-edge XMCD spectra normalized at peak **e**.

the interface of the as-grown $CoFe_2O_4$ thin films, and the vacancies were filled by Fe and Co ions diffused from O_h sites. These vacant T_d sites would play an important role in the magnetically dead layers (see details in section 4.3.3). On the other hand, to satisfy the charge-neutrality condition of a sample, it also requires existence of oxygen vacancies in the film. We speculate that the oxygen vacancies distribute near the interface and/or crystal domain boundaries and, therefore the vacancies at the T_d site and Fe^{2+} ions at the O_h site would be located near them. The schematic illustrations of the above situations are shown in Fig. 4.6.

Note that the inversion parameter y is defined based on the ideal spinel structure ($[Co_{1-y}Fe_y]_{Td}[Fe_{2-y}Co_y]_{Oh}$) and, therefore, the vacant site is not taken into account. The lowering of y should reflects not only the replacement of the Fe ion by the Co ion, but also vacancies at the T_d and/or O_h sites.

4.3.2 Results on $NiFe_2O_4$ thin films

Figure 4.7 shows Fe $L_{2,3}$-edge XAS and XMCD spectra of as-grown and annealed $NiFe_2O_4$ thin films with various thicknesses d = 1.7, 3.5, and 5.2 nm. The spectra of the as-grown $NiFe_2O_4$ films are adopted from the previous work [41]. Here, in order to compare the spectra taken in different beamlines, we measured XAS and XMCD spectra of the 5.2 nm-thick $NiFe_2O_4$ film under the same condition at the two different beamlines, and corrected energy resolution and the degree of circular polarization. The XMCD intensity of the 1.7 nm-thick film is exceptionally lower than the others, indicating the dominant effect of magnetically dead layers. After annealing, the XMCD intensities were increased. Although the spectra of as-grown films were measured under the ferrimagnetic field of 7 T, the XMCD intensity of annealed films measured under 5 T is larger than those of as-grown ones. This fact clearly indicate that the magnetic order was significantly recovered by annealing also in the $NiFe_2O_4$ thin films similar to $CoFe_2O_4$. Figure 4.8 shows Ni $L_{2,3}$-edge XAS and XMCD spectra of the $NiFe_2O_4$ films. In contrast to $CoFe_2O_4$, not only the Fe edge but also the Ni edge show significant increase of XMCD intensity after annealing (Fig. 4.5). Figures 4.7 (c) and (d) show the magnified view of the Fe L_3-edges XMCD spectra normalized at peak **c**. The spectral line shapes show that the positive peak **b** of the 1.7 nm-thick film is significantly increased after annealing, indicating the increase of $Fe^{3+}(T_d)$ ions. On

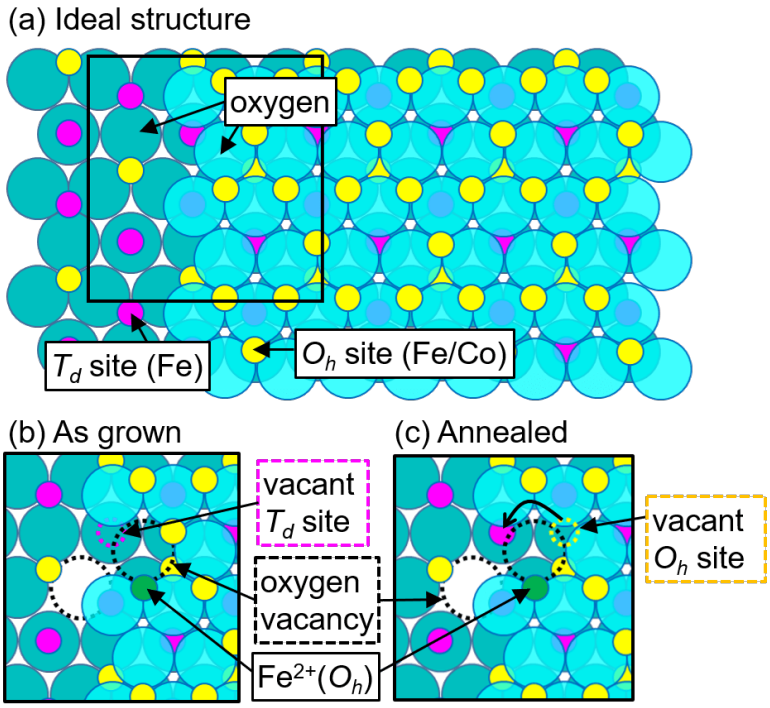

Figure 4.6: Schematic illustrations of the (111) plane of spinel structure. Four layers composed of oxygen (dark blue), T_d and O_h sites (pink and yellow), oxygen (light blue), and O_h sites (yellow) are drawn in bottom-to-top order. The viewpoint of image is perpendicular to the film surface. Some part of upperside two layers are omitted for clarity. (a) Ideal structure. (b) A possible situation around oxygen vacancies in an as-grown film. One T_d site is vacant and one Fe ion at the O_h site become divalent. (c) A possible situation after annealing. A Fe or Co ion at the O_h site is moved to the vacant T_d site.

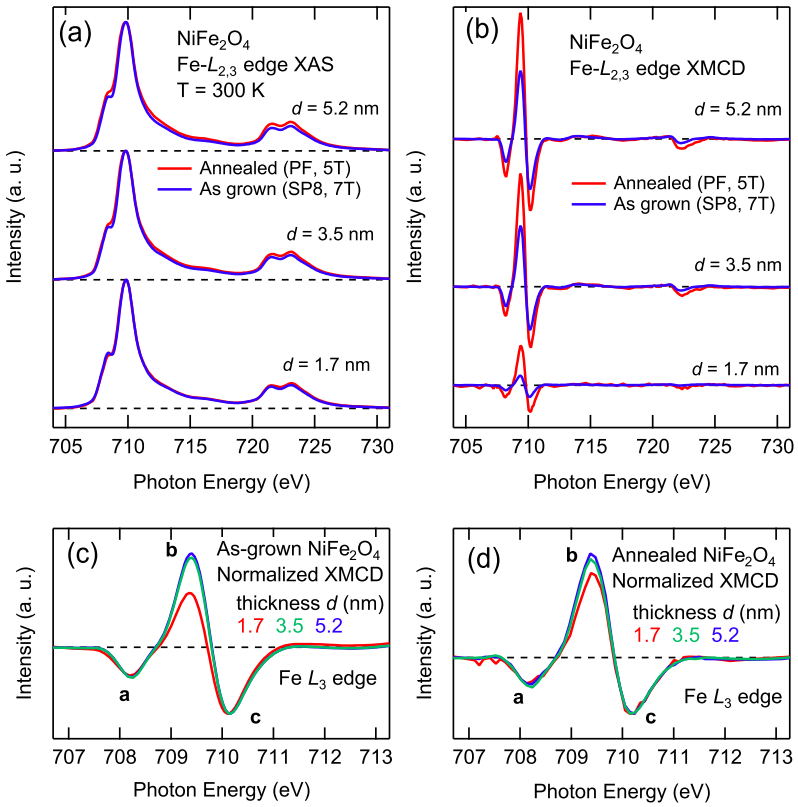

Figure 4.7: Fe L-edge XAS and XMCD spectra of as-grown and annealed $NiFe_2O_4$ thin films with various thicknesses d = 1.7, 3.5, and 5.2 nm. The spectra of as-grown films (blue lines) are adopted from Ref. [41]. (a), (b) Fe $L_{2,3}$-edge XAS and XMCD spectra. (c), (d) Magnified views of Fe L_3-edge XMCD spectra normalized at peak **c**.

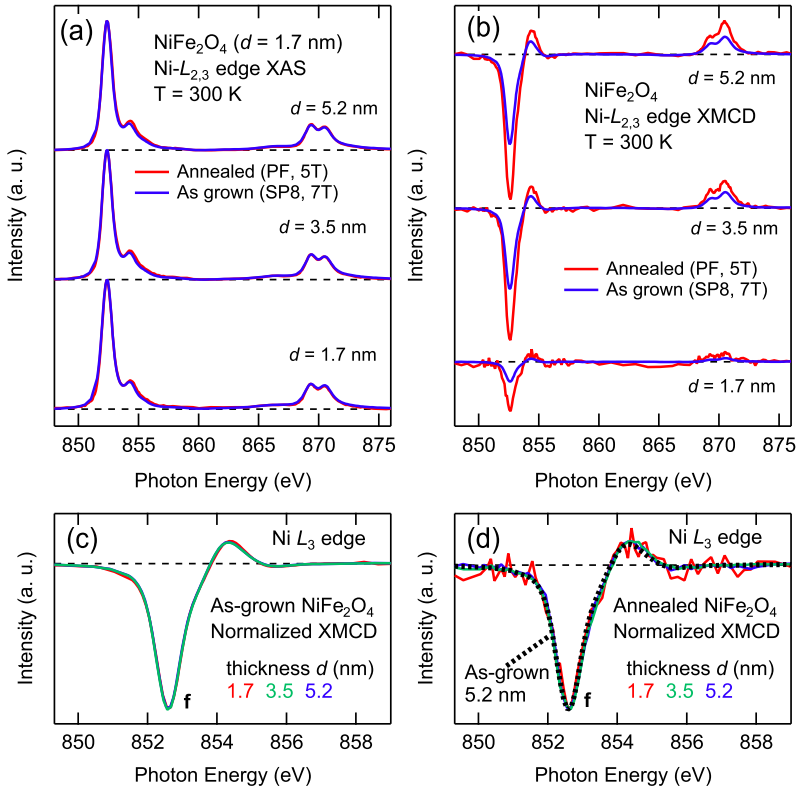

Figure 4.8: Ni L-edge XAS and XMCD spectra of as-grown and annealed $NiFe_2O_4$ thin films with various thicknesses d = 1.7, 3.5, and 5.2 nm. The spectra of as-grown films (blue lines) are adopted from Ref. [41]. (a), (b) Ni $L_{2,3}$-edge XAS and XMCD spectra. (c), (d) Magnified views of Ni L_3-edge XMCD spectra normalized at peak **f**.

the other hand, the Ni-edge XMCD spectral line shapes, shown in Figs. 4.8 (c) and (d), do not show any changes depending on the thickness and annealing. The XMCD spectra of 5.2 nm-thick film are shown in Fig. 4.8 (d) as a dashed line, which demonstrates the same spectral line shape. Since the Ni ion takes only the $Ni^{2+}(O_h)$ state, as reported in as-grown films [41], the same spectral line shapes confirms that the Ni ions did not move to the T_d sites even after annealing due to the high site selectivity of the Ni^{2+} ion. This is also consistent with that the XMCD intensity at the Ni edge showed significant increases unlike at the Co edge in $CoFe_2O_4$, where Co ions moved to T_d site.

As in the case of $CoFe_2O_4$, in order to quantitatively analyze the spectral line shapes, we fitted the weighted sum of three calculated spectra for $Fe^{2+}(O_h)$, $Fe^{3+}(T_d)$, and $Fe^{3+}(O_h)$ ions to the experimental spectra. The parameters for the CI cluster model were the same as those of $CoFe_2O_4$ listed in Table. 4.1. Figure 4.9 shows the experimental and calculated Fe $L_{2,3}$-edge XAS and XMCD spectra. The experimental spectra are well reproduced by the calculation. From the fitting, one can obtain the ratio of the numbers of the $Fe^{2+}(O_h)$, $Fe^{3+}(T_d)$, and $Fe^{3+}(O_h)$ ions in the as-grown and annealed $NiFe_2O_4$ thin films. Figure 4.10 show the thickness dependence of them deduced from the above fitting. One can see that the ratios of the $Fe^{3+}(T_d)$ and $Fe^{3+}(O_h)$ ions are decreased and increased, respectively, at $d = 1.7$ nm. Thus, the inversion parameter y of the as-grown 1.7 nm-thick film is exceptionally lower than those of the thicker films, which is consistent with the tendency of XMCD intensity. The low y of this film is significantly increased to 0.96 after annealing (red dashed line). Therefore, from the view point of the inversion parameter, almost perfect $NiFe_2O_4$ thin films were achieved by annealing. However, there are still the thickness dependence of XMCD intensity even after annealing, namely, the magnetically dead layer still exists even in the nearly $y = 1$ film.

Before annealing the ratio of $Fe^{3+}(T_d)$ to $Fe^{3+}(O_h)$ was about $\frac{2}{3}$, and the Ni ion takes only the divalent state at the O_h sites. Therefore, at least the $\frac{1}{3}$ of T_d site should not be occupied by either Fe or Ni ion in as-grown 1.7 nm-thick thin film. As discussed below, vacancies at the T_d sites rather than those at the O_h sites should have crucial effects on the ferrimagnetic order in the spinel structure.

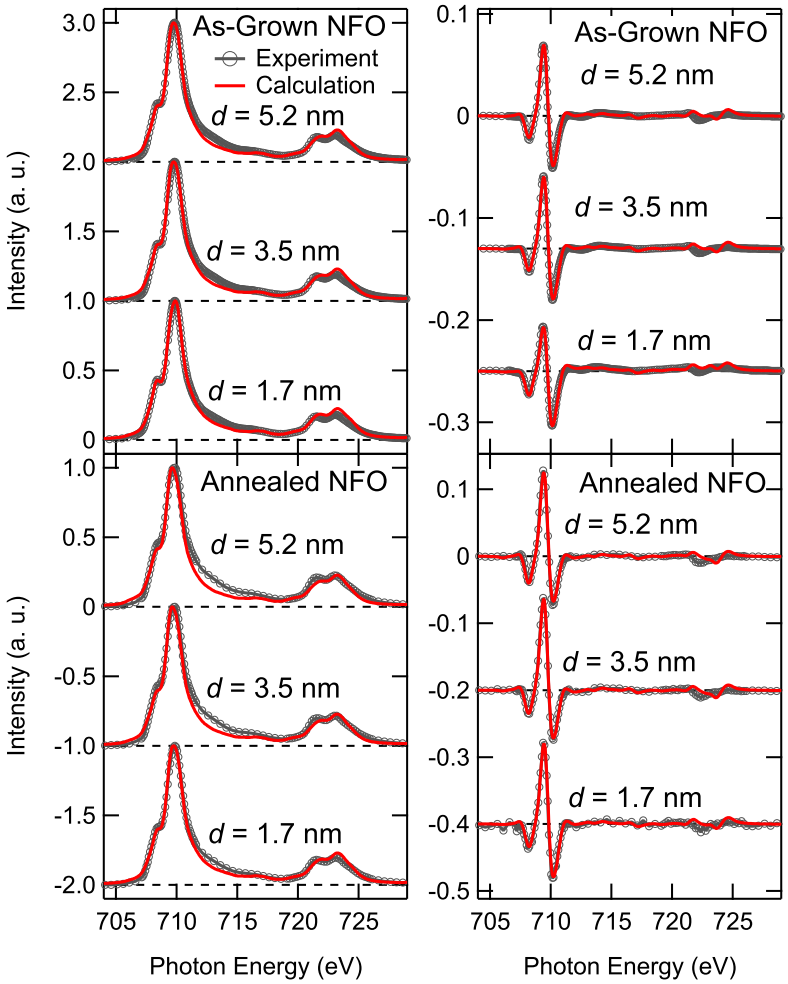

Figure 4.9: Comparison between experimental and calculated Fe $L_{2,3}$-edge XAS and XMCD spectra for as-grown and annealed $CoFe_2O_4$ thin films.

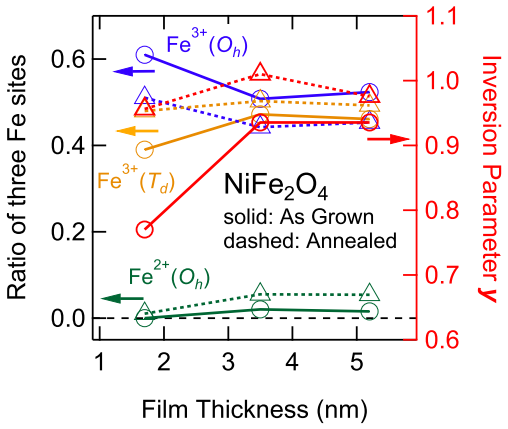

Figure 4.10: Ratio of the numbers of the $Fe^{2+}(O_h)$, $Fe^{3+}(T_d)$, and $Fe^{3+}(O_h)$ ions in the as-grown and annealed $CoFe_2O_4$ thin films as a function of thickness. The inversion parameter y is also plotted against the right axis. Solid lines with open circles and dashed lines with open triangles indicate as-grown and annealed samples, respectively.

4.3.3 Vacant sites as an origin of the magnetically dead layer

Let us discuss the role of vacant sites in the magnetically dead layers. As introduced in section 4.1, it is widely accepted that the magnetically dead layers in the spinel ferrites are driven by the APBs based on the studies on Fe_3O_4 [34, 35, 38]. However, as shown above, we found that there is a significant number of vacant T_d sites near the interface, and transfer of cations from the O_h to T_d sites significantly recover the ferrimagnetic order. It is well known that the antiferromagnetic superexchange interaction between the T_d-site and O_h-site cations is the driving force of ferrimagnetic order in the spinel ferrites. Therefore, the lack of superexchange interaction due to the vacancies should significantly suppress the ferrimagnetism of magnetically dead layers. Although the charge-neutrality condition was discussed in Fig. 4.6, in this section, we focus on how the vacant T_d sites affect spin structures in the magnetically dead layers.

Figure 4.11 (a) focuses the schematic pictures of exchange interaction between the O_h and T_d sites in the usual spinel structure. The experimentally estimated values of the exchange interaction in MFe_2O_4 (M=Co, Ni) [110], which are denoted

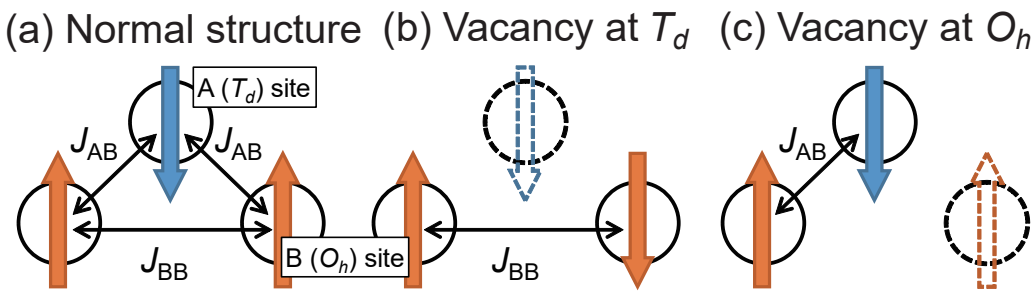

Figure 4.11: Schematic pictures of exchange interaction between the T_d- and O_h-site ions. The T_d and O_h sites are labeled as A and B sites, respectively.

Table 4.2: Exchange interaction between transition metal ions in MFe$_2$O$_4$ (M=Fe, Co) in units of Kelvin (K). Reconstructed from Ref. [110]. The suffixes A and B denotes the T_d and O_h sites, respectively. Note that the listed values include both the superexchange and direct exchange interactions.

		M = Co	M = Ni
J_{AB}	Fe^{3+}-M^{2+}	−22.7	−27.4
	Fe^{3+}-Fe^{3+}	−26	−30.7
J_{BB}	M^{2+}-M^{2+}	46.9	30.0
	Fe^{3+}-M^{2+}	−18.5	−2.7
	Fe^{3+}-Fe^{3+}	−7.5	−5.4

as J_{AB} and J_{BB} in Fig. 4.11, are listed in Table. 4.2 in units of K. Here, the exchange interaction include not only superexchange but also direct exchange interaction. The large negative values of J_{AB} demonstrate that the strong contribution of the T_d site to the ferrimagnetic order. As for the O_h-O_h interaction J_{BB}, one can see large positive values for M^{2+}-M^{2+} interaction, and negative ones for Fe^{3+}-Fe^{3+} and Fe^{3+}-M^{2+} interactions, indicating that the most of J_{BB} area antiferromagnetic interaction. Note that the number of the O_h-T_d exchange pairs are 2.3 times larger than that of O_h-O_h ones [35]. When the T_d site is vacant as shown in Fig. 4.11 (b), J_{AB} between neighboring O_h-site ions would vanish and the remaining interaction is only J_{BB}. Therefore, most of the ions tend to be antiferromagnetically coupled. Clearly, vacancies at the T_d sites strongly degrade the ferrimagnetic order. After annealing, some O_h-site ions move to T_d sites. As a result, vacancies at the T_d sites moves to the O_h sites, which is shown in Fig. 4.11 (c). One can see that there is only antiferromagnetic J_{AB} which still stabilizes the ferrimagnetic order. It can be concluded that vacancies at the O_h sites still prefer ferrimagnetic order, whereas vacancies at the T_d sites strongly degrade the ferrimagnetic order.

4.4 Conclusion

We have studied the electronic and magnetic states of as-grown and annealed $CoFe_2O_4$(111) and $NiFe_2O_4$(111) thin films with various thicknesses grown on Si substrate using γ-Al_2O_3 buffer layers. The film thicknesses were 1.4, 2.3, 4, and 11 nm for $CoFe_2O_4$, and 1.7, 3.5, and 5.2 nm for $NiFe_2O_4$. By analyzing the spectral line shapes using the configuration-interaction cluster-model calculation, we estimated the valences and site occupancies of Fe ions. We confirmed that there were magnetically dead layers through a significant reduction of XMCD intensities in very thin films (1.4 and 2.3 nm for $CoFe_2O_4$, and 1.7 nm for $NiFe_2O_4$). As reported in the previous work [40, 41], sudden reduction of inversion parameters were observed in magnetically dead layers. In order to redistribute the ions, we annealed the films for 48 hours in air. As a result, we successfully recovered the ferrimagnetic order in the magnetically dead layers; the XMCD intensity and inversion parameters were significantly increased after annealing, particularly in thinner films. Furthermore, from comparison between the results of the as-grown and annealed films, we found that there were a number of vacant T_d sites in the

magnetically dead layers. After annealing, the vacancies at the T_d sites were partially occupied by ions moved from the O_h sites. The microscopic origin of the magnetically dead layers arisen from the vacant T_d sites.

Chapter 5

XMCD study of the Verwey transition in Fe_3O_4

5.1 Introduction

As described in section 1.5, the orbital order in Fe_3O_4 has been a hot topic for a long time. In order to examine the orbital states, x-ray absorption spectroscopy (XAS) and x-ray magnetic circular dichroism (XMCD) are useful. By measuring XAS spectra and XMCD spectra, one can obtain the orbital magnetic moment through the well-known sum-rule analysis [69, 70]. The orbital magnetic moment should reflect the orbital states realized in the ordered state mentioned above. Although many XMCD studies were performed previously [78, 111–115], the reported orbital magnetic moments did not agree with each other, and neither temperature nor angle dependence related to the Verwey transition was detected. In order to tackle these issues, we have added three new features to XMCD experiment as follows. First, we measured a partially detwinned thin film. Since the Verwey transition is accompanied by a structural transition from the cubic to monoclinic phases upon cooling, twinning which occurs in the low-temperature phase is a severe problem. In a bulk crystal, there are 24 orientations of crystal domains [116], but the number of different orientations is significantly reduced to 2 in a thin film grown on a stepped substrate [63]. Therefore, anisotropy which might be hidden by the twinning may be detected in thin films grown on stepped substrates. Second, we measured XMCD spectra using the fast circular-

polarization switching technique [88, 94], which allows us to detect XMCD signals with much higher accuracy than the conventional method of subtracting XAS spectra taken with opposite circular polarization. Compared to the conventional XMCD experiments, one can minimize extrinsic effects arising from the time variation of XAS spectra. Third, we used the vector-magnet XMCD apparatus, which allows us to measure the anisotropy of spectra with a fixed incident angle of x rays by applying magnetic fields along variable directions [90]. As reported in previous studies [81, 111], extrinsic saturation effect of TEY mode, which is known as a distortion of spectra depending on incident angles, is not negligible. Therefore, using this apparatus, one can discuss the anisotropy of spectra with a very high accuracy. Based on the above new features, we have attempted to detect the orbital order in Fe_3O_4.

5.2 Experimental Methods

A 40-nm-thick Fe_3O_4 thin film was grown on an off-cut MgO substrate using molecular beam epitaxy (MBE) by Dr. Chun-Fu Chang and Prof. Liu Hao Tjeng of the Max Planck Institute for Chemical Physics of Solids. Figure 5.1 (a) shows a schematic illustration of the sample structure. The [001] axis of the off-cut substrate is tilted by 6° towards the [100] axis, thus, there are step edges along the [010] axis on its surface. Figure 5.1 (b) shows the resistivity of the Fe_3O_4 thin film as a function of temperature. The Verwey transition temperature T_V of this film was about 117 K. The bulk-like higher T_V and the clear hysteresis demonstrate the high quality of this film in contrast to the low T_V and broad transition in previously reported thin films [117–119].

The XMCD measurements were performed using the vector-magnet XMCD apparatus installed at the undulator beamline BL-16A of Photon Factory, the High Energy Accelerator Research Organization (KEK-PF). Absorption signals were detected in the total electron yield (TEY) mode. The XMCD signals were collected by switching the photon helicity at each photon energy with the frequency of 10 Hz for 1 second under the fixed magnetic field of 1 T [94]. In order to see the effect of short-range orbital order which is predicted just above T_V, we chose 100, 133, and 208 K as measurement temperatures corresponding to slightly below, above, and far above T_V, respectively. In order to minimize experimental artifacts,

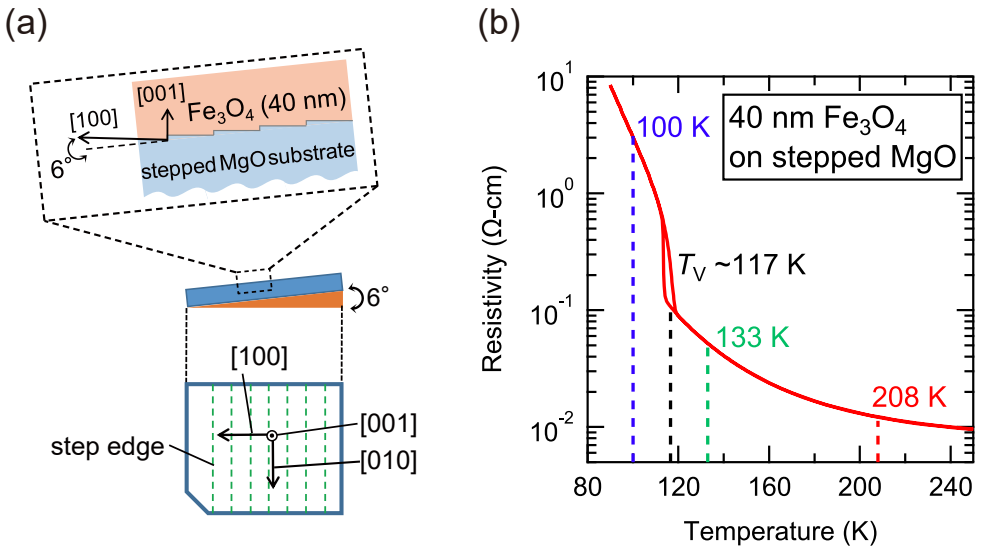

Figure 5.1: Sample structure and resistivity of the 40-nm-thick Fe_3O_4 thin film grown on an off-cut MgO substrate. (a) Schematic illustration of the sample structure. (b) Resistivity of the Fe_3O_4 thin film. The measurement temperatures of the present study are indicated by blue, green, and red dashed lines.

we averaged the repeatedly measured spectra under opposite magnetic-field directions and reversed photon helicities. The geometry of the present measurements is illustrated in Fig. 5.2. The magnetic field was applied along characteristic three crystal axes [001], [111], and [110]. In order to discuss the small angle dependence of the orbital magnetic moment, the extrinsic saturation effect of the TEY mode is not negligible [81,111]. In order to eliminate the saturation effect from the angle dependence, we fixed the x-ray incident angle and varied the magnetic-field directions. The magnetic-field angle θ_H was defined as an angle measured from the optical axis of incident x rays. Since the TEY signals were very weak for the in-plane magnetic-filed direction, we slightly (10°) tilted the magnetic-field direction of the [110] measurements out of plane, similar to a previous x-ray magnetic linear dichroism study [120].

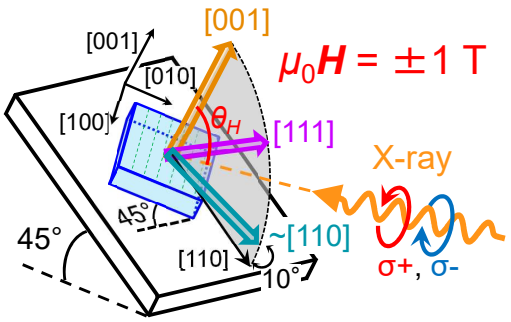

Figure 5.2: Schematic illustration of the experimental geometry. θ_H denotes an angle between the magnetic field and the x-ray incident direction.

5.3 Results and Discussion

Figures 5.3 (a) and (b) show the Fe $L_{2,3}$-edge XAS ($\mu^+ + \mu^-$) and XMCD ($\mu^+ - \mu^-$) spectra of the Fe_3O_4 thin film, respectively. Here, μ^+ (μ^-) denotes the absorption coefficients for photon with helicity parallel (antiparallel) to the majority-spin direction. The XMCD spectra have been divided by $\cos\theta_H$ for comparison because the XMCD intensity is proportional to the projection of the magnetization onto the x-ray incident direction. The extremely low noise level demonstrates the precision of our measurements. Figures 5.3 (c)-(f) show magnified views of the L_3- and L_2-edge XAS and XMCD spectra. One can see clear changes of the spectral line shapes depending on the magnetic field direction and temperature. Although angle-dependent XMCD studies on Fe_3O_4 were previously reported [111, 113], it was not possible to distinguish the intrinsic anisotropy from the extrinsic saturation effect. In the present study, we can rule out the possibility of saturation effects and, therefore, the observed anisotropy of the spectra is entirely intrinsic. The XAS spectra shown in Figs. 5.3 (c) and (e) exhibit a small anisotropy of the spectral line shape. This anisotropy can be explained by x-ray magnetic linear dichroism (XMLD). First, let us discuss the difference between the XAS spectra taken under the magnetic fields in the [110] and [001] directions. Figure 5.4 (a) illustrates the experimental geometry and the polarization of incident x rays. Since the circularly polarized light is a sum of two orthogonal linearly polarized light, the non-polarized XAS spectrum $\mathrm{XAS}^{\text{non-pol.}} = \mathrm{XAS}^{\sigma^+} + \mathrm{XAS}^{\sigma^-}$ can also be written as $\mathrm{XAS}^{\sigma^x} + \mathrm{XAS}^{\sigma^y}$. Here, σ^+, σ^-, σ^x, and σ^y denote circularly and linearly

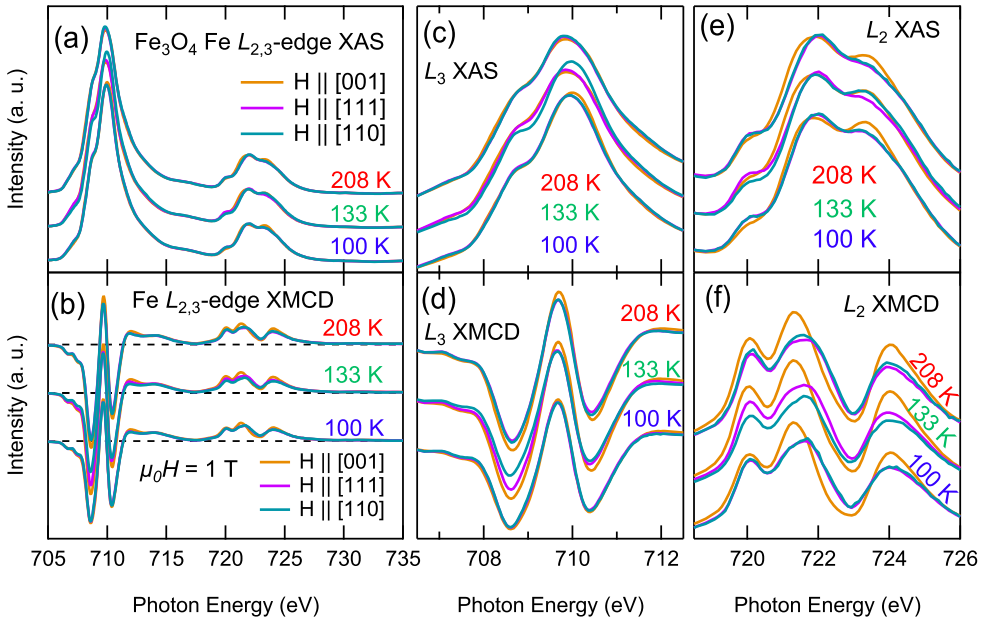

Figure 5.3: Fe $L_{2,3}$-edge XAS (a) and XMCD (b) spectra of the Fe_3O_4 thin film for various temperatures and magnetic field directions. The XMCD spectra have been divided by $\cos\theta_H$ for comparison. (c)-(f) Magnified views of the L_3- and L_2-edge XAS and XMCD spectra.

polarized photons as defined in Fig. 5.4 (a). Therefore, the difference between XAS spectra under the magnetic fields along the [110] and [001] directions are given by

$$\mathrm{XAS}_{[110]} - \mathrm{XAS}_{[001]} = (\mathrm{XAS}^{\sigma^x}_{[110]} - \mathrm{XAS}^{\sigma^x}_{[001]}) + (\mathrm{XAS}^{\sigma^y}_{[110]} - \mathrm{XAS}^{\sigma^y}_{[001]}). \quad (5.1)$$

The first and second term on the right side is the XMLD spectra for the σ^x and σ^y polarization, respectively. Because the electric field of σ^y is perpendicular to both the magnetic field directions [001] and [110], XMLD for σ^y should be small in this geometry. Therefore, the difference of XAS spectrum $\mathrm{XAS}_{[110]} - \mathrm{XAS}_{[001]}$ should largely reflect XMLD for σ^x. Figure 5.4 (b) shows the difference spectrum $\mathrm{XAS}_{[110]} - \mathrm{XAS}_{[001]}$ compared with the previously reported XMLD spectrum of the in-plane uniaxially strained Fe_3O_4 thin film grown on a STO(110) substrate [120]. One can see good agreement between them. The XMCD spectra also

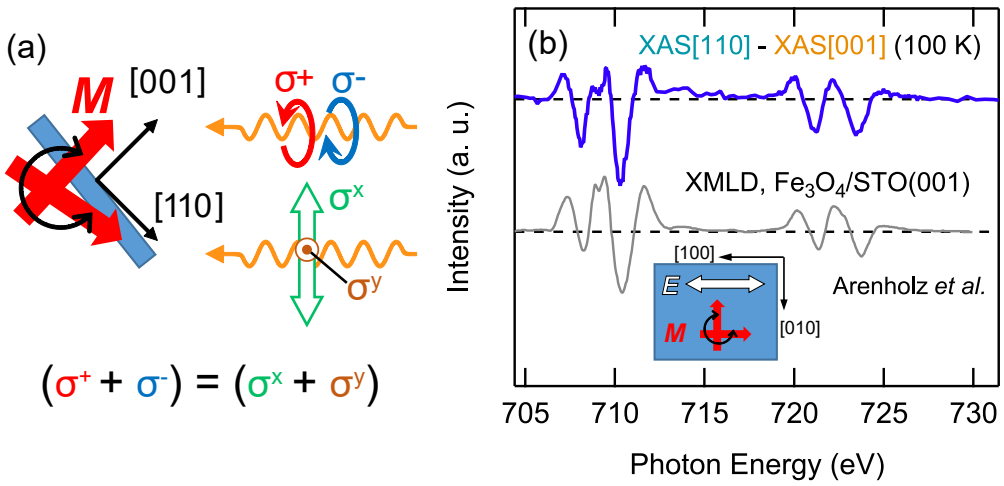

Figure 5.4: Interpretation of the observed anisotropy in the XAS spectra. (a) Illustration of the experimental geometry and the polarization of incident x rays. (b) The difference spectrum of $XAS_{[110]}$ and $XAS_{[001]}$ compared with the previously reported XMLD spectra [120]. The experimental geometry of the XMLD spectra is shown as the inset.

show anisotropy in the spectral line shapes particularly at the L_2 edge [see Fig. 5.3 (f)]. The spectra under the magnetic field along [001] show clearly different spectral line shapes from the spectra taken under different magnetic field directions. Considering that the present Fe_3O_4 thin film is epitaxially grown on the MgO substrate, the film is compressively strained (lattice mismatch being $\sim 0.3\%$). As reported in the previous angle-dependent XMCD study of a spinel manganite [121], even a small uniaxial strain induces a uniaxial anisotropy to the XMCD spectra, which would also be the origin of the anisotropy observed in our XMCD spectra.

It is widely recognized that the characteristic three negative, positive, and negative peaks at the L_3-edge XMCD spectra of Fe_3O_4 primarily originate from the $Fe^{2+}(O_h)$, $Fe^{3+}(T_d)$, and $Fe^{3+}(O_h)$ ions, respectively. To confirm this, we have calculated XAS and XMCD spectra of the Fe ions with the different valences at the different crystallographic sites based on the CI cluster model using the same parameters as those listed in chapter 4 as shown in Figs. 5.5 (a) and (b). One can

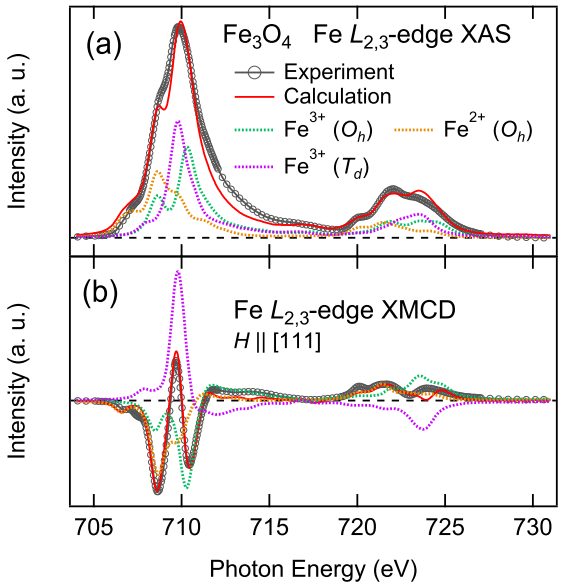

Figure 5.5: Comparison between the experimental and calculated Fe $L_{2,3}$-edge XAS (a) and XMCD (b) spectra of Fe_3O_4.

see that the three peaks at the L_3-edge XMCD spectra are well reproduced by the CI cluster-model calculation.

By applying the XMCD sum rule to the spectra [69, 70], one can deduce the spin and orbital magnetic moments according to the following equations,

$$m_{\mathrm{orb}}^{\mathrm{proj}} = -\frac{4\int_{L_3+L_2}(\mu^+ - \mu^-)\,d\nu}{3\int_{L_3+L_2}(\mu^+ + \mu^-)\,d\nu} n_h \mu_{\mathrm{B}}, \tag{5.2}$$

$$m_{\mathrm{spin}}^{\mathrm{proj}} = -\frac{2\int_{L_3}(\mu^+ - \mu^-)\,d\nu - 4\int_{L_2}(\mu^+ - \mu^-)\,d\nu}{\int_{L_3+L_2}(\mu^+ + \mu^-)\,d\nu} n_h \mu_{\mathrm{B}}. \tag{5.3}$$

Here, $m_{\mathrm{orb}}^{\mathrm{proj}}$ and $m_{\mathrm{spin}}^{\mathrm{proj}}$ denotes the orbital and spin magnetic moments, respectively, projected onto the x-ray incident direction, in units of μ_{B}. The n_h denotes the number of Fe $3d$ holes, and we adopted $n_h = 13.5/3$ from Ref. [112]. We have ignored the magnetic dipole term $7m_{\mathrm{T}}$ in the spin sum rule (5.3) because it is negligibly small under O_h and T_d symmetry [71]. Figures 5.6 (a) and (b) show

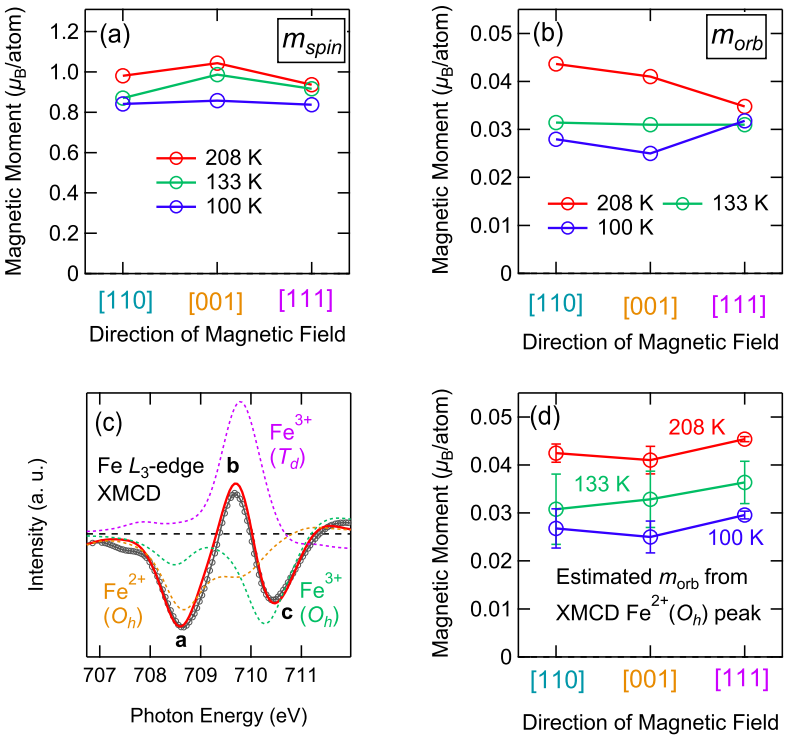

Figure 5.6: Magnetic moments deduced from the XMCD spectra using the XMCD sum rules and the relative intensity of peak **a** to peak **c**. (a), (b) Spin and orbital magnetic moments deduced using the XMCD sum rule. (c) Magnified view of Fig. 5.5 (b), demonstrating the origins of the three peaks at the L_3-edge XMCD spectra. (d) Orbital magnetic moments estimated from the relative intensity of peak **a** to peak **c**. Errors are estimated from experimental reproducibility.

the deduced spin and orbital magnetic moments, respectively. Here, the deduced values have been divided by $\cos\theta_H$ for comparison. One can see a reduction of the spin magnetic moments with decreasing temperature in all the directions. This tendency is consistent with previous studies which reported the reduction of magnetization below T_V [122, 123].

Since the applications of XMCD orbital sum rule requires the integration of XMCD spectra over the $L_{2,3}$ edge (see Eq. 5.2), any slight offset in spectra critically affects the precise determination of the magnetic moment. Therefore, evaluation of the error bars in the experimental moment is difficult especially when the experimental reproducibility is concerned. The large discrepancy between the reported orbital magnetic moments deduced from XMCD demonstrates that careful background subtraction is necessary [78, 111–115]. In addition, as stated in chapter 3, the magnetization direction may deviates from the applied magnetic field direction, resulting in a disagreement between the true m_{orb} and the deduced $m_{\mathrm{orb}}^{\mathrm{proj}}/\cos\theta_H$ which is plotted above. In order to discuss very small orbital magnetic moments and their variation with magnetic field direction and temperature with high reliability, let us estimate them in a different way. Figure 5.6 (c) shows the magnified view of Fig. 5.5 (b) at the L_3 edge. The calculated spectra clearly indicate that peaks **a**, **b**, and **c** in the L_3-edge XMCD spectra mainly originate from $Fe^{2+}(O_h)$, $Fe^{3+}(T_d)$, and $Fe^{3+}(O_h)$ ions, respectively. Since the Fe^{3+} (d^5) ions, which have the stable half-filled d shell, have no orbital degree of freedom, their orbital magnetic moment should be negligibly small. Therefore, the XMCD intensities from the $Fe^{3+}(O_h)$ and $Fe^{3+}(T_d)$ ions dominantly originate from the spin magnetic moments. As for peak **a**, since there is the orbital degree of freedom at the $Fe^{2+}(O_h)$ (d^6) ion, both spin and orbital magnetic moments contribute to the XMCD intensity. Considering that the spin of $Fe^{2+}(O_h)$ ion should be parallel to that of $Fe^{3+}(O_h)$ ion in the ferrimagnetic state ($T <\sim 860K$), the contribution from the spin magnetic moment to peak **a** should be proportional to peak **c**. Note that there is certain spectral weight from the $Fe^{2+}(O_h)$ ion at peak **b**. Therefore, the relative intensity of peak **a** to peak **c** and the orbital magnetic moment from $Fe^{2+}(O_h)$ ion should have a positive correlation. Figure 5.6 (d) shows the orbital magnetic moments estimated from the relative intensity of peak **a** to peak **c**. The error bars were evaluated from the reproducibility of multiple measurements. Since this determination does not require the wide-range integration over the spectrum, it is

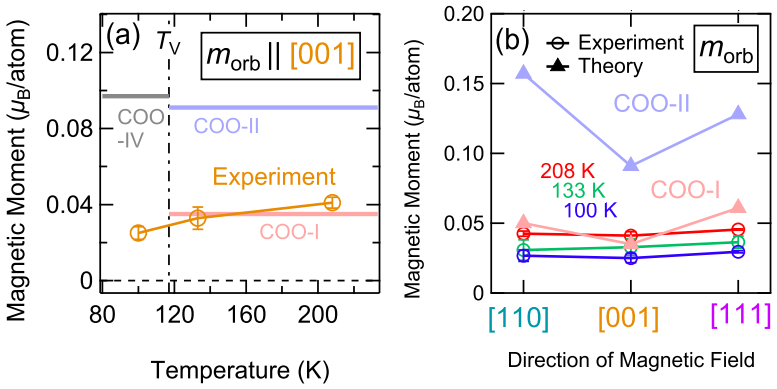

Figure 5.7: Comparison between the COO models and experimental results. (a) Temperature dependence of the orbital magnetic moment along the [001] direction. (b) Angle dependence of the orbital magnetic moment at the three temperatures 100, 133, and 208 K.

not sensitive to small experimental artifacts like the offset of the spectra. The error bars are less than 0.01 μ_B, which demonstrate the high accuracy of this analysis compared with those reported previously, e.g. 0.25 ± 0.03 [112] and 0.00 ± 0.02 μ_B/atom [114]. Here, the vertical axis was set according to the results of orbital sum rule to be the same value at the 208 and 100 K in [001] direction. Therefore, the absolute values might be different from these estimate might be changed, however, one can discuss the temperature and angle dependences. One can confirm the reduction of the orbital magnetic moment with decreasing temperature. From the consistency between the two analyses, we claim with confidence that there is a decreasing tendency of the orbital magnetic moment upon cooling across T_V. We also found that there was almost no anisotropy in the orbital magnetic moment below and above T_V. It should be noted that the uniaxial anisotropy of the XMCD spectra induced by the epitaxial strain may affect the angle dependence, however, the temperature dependence would represent that of bulk Fe_3O_4 to a large extent.

In order to discuss the orbital order just above T_V, we have compared our results with the orbital magnetic moments predicted by the Hartree-Fock calculation which takes into account complex-number orbital order [61, 62]. As described in section 1.5, two kinds of COO models, COO-I and COO-II, were predicted (see Fig. 1.13). Note that the orbital order below T_V was labeled COO-IV. Figure 5.7

(a) and (b) show the predicted (averaged) orbital magnetic moments compared with the present experimental results. Here, we have assumed that the predicted short-range orbital orders COO-I and COO-II are fully aligned by applied external magnetic field. The observed orbital magnetic moments are close to those of the COO-I state. One may, therefore, think that the ordered state just above T_V is close to the COO-I. However, because the calculated orbital magnetic moments strongly depends on model parameters, namely, the predicted values from theory may vary with the model parameters. From the viewpoint of the temperature dependence along the [001] direction, the absence of large difference between below and above T_V is similar to the COO-II case whose value is nearly the same as that of the Verwey state (COO-IV). However, the relatively large anisotropy of the COO-II state does not appear in the present experimental results [see Fig. 5.7]. At present, the experimental results are not fully explained by theory. However, our findings of (i) the decreasing trend of orbital magnetic moment across T_V upon cooling and (ii) the almost no anisotropy of orbital magnetic moment below and above T_V would provide constraints on theoretical models that describe the Verwey transition [54–56, 60–62]. These features are seemingly consistent with orbital order composed of real orbitals.

5.4 Conclusion

We have performed XMCD experiments on the partially detwinned Fe_3O_4 thin film using the vector-magnet apparatus and the fast polarization-switching undulator beamline. The measurements were performed at 100, 133, and 208 K under the magnetic field of 1 T applied along the [001], [111], and [110] directions. We observed clear magnetic-field-angle dependences in the XAS and XMCD spectra. We explained the anisotropy of the XAS spectra as arising from XMLD, and that of XMCD from the uniaxial anisotropy induced by the epitaxial strain. From sum-rule analyses, we obtained small orbital magnetic moments less than 0.05 μ_B/atom for every measurement condition. In order to avoid the effects from possible slight offsets in the measured spectra, we examined the correlation between the spectral line shapes and the orbital magnetic moments originating from the $Fe^{2+}(O_h)$ ions. We found that the orbital magnetic moment decreases across T_V upon cooling in all the three directions. We also found that there was almost no anisotropy of the

orbital magnetic moment at all the three temperatures within experimental error below 0.01 μ_B/atom. We compared the present results with the reported value in complex-number orbital order models [61, 62], but not agreed well. The observed temperature dependence and the upper bound of the angle dependence of the orbital magnetic moments would put constraints on theoretical models for the studies of the Verwey transition.

Chapter 6

Summary

As introduced in Chapter 1, the magnetic and electronic properties of spinel ferrites $M\mathrm{Fe_2O_4}$ (M = Fe, Co, Ni) have attracted strong attention from both the scientific and technological point of view. Towards the industrial applications, the spin-filter structure using spinel ferrites are intensively studied as a promising spin injector to Si. However, the magnetically dead layer has prevented practical applications. In previous studies, it was revealed that the significant lowering of inversion parameter y at the interface is correlated with the magnetically dead layers [40, 41]. In order to clarify the microscopic origin, we investigated magnetic and electronic states of epitaxial $\mathrm{CoFe_2O_4}$(111) and $\mathrm{NiFe_2O_4}$(111) thin films using x-ray absorption spectroscopy (XAS) and x-ray magnetic circular dichroism (XMCD). The film thicknesses were 1.4, 2.3, 4, and 11 nm for $\mathrm{CoFe_2O_4}$, and 1.7, 3.5, and 5.2 nm for $\mathrm{NiFe_2O_4}$.

In Chapter 3, the magnetocrystalline anisotropy (MCA), which is intrinsic to the property of material, at the magnetically dead layers of the epitaxial $\mathrm{CoFe_2O_4}$(111) thin films are examined. From the magnetic-field-angle dependence of XMCD spectra, we revealed that the MCA is significantly reduced in the magnetically dead layers. This reduction was qualitatively explained by the cation distributions near the interface.We also pointed out that the uniaxial MCA induced by epitaxial strain play a certain role in addition to the cation distribution.

In Chapter 4, we presented XMCD study of the as-grown and annealed $\mathrm{CoFe_2O_4}$(111) and $\mathrm{NiFe_2O_4}$(111) thin films. By analyzing the spectral line shapes using the configuration-interaction cluster-model calculation, the valences and site

occupancies of Fe ions were obtained. We confirmed that there were magnetically dead layers through a significant reduction of XMCD intensities in very thin films (1.4 and 2.3 nm for $CoFe_2O_4$, and 1.7 nm for $NiFe_2O_4$). In order to redistribute the cations, we annealed the films for 48 hours in air. As a result, the ferrimagnetic order in the magnetically dead layers was successfully recovered; the XMCD intensity and inversion parameters were significantly increased after annealing, particularly in thinner films. Furthermore, it was found that there were a number of vacancies at the T_d sites in the magnetically dead layers. After annealing, the vacancies at the T_d sites were partially occupied by ions moved from the O_h sites. From the above, we concluded that the microscopic origin of the magnetically dead layers induced by cation distributions arise from the vacant T_d sites.

From the viewpoint of fundamental science, the Verwey transition in Fe_3O_4 was investigated in Chapter 5. We performed XMCD experiments on the partially detwinned Fe_3O_4 thin film using the vector-magnet apparatus and the fast polarization-switching undulator beamline. The accurate XMCD measurements were conducted under the magnetic field of 1 T applied along the [001], [111], and [110] directions. The measurement temperatures of 100, 133, and 208 K were chosen as slightly below, above, and far above the transition temperature T_V, respectively. From sum-rule analyses, we obtained small orbital magnetic moments less than 0.05 μ_B/atom for every measurement condition. In order to avoid the effects from possible slight offsets in the measured spectra, we examined the correlation between the spectral line shapes and the orbital magnetic moments originating from the $Fe^{2+}(O_h)$ ions. It was found that the orbital magnetic moment decreases across T_V with decreasing temperature in all the three directions. We also found that there was almost no anisotropy of the orbital magnetic moment at all the three temperatures within experimental error below 0.01 μ_B/atom. We compared the present results with the reported value in complex-number orbital order models [61,62], but not agreed well. The observed temperature dependence and the upper bound of the angle dependence of the orbital magnetic moments would put constraints on theoretical models for the studies of the Verwey transition.

To summarize, we presented new insights into the electronic and magnetic states in spinel ferrites from both the scientific and technological point of view. As for the spin-filter structures, it was found that the vacant T_d sites near the

interface is the microscopic origin of the magnetically dead layers in addition to the antiphase boundaries. Also, we found that the vacancies at the T_d sites can be restored by the post-deposition annealing. These results provide a new important perspective for the design of spin-filter structures using spinel ferrites. As for the Verwey transition in Fe_3O_4, we observed temperature and angle dependences of orbital magnetic moments. This information can be directly compared with expected orbital-order models and, therefore, it is interesting to measure the other orbital active systems such like FeV_2O_4, where the interplay of 2 kinds of orbital active ions $V^{3+}(O_h)$ (t_{2g}^2) and $Fe^{2+}(T_d)$ $(e_{\downarrow}^1)$ thought to result in complicated orbital-ordered state [124, 125].

Acknowledgments

It is my greatest pleasure to express gratitude to the following people concerning this my doctoral study.

First of all, I would like to express my sincere gratitude to Prof. Atsushi Fujimori, who has given me the opportunity to study these interesting materials and a lot of invaluable advice. This work could not have been completed without his huge help.

I also express heartfelt gratitude to Dr. Goro Shibata, who has always given me great guidance for experiment and analysis.

The high-quality $CoFe_2O_4$ and $NiFe_2O_4$ thin films are provided by Prof. Masaaki Tanaka's group from the Department of Electrical Engineering and Information System the University of Tokyo. I am very grateful to Dr. Yuki. K. Wakabayashi and Prof. Ryosho Nakane who grew the samples for my research and gave me invaluable advices.

I deeply thank Prof. Liu Hao Tjeng and Dr. Chun-Fu Chang of the Max Planck Institute for Chemical Physics of Solids, who have provided the high-quality Fe_3O_4 thin films. I also thank Dr. Xionghua Liu for giving me characterization data.

I deeply gratitude Prof. Arata Tanaka. He developed the program 'Xtls version 8.5', and kindly answered many of my questions.

I appreciate Prof. Tsuneharu Koide, Prof. Kenta Amemiya, and Prof. Masako Suzuki-Sakamaki for their support during the measurements at the BL-16A of KEK-PF. The state-of-the art soft x-ray undulator beamline has allowed me to take high-quality spectra.

The measurements at BL-16A of KEK-PF were supported by Dr. Shoya Sakamoto, Mr. Keisuke Ikeda, Mr. Zhendong Chi, Mr. Masahiro Suzuki, and Mr.

Yuxuan Wan, who helped the XMCD experiments and analysis. Their cooperation were very valuable.

I also appreciate the support at the BL23SU of SPring-8 from Dr. Yukiharu Takeda, Dr. Yuji Saitoh, and Prof. Hiroshi Yamagami. Although experimental data measured at SPring-8 are not included this thesis, I obtained crucial perspectives from them.

I would also express my gratitude to Prof. Tomohiko Saitoh of the Tokyo University of Science, who is my former supervisor of the undergraduate research program. He taught me how interesting the physics of solids is, and without his guidance, I would not choose this field of study.

I would like to give many thanks to the current and former members of Fujimori group. Prof. Kozo Okazaki, Prof. Masaki Kobayashi, Dr. Keisuke Ishigami, Dr. Hakuto Suzuki, Dr. Jian Xu, Dr. Masahumi Horio, Mr. Keisuke Koshiishi, Mr. Kenta Hagiwara, Mr. Suguru Nakata, Mr. Chun Lin, Mr. Takahito Takeda, Ms. Mayuko Niwata, Ms. Ami Michimura, and Ms. Yuko Shimazaki.

Finally, I would like to express cordial gratitude to my parents for their continuing support and warm encouragement.

December 2018,
Yosuke Nonaka

References

[1] A. Urushibara, Y. Moritomo, T. Arima, A. Asamitsu, G. Kido, and Y. Tokura, Phys. Rev. B **51**, 14103 (1995).

[2] M. Imada, A. Fujimori, and Y. Tokura, Rev. Mod. Phys. **70**, 1039 (1998).

[3] D. N. Astrov, Sov. Phys. JETP **11**, 708 (1960).

[4] J. G. Bednorz and K. A. Müller, Zeitschrift für Phys. B Condens. Matter **64**, 189 (1986).

[5] Y. Lu, Ph.D. thesis, 2017.

[6] K. Momma and F. Izumi, J. Appl. Crystallogr. **44**, 1272 (2011).

[7] Y. Tokura and N. Nagaosa, Science (80-.). **288**, 462 (2000).

[8] Y. Murakami, J. P. Hill, D. Gibbs, M. Blume, I. Koyama, M. Tanaka, H. Kawata, T. Arima, Y. Tokura, K. Hirota, and Y. Endoh, Phys. Rev. Lett. **81**, 582 (1998).

[9] K. Yosida and M. Tachiki, Prog. Theor. Phys. **17**, 331 (1957).

[10] P. G. Radaelli, New J. Phys. **7**, 53 (2005).

[11] G. A. Sawatzky, F. VAN DER Woude, and A. H. Morrish, J. Appl. Phys. **39**, 1204 (1968).

[12] S. Kondo, D. C. Johnston, C. A. Swenson, F. Borsa, A. V. Mahajan, L. L. Miller, T. Gu, A. I. Goldman, M. B. Maple, D. A. Gajewski, E. J. Freeman, N. R. Dilley, R. P. Dickey, J. Merrin, K. Kojima, G. M. Luke, Y. J. Uemura, O. Chmaissem, and J. D. Jorgensen, Phys. Rev. Lett. **78**, 3729 (1997).

[13] O. Zaharko, N. B. Christensen, A. Cervellino, V. Tsurkan, A. Maljuk, U. Stuhr, C. Niedermayer, F. Yokaichiya, D. N. Argyriou, M. Boehm, and A. Loidl, Phys. Rev. B **84**, 94403 (2011).

[14] V. Fritsch, J. Hemberger, N. Büttgen, E.-W. Scheidt, H.-A. Krug von Nidda, A. Loidl, and V. Tsurkan, Phys. Rev. Lett. **92**, 116401 (2004).

[15] R. Fichtl, V. Tsurkan, P. Lunkenheimer, J. Hemberger, V. Fritsch, H.-A. K. von Nidda, E.-W. Scheidt, and A. Loidl, Phys. Rev. Lett. **94**, 027601 (2005).

[16] Y. Yamasaki, S. Miyasaka, Y. Kaneko, J.-P. He, T. Arima, and Y. Tokura, Phys. Rev. Lett. **96**, 207204 (2006).

[17] T. Suzuki, M. Katsumura, K. Taniguchi, T. Arima, and T. Katsufuji, Phys. Rev. Lett. **98**, 127203 (2007).

[18] H. Tsunetsugu and Y. Motome, Phys. Rev. B **68**, 060405 (2003).

[19] D. I. Khomskii and T. Mizokawa, Phys. Rev. Lett. **94**, 156402 (2005).

[20] O. Tchernyshyov, Phys. Rev. Lett. **93**, 157206 (2004).

[21] H. Ishibashi, S. Shimono, K. Tomiyasu, S. Lee, S. Kawaguchi, H. Iwane, H. Nakao, S. Torii, T. Kamiyama, and Y. Kubota, Phys. Rev. B **96**, 144424 (2017).

[22] Y. KATO and T. TAKEI, J. Inst. Electr. Eng. Japan **53**, 408 (1933).

[23] L. Néel, Ann. Phys **3**, 137 (1948).

[24] J. Kanamori, *Magnetism*, 1st ed. (Baifukan, Tokyo, 1969).

[25] J. S. Moodera, G. X. Miao, and T. S. Santos, Phys. Today **63**, 46 (2010).

[26] T. S. Santos, J. S. Moodera, K. V. Raman, E. Negusse, J. Holroyd, J. Dvorak, M. Liberati, Y. U. Idzerda, and E. Arenholz, Phys. Rev. Lett. **101**, 147201 (2008).

[27] J. S. Moodera, T. S. Santos, and T. Nagahama, J. Phys.: Condens. Matter **19**, 165202 (2007).

[28] B. S. Holinsworth, D. Mazumdar, H. Sims, Q. C. Sun, M. K. Yurtisigi, S. K. Sarker, A. Gupta, W. H. Butler, and J. L. Musfeldt, Appl. Phys. Lett. **103**, 082406 (2013).

[29] S. Matzen, J. B. Moussy, R. Mattana, K. Bouzehouane, C. Deranlot, and F. Petroff, Appl. Phys. Lett. **101**, 042409 (2012).

[30] J.-B. Moussy, J. Phys. D. Appl. Phys. **46**, 143001 (2013).

[31] Y. K. Takahashi, S. Kasai, T. Furubayashi, S. Mitani, K. Inomata, and K. Hono, Appl. Phys. Lett. **96**, 072512 (2010).

[32] A. V. Ramos, M.-J. Guittet, J.-B. Moussy, R. Mattana, C. Deranlot, F. Petroff, and C. Gatel, Appl. Phys. Lett. **91**, 122107 (2007).

[33] Z. Szotek, W. M. Temmerman, D. Ködderitzsch, A. Svane, L. Petit, and H. Winter, Phys. Rev. B **74**, 174431 (2006).

[34] D. T. Margulies, F. T. Parker, F. E. Spada, R. S. Goldman, J. Li, R. Sinclair, and A. E. Berkowitz, Phys. Rev. B **53**, 9175 (1996).

[35] D. T. Margulies, F. T. Parker, M. L. Rudee, F. E. Spada, J. N. Chapman, P. R. Aitchison, and a. E. Berkowitz, Phys. Rev. Lett. **79**, 5162 (1997).

[36] F. C. Voogt, T. T. M. Palstra, L. Niesen, O. C. Rogojanu, M. A. James, and T. Hibma, Phys. Rev. B **57**, R8107 (1998).

[37] W. Eerenstein, T. T. M. Palstra, T. Hibma, and S. Celotto, Phys. Rev. B **66**, 201101 (2002).

[38] J.-B. Moussy, S. Gota, A. Bataille, M.-J. Guittet, M. Gautier-Soyer, F. Delille, B. Dieny, F. Ott, T. Doan, P. Warin, P. Bayle-Guillemaud, C. Gatel, and E. Snoeck, Phys. Rev. B **70**, 174448 (2004).

[39] R. Bachelet, P. de Coux, B. Warot-Fonrose, V. Skumryev, G. Niu, B. Vilquin, G. Saint-Girons, and F. Sánchez, CrystEngComm **16**, 10741 (2014).

[40] Y. K. Wakabayashi, Y. Nonaka, Y. Takeda, S. Sakamoto, K. Ikeda, Z. Chi, G. Shibata, A. Tanaka, Y. Saitoh, H. Yamagami, M. Tanaka, A. Fujimori, and R. Nakane, Phys. Rev. B **96**, 104410 (2017).

[41] Y. K. Wakabayashi, Y. Nonaka, Y. Takeda, S. Sakamoto, K. Ikeda, Z. Chi, G. Shibata, A. Tanaka, Y. Saitoh, H. Yamagami, M. Tanaka, A. Fujimori, and R. Nakane, Phys. Rev. Mater. **2**, 104416 (2018).

[42] M. I. Katsnelson, V. Y. Irkhin, L. Chioncel, A. I. Lichtenstein, and R. A. de Groot, Rev. Mod. Phys. **80**, 315 (2008).

[43] N. Takahashi, T. Huminiuc, Y. Yamamoto, T. Yanase, T. Shimada, A. Hirohata, and T. Nagahama, Sci. Rep. **7**, 7009 (2017).

[44] J. García and G. Subías, J. Phys.: Condens. Matter **16**, R145 (2004).

[45] A. J. M. Kuipers and V. A. M. Brabers, Phys. Rev. B **20**, 594 (1979).

[46] R. Aragón, D. J. Buttrey, J. P. Shepherd, and J. M. Honig, Phys. Rev. B **31**, 430 (1985).

[47] E. J. Verwey and E. L. Heilmann, J. Chem. Phys. **15**, 174 (1947).

[48] E. J. W. VERWEY, Nature **144**, 327 (1939).

[49] E. J. Samuelsen, E. J. Bleeker, L. Dobrzynski, and T. Riste, J. Appl. Phys. **39**, 1114 (1968).

[50] T. Yamada, K. Suzuki, and S. Chikazumi, Appl. Phys. Lett. **13**, 172 (1968).

[51] R. Hargrove and W. Kündig, Solid State Commun. **8**, 303 (1970).

[52] M. Rubinstein and D. Forester, Solid State Commun. **9**, 1675 (1971).

[53] F. Walz, J. Phys.: Condens. Matter **14**, R285 (2002).

[54] I. Leonov, A. N. Yaresko, V. N. Antonov, M. A. Korotin, and V. I. Anisimov, Phys. Rev. Lett. **93**, 146404 (2004).

[55] H.-T. Jeng, G. Y. Guo, and D. J. Huang, Phys. Rev. Lett. **93**, 156403 (2004).

[56] H. T. Jeng, G. Y. Guo, and D. J. Huang, Phys. Rev. B **74**, 195115 (2006).

[57] D. J. Huang, H.-J. Lin, J. Okamoto, K. S. Chao, H.-T. Jeng, G. Y. Guo, C.-H. Hsu, C.-M. Huang, D. C. Ling, W. B. Wu, C. S. Yang, and C. T. Chen, Phys. Rev. Lett. **96**, 096401 (2006).

[58] J. Schlappa, C. Schüßler-Langeheine, C. F. Chang, H. Ott, A. Tanaka, Z. Hu, M. W. Haverkort, E. Schierle, E. Weschke, G. Kaindl, and L. H. Tjeng, Phys. Rev. Lett. **100**, 026406 (2008).

[59] M. S. Senn, J. P. Wright, and J. P. Attfield, Nature **481**, 173 (2011).

[60] K. Yamauchi, T. Fukushima, and S. Picozzi, Phys. Rev. B **79**, 212404 (2009).

[61] H. Uzu and A. Tanaka, J. Phys. Soc. Jpn **77**, 074711 (2008).

[62] H. Uzu and A. Tanaka, J. Phys. Soc. Jpn **75**, 043704 (2006).

[63] A. Tanaka, C. F. Chang, M. Buchholz, C. Trabant, E. Schierle, J. Schlappa, D. Schmitz, H. Ott, P. Metcalf, L. H. Tjeng, and C. Schüßler-Langeheine, Phys. Rev. B **88**, 195110 (2013).

[64] A. Tanaka, C. F. Chang, M. Buchholz, C. Trabant, E. Schierle, J. Schlappa, D. Schmitz, H. Ott, P. Metcalf, L. H. Tjeng, and C. Schüßler-Langeheine, Phys. Rev. Lett. **108**, 227203 (2012).

[65] S. M. Shapiro, M. Iizumi, and G. Shirane, Phys. Rev. B **14**, 200 (1976).

[66] Y. Yamada, M. Mori, Y. Noda, and M. Iizumi, Solid State Commun. **32**, 827 (1979).

[67] Y. Yamada, Philos. Mag. B **42**, 377 (1980).

[68] M. Kobayashi, Ph.D. thesis, The University of Tokyo, 2007.

[69] B. T. Thole, P. Carra, F. Sette, and G. van der Laan, Phys. Rev. Lett. **68**, 1943 (1992).

[70] P. Carra, B. T. Thole, M. Altarelli, and X. Wang, Phys. Rev. Lett. **70**, 694 (1993).

[71] J. Stöhr and H. König, Phys. Rev. Lett. **75**, 3748 (1995).

[72] R. Wu and A. Freeman, Phys. Rev. Lett. **73**, 1994 (1994).

[73] *SpinOrbit-Influenced Spectroscopies of Magnetic Solids*, Vol. 466 of *Lecture Notes in Physics*, edited by H. Ebert and G. Schütz (Springer Berlin Heidelberg, Berlin, Heidelberg, 1996).

[74] *New Directions in Research with Third-Generation Soft X-Ray Synchrotron Radiation Sources*, edited by A. S. Schlachter and F. J. Wuilleumier (Springer Netherlands, Dordrecht, 1994).

[75] C. T. Chen, Y. U. Idzerda, H.-J. Lin, N. V. Smith, G. Meigs, E. Chaban, G. H. Ho, E. Pellegrin, and F. Sette, Phys. Rev. Lett. **75**, 152 (1995).

[76] D. Bonnenberg, K. A. Hempel, and H. P. J. Wijn, in *3d, 4d and 5d Elements, Alloys and Compounds*, Vol. 19a of *Landolt-Börnstein - Group III Condensed Matter*, edited by H. Wijn (Springer-Verlag, Berlin/Heidelberg, 1986).

[77] Y. Teramura, A. Tanaka, and T. Jo, J. Phys. Soc. Jpn **65**, 1053 (1996).

[78] L. Martín-García, R. Gargallo-Caballero, M. Monti, M. Foerster, J. F. Marco, L. Aballe, and J. de la Figuera, Phys. Rev. B **91**, 020408 (2015).

[79] B. H. Frazer, B. Gilbert, B. R. Sonderegger, and G. De Stasio, Surf. Sci. **537**, 161 (2003).

[80] S. Eisebitt, T. Böske, J.-E. Rubensson, and W. Eberhardt, Phys. Rev. B **47**, 14103 (1993).

[81] R. Nakajima, J. Stöhr, and Y. Idzerda, Phys. Rev. B **59**, 6421 (1999).

[82] W. A. Harrison, *Electronic Structure and the Properties of Solids*, 3rd ed. (Freeman, San Francisco, 1980).

[83] T. Mizokawa and a. Fujimori, Phys. Rev. B **48**, 14150 (1993).

[84] A. Tanaka and T. Jo, J. Phys. Soc. Jpn **63**, 2788 (1994).

[85] S. Hüfner, *Photoelectron Spectroscopy*, *Advanced Texts in Physics*, 3 ed. (Springer Berlin Heidelberg, Berlin, Heidelberg, 2003).

[86] K. Amemiya, BL-16A: Variable Polarization Soft X-ray spectroscopy Station, http://pfwww.kek.jp/users_info/users_guide_e/station_spec_e/bl16/bl16a.html, retrieved in December 8, 2018.

[87] K. Amemiya, A. Toyoshima, T. Kikuchi, T. Kosuge, K. Nigorikawa, R. Sumii, K. Ito, R. Garrett, I. Gentle, K. Nugent, and S. Wilkins, in *AIP Conf. Proc.* (PUBLISHER, ADDRESS, 2010), No. 2010, pp. 295–298.

[88] T. Muro, T. Nakamura, T. Matsushita, H. Kimura, T. Nakatani, T. Hirono, T. Kudo, K. Kobayashi, Y. Saitoh, M. Takeuchi, T. Hara, K. Shirasawa, and H. Kitamura, J. Electron Spectros. Relat. Phenomena **144-147**, 1101 (2005).

[89] M. Furuse, M. Okano, S. Fuchino, A. Uchida, J. Fujihira, and S. Fujihira, IEEE Trans. Appl. Supercond. **23**, 4100704 (2013).

[90] G. Shibata, M. Kitamura, M. Minohara, K. Yoshimatsu, T. Kadono, K. Ishigami, T. Harano, Y. Takahashi, S. Sakamoto, Y. Nonaka, K. Ikeda, Z. Chi, M. Furuse, S. Fuchino, M. Okano, J.-i. Fujihira, A. Uchida, K. Watanabe, H. Fujihira, S. Fujihira, A. Tanaka, H. Kumigashira, T. Koide, and A. Fujimori, npj Quantum Mater. **3**, 3 (2018).

[91] X. Hao, J. S. Moodera, and R. Meservey, Phys. Rev. B **42**, 8235 (1990).

[92] J. S. Moodera, R. Meservey, and X. Hao, Phys. Rev. Lett. **70**, 853 (1993).

[93] B. T. Thole, G. van der Laan, J. C. Fuggle, G. A. Sawatzky, R. C. Karnatak, and J.-M. Esteva, Phys. Rev. B **32**, 5107 (1985).

[94] K. Amemiya, M. Sakamaki, T. Koide, K. Ito, K. Tsuchiya, K. Harada, T. Aoto, T. Shioya, T. Obina, S. Yamamoto, and Y. Kobayashi, J. Phys. Conf. Ser. **425**, 152015 (2013).

[95] E. C. Stoner and E. P. Wohlfarth, Philos. Trans. R. Soc. London. Ser. A **240**, 599 (1948).

[96] H. Shenker, Phys. Rev. **107**, 1246 (1957).

[97] M. Tachiki, Prog. Theor. Phys. **23**, 1055 (1960).

[98] W. Huang, J. Zhu, H. Z. Zeng, X. H. Wei, Y. Zhang, and Y. R. Li, Appl. Phys. Lett. **89**, 262506 (2006).

[99] A. Lisfi, C. M. Williams, L. T. Nguyen, J. C. Lodder, A. Coleman, H. Corcoran, A. Johnson, P. Chang, A. Kumar, and W. Morgan, Phys. Rev. B **76**, 054405 (2007).

[100] S. Xie, J. Cheng, B. W. Wessels, and V. P. Dravid, Appl. Phys. Lett. **93**, 181901 (2008).

[101] J. H. Yin, J. Ding, B. H. Liu, J. B. Yi, X. S. Miao, and J. S. Chen, J. Appl. Phys. **101**, 09K509 (2007).

[102] M. Khodaei, S. Seyyed Ebrahimi, Y. J. Park, J. M. Ok, J. S. Kim, J. Son, and S. Baik, J. Magn. Magn. Mater. **340**, 16 (2013).

[103] C.-W. Cho, D. Lee, J. Bae, and S. Park, J. Magn. Magn. Mater. **368**, 149 (2014).

[104] R. Patel, T. Tainosho, Y. Hisamatsu, S. Sharmin, E. Kita, and H. Yanagihara, Jpn. J. Appl. Phys. **56**, 053001 (2017).

[105] G. Hu, J. Choi, C. Eom, V. Harris, and Y. Suzuki, Phys. Rev. B **62**, R779 (2000).

[106] J. Chen, D. J. Huang, A. Tanaka, C. F. Chang, S. C. Chung, W. B. Wu, and C. T. Chen, Phys. Rev. B **69**, 085107 (2004).

[107] S. Matzen, J. B. Moussy, R. Mattana, F. Petroff, C. Gatel, B. Warot-Fonrose, J. C. Cezar, A. Barbier, M. A. Arrio, and P. Sainctavit, Appl. Phys. Lett. **99**, 052514 (2011).

[108] J. Takaobushi, M. Ishikawa, S. Ueda, E. Ikenaga, J.-J. Kim, M. Kobata, Y. Takeda, Y. Saitoh, M. Yabashi, Y. Nishino, D. Miwa, K. Tamasaku, T. Ishikawa, I. Satoh, H. Tanaka, K. Kobayashi, and T. Kawai, Phys. Rev. B **76**, 205108 (2007).

[109] S. Matzen, J.-B. Moussy, P. Wei, C. Gatel, J. C. Cezar, M. A. Arrio, P. Sainctavit, and J. S. Moodera, Appl. Phys. Lett. **104**, 182404 (2014).

[110] C. M. Srivastava, G. Srinivasan, and N. G. Nanadikar, Phys. Rev. B **19**, 499 (1979).

[111] E. Goering, S. Gold, M. Lafkioti, and G. Schütz, Europhys. Lett. **73**, 97 (2006).

[112] D. J. Huang, C. F. Chang, H.-T. Jeng, G. Y. Guo, H.-J. Lin, W. B. Wu, H. C. Ku, A. Fujimori, Y. Takahashi, and C. T. Chen, Phys. Rev. Lett. **93**, 077204 (2004).

[113] E. Goering, M. Lafkioti, S. Gold, and G. Schuetz, J. Magn. Magn. Mater. **310**, e249 (2007).

[114] M. Kallmayer, K. Hild, H. J. Elmers, S. K. Arora, H.-C. Wu, R. G. S. Sofin, and I. V. Shvets, J. Appl. Phys. **103**, 07D715 (2008).

[115] G. F. M. Gomes, T. E. P. Bueno, D. E. Parreiras, G. J. P. Abreu, A. de Siervo, J. C. Cezar, H.-D. Pfannes, and R. Paniago, Phys. Rev. B **90**, 134422 (2014).

[116] T. Kasama, N. S. Church, J. M. Feinberg, R. E. Dunin-Borkowski, and R. J. Harrison, Earth Planet. Sci. Lett. **297**, 10 (2010).

[117] X. W. Li, A. Gupta, G. Xiao, and G. Q. Gong, J. Appl. Phys. **83**, 7049 (1998).

[118] R. G. S. Sofin, S. K. Arora, and I. V. Shvets, Phys. Rev. B **83**, 134436 (2011).

[119] M. Baghaie Yazdi, K.-Y. Choi, D. Wulferding, P. Lemmens, and L. Alff, New J. Phys. **15**, 103032 (2013).

[120] E. Arenholz, G. van der Laan, R. V. Chopdekar, and Y. Suzuki, Phys. Rev. B **74**, 094407 (2006).

[121] G. van der Laan, R. V. Chopdekar, Y. Suzuki, and E. Arenholz, Phys. Rev. Lett. **105**, 067405 (2010).

[122] A. R. Muxworthy and E. McClelland, Geophys. J. Int. **140**, 101 (2000).

[123] C. A. Domenicali, Phys. Rev. **78**, 458 (1950).

[124] Y. Nii, H. Sagayama, T. Arima, S. Aoyagi, R. Sakai, S. Maki, E. Nishibori, H. Sawa, K. Sugimoto, H. Ohsumi, and M. Takata, Phys. Rev. B **86**, 125142 (2012).

[125] S. Sarkar and T. Saha-Dasgupta, Phys. Rev. B **84**, 235112 (2011).